Distribution Agreement

In presenting this thesis or dissertation as a partial fulfillment of the requirements for an advanced degree from Emory University, I hereby grant to Emory University and its agents the non-exclusive license to archive, make accessible, and display my thesis or dissertation in whole or in part in all forms of media, now or hereafter known, including display on the world wide web. I understand that I may select some access restrictions as part of the online submission of this thesis or dissertation. I retain all ownership rights to the copyright of the thesis or dissertation. I also retain the right to use in future works (such as articles or books) all or part of this thesis or dissertation.

Signature:

______________________________ _______________
Daniel R. Stabley Date

Nanoscale Tools to Expand the Biophysical Understanding of Epidermal Growth Factor Receptor Function

By

Daniel R. Stabley

Doctor of Philosophy

Chemistry

Khalid Salaita
Advisor

David Lynn
Committee Member

Stefan Lutz
Committee Member

Accepted:

Lisa A. Tedesco, Ph.D.
Dean of the James T. Laney School of Graduate Studies

Date

Nanoscale Tools to Expand the Biophysical Understanding of Epidermal Growth Factor Receptor Function

By

Daniel R. Stabley

B.S. Wayne State University, 2008

Advisor: Khalid Salaita, Ph.D.

An abstract of

A dissertation submitted to the Faculty of the

James T. Laney School of Graduate Studies of Emory University

in partial fulfillment of the requirements for the degree of

Doctor of Philosophy

in Chemistry

2014

Abstract

Nanoscale Tools to Expand the Biophysical Understanding of Epidermal Growth Factor Receptor Function

By Daniel R. Stabley

Modern techniques in biochemistry and fluorescence imaging have done much to reveal the vast chemical signaling networks associated with cell surface receptors, however many aspects of receptor function and regulation remain obscure. This is especially evident in the case of the epidermal growth factor receptor (EGFR), a long-studied receptor tyrosine kinase. While the signaling networks of the EGFR are largely known, there are still critical elements of receptor function that have not been elucidated. For example, the EGFR has long been shown to self-assemble during the process of activation, but the precise functional role of this oligomerization is not well defined. Additionally, mechanical forces are thought to play a role during receptor endocytosis, but direct evidence has not been obtained.

This dissertation describes the development of novel methods to answer long-standing questions about cell receptor function that are difficult to answer with current techniques. Chapter 1 gives a brief history of the EGFR as well as an overview of the known aspects of its signaling networks and corresponding regulatory elements. Chapter 2 describes the development of a fluorescence force sensor that can directly measure forces exerted by the cell through receptor-ligand interactions. This sensor was used to visualize the force exerted on the EGFR during endocytosis, and remains as a facile and broadly applicable method for the characterization of mechanotransduction events in living cells. In chapter 3 we apply recently developed supported lipid bilayer

nanopatterning techniques to determine whether the formation of micron-sized EGFR oligomers impacts biochemical signaling output. Supported lipid bilayers were formed on surfaces modified with diffusion barriers and were subsequently functionalized with the epidermal growth factor (EGF), a ligand for the EGFR. By controlling the size of the diffusion barriers oligomer size could be controlled, and pairing this approach with standard immunofluorescence staining revealed a correlation between the cluster size and signaling output. Chapter 4 details the development of simultaneous two-wavelength axial ratiometry (STAR), a new fluorescence microscopy technique based on total internal reflection fluorescence microscopy (TIRF-M) that allows nanoscale imaging along the optical axis with millisecond time resolution. This technique was used to investigate the dynamics of EGFR internalization and stands as a turn-key method to study cell membrane processes with high spatial and temporal resolution. The final chapter gives a summary of these techniques as they have been implemented to date, and also describes future directions for their continued application. These approaches serve to expand the modern biochemical toolkit, allowing access to previously unknown aspects of long-studied biological systems.

Nanoscale Tools to Expand the Biophysical Understanding of Epidermal Growth Factor Receptor Function

By

Daniel R. Stabley

B.S. Wayne State University, 2008

Advisor: Khalid Salaita, Ph.D.

A dissertation submitted to the Faculty of the

James T. Laney School of Graduate Studies of Emory University

in partial fulfillment of the requirements for the degree of

Doctor of Philosophy

in Chemistry

2014

Dedication

This dissertation is dedicated to my wife, Molly, without whom none herein would be possible. Thank you for being my support when support was needed most, and for providing me with much needed perspective.

Acknowledgements

First and foremost, I thank my parents, Mark and Carol Stabley, for making me the person I am and supporting me through all of my hardest trials. I would also like to thank my advisor, Khalid Salaita, for taking me in at a time when I was struggling and, through much effort, instilling in me the core elements of scientific success. It was a great honor to be able to participate in the startup of a lab that I see (through biased eyes) as having a very bright future. I thank Shana Topp for being a wonderful friend and a true inspiration, and for providing much needed encouragement. Next I would like to thank my labmates for all of their support and lent knowledge. Kevin Yehl, for being a great friend and confidant from the early years of the lab, as well as a talented scientist. Yoshie Narui, for her many contributions to lab logistics that that keep things running smoothly, and for being a labmate that I could always depend on for advice. Carol Jurchenko, without whom MTFM would not have been possible. Thank you for suffering through an extremely challenging project with me, and for all of your hard work. Yang, Yuan, Yun, Kornelia, WeiWei, and Zheng – I can't wait to see what the future holds for the Salaita lab in your capable hands. Finally, I would like to thank my friends Colleen Knight, Brad Balthaser, Erin Schuler, and Ashley Daugherty for being great sources of advice and support, and for all of the great times together.

Chapter 1: The EGFR Signaling Pathway

Chapter 2: Visualizing Mechanical Tension Across Membrane Receptors with a Fluorescent Sensor

Chapter 3: Manipulating the Lateral Diffusion of Surface-Anchored EGF Demonstrates that Receptor Clustering Modulates Phosphorylation Levels

Chapter 4: Simultaneous Two-Wavelength Axial Ratiometry (STAR) for Imaging Protein Dynamics with sub-15 nm Accuracy in Living Cells

Chapter 5: Conclusion

List of Figures

Chapter 1: The EGFR Signaling Pathway

1.1 Introduction

1.1.1 Historical Perspectives

The discovery of the Epidermal Growth Factor Receptor (EGFR) was preceded by the discovery of one of its cognate ligands, the Epidermal Growth Factor (EGF). Stanley Cohen was looking for novel biologically derived compounds that increase nerve cell growth. During these endeavors, a peptide was isolated from a wide variety of sources (including snake venom and mouse submaxillary glands) that was found to have a profound effect on living ganglia. When cells were exposed to this factor, they rapidly began to change and produce a large number of nerve fiber projections (Fig 1.1).[1]

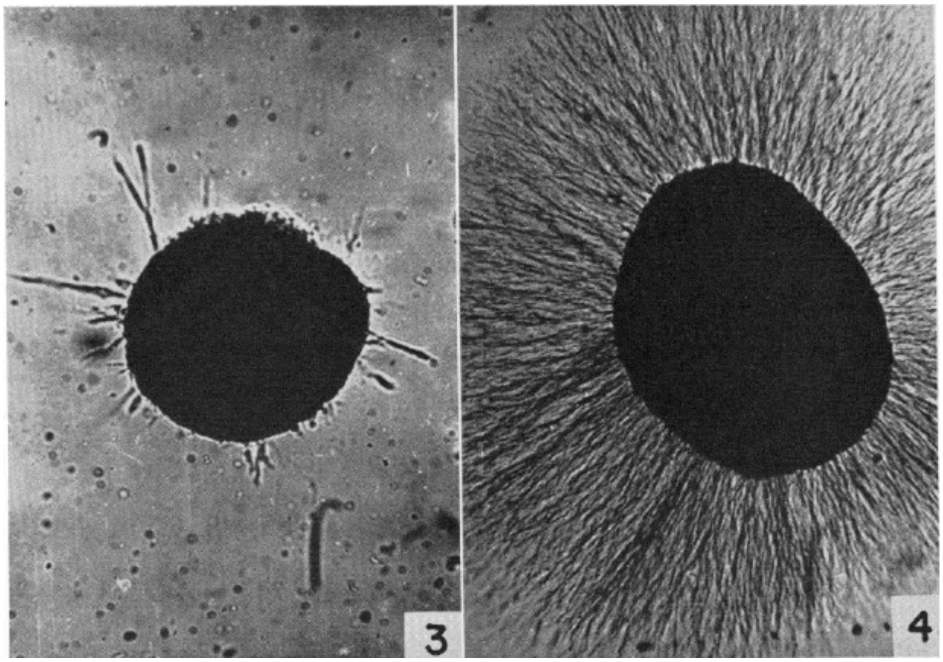

Fig 1.1: Effect of Nerve Growth Factor on living cells.

Representative images of living 9 day old chick sensory ganglia in the absence (3) or presence (4) of Nerve Growth Factor. Adapted from Cohen *et Al.*[1]

Thus, this compound came to be known as nerve growth factor, and was among the first of a class of proteins called growth factors to be discovered.

During the course of the pioneering studies on nerve growth factor, another interesting compound was incidentally discovered. Cohen initially noticed that mice and rats injected with nerve growth factor isolates from mouse salivary glands experienced profound developmental changes that were unrelated to the previously published effects on nerve cells. These changes included early opening of the eyelids, early eruption of teeth, a marked decrease in hair growth, and a decrease in overall growth of the animal (Fig 1.2).[2] These changes were later found to be due to early onset of keratinization of the epidermal layer as well as increased proliferation of epidermal cells, and thus the peptide came to be known as the Epidermal Growth Factor (EGF).[3,4] Importantly, Cohen's work, along with that of his collaborator Rita Levi-Montalcini, established growth factors as a diverse and critical element of cell biology, and earned them the Nobel Prize in Medicine in 1986.

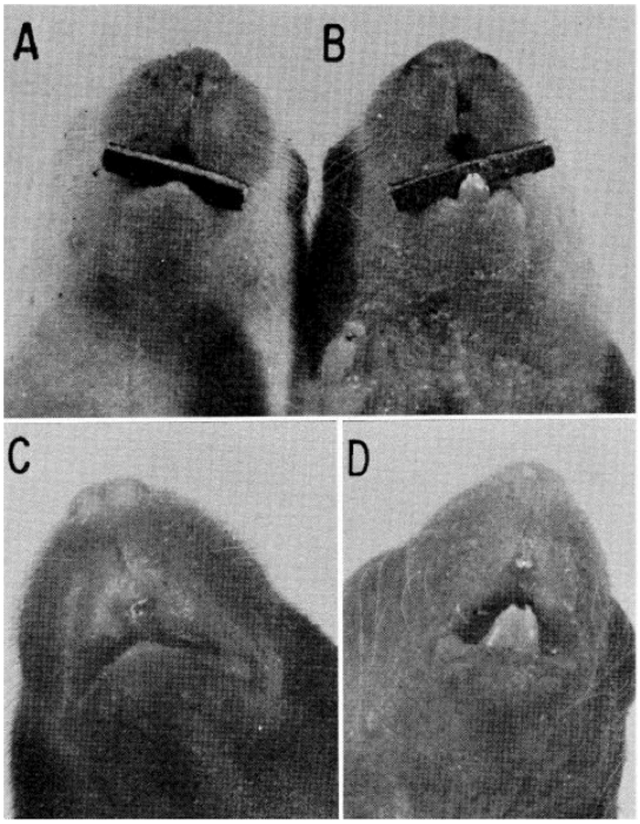

Fig 1.2: The anatomical effects of EGF on newborn mice and rats.
Contol 8 day old mice (A) and rats (C) as compared to animals injected with EGF (B,D). Adapted from Cohen *et Al.*[2]

Following the discovery of EGF, attention naturally turned to finding the receptor to which it binds. Cohen himself led the charge to find this cryptic protein with initial studies using radiolabeled EGF. This line of inquiry resulted in the discovery that EGF does in fact bind to a specific site on the cell surface, and established a cumulative binding constant of 0.27-0.43 nM.[5] Following this study, the first co-purification of receptor and ligand was reported.[6] Importantly, it was shown that exposure of cells to EGF resulted in phosphorylation of membrane proteins[6], specifically at tyrosine residues.[7] In addition to providing the first evidence of a specific receptor for EGF, these studies established an initial foothold into the characteristic phosphorylation cascade that results from EGF stimulation of cells. Although early studies isolated a co-precipitated protein from membrane fractions treated with EGF, the cDNA of the EGFR and a conclusive protein identity were not established until 1984.[8] The crystal structure of the EGFR followed almost two decades later (no doubt due to the difficulties of crystallizing transmembrane proteins) and was obtained in a piecemeal fashion, with the structure of the extracellular domain preceding that of the kinase domain. [9,10]

These key studies establish the historical precedent of the EGFR, from the discovery of the physiological effects of its ligand all the way up to the elucidation of its crystal structure. Importantly, at each point along this path, many new aspects of EGFR function were discovered and related to the existing literature, building up a large body of knowledge, and making the EGFR one of the best-studied receptors, and signaling pathways in all of biology. The insights obtained into the function of the EGFR will be discussed in detail in later sections of this work.

1.1.2 Impact on Human Health

Though fundamental questions about receptor function have driven many to study the EGFR, it is perhaps even better recognized for its implication in many catastrophic diseases, especially cancer. The first clue that the EGFR was involved in the development of cancer phenotypes came from the avian erythroblastosis tumor virus (AEV), a virus that can induce both erythroblastomas and sarcomas in birds. The malignant action of the virus was traced to a mutant homolog of EGFR contained in the viral genome through the use of site-specific protein mutagenesis and analysis of the viral sequence.[11,12] These studies showed that the mutant EGFR was specifically required for cancer to develop from viral exposure, establishing the hallmark of EGFR mutation that is found in a wide variety of cancers. In addition to mutation of the EGFR, a common mechanism of its contribution to cancer is overexpression of the receptor. A meta-analysis of over 200 studies reporting EGFR expression levels in relation to cancer relapse or survival showed that EGFR expression levels were correlated with prognosis for many types of cancer, including cancers of the head, neck, ovaries, bladder, and esophagus.[13]

In light of the prevalence of EGFR mutation and overexpression in common cancer types, it is no surprise that EGFR has become a prime target for molecular therapies. These molecules include kinase domain inhibitors of the EGFR such as Gefitinib and Erlotinib (which prevent the receptor from phosphorylating itself, thus shutting down signal propagation at the receptor level) and antibodies against the EGFR such as Cetuximab and Panitumumab.[14-16] While these therapies have found some success in the clinic, the response rates remain low in some instances. For example, in a study of 115 patients with squamous cell cancer of the head and neck, only five patients responded to Erlotinib therapy.[16] Such issues serve to reinforce the fact that, while EGFR is one of the best studied receptors, there is still much we do not know about the relation of its signaling network to cancer outcomes. In light of this, it is prudent to continue to strive for further understanding of the fine details of EGFR function so that more effective therapies can be devised in the future.

1.2 Current Models of EGFR Activation and Internalization

1.2.1 Critical Events in EGFR Signaling

On the cell surface, the EGFR exists in an auto-inhibited monomeric state.[17-19] In typical paracrine signaling modes, the EGFR will bind to one of its cognate ligands (such as EGF or transforming growth factor alpha), and will then undergo a series of structural changes that lead to activation of the kinase domain.[20] One critical event in EGFR activation is the formation of EGFR oligomers. The native stoichiometry of ligand-EGFR interaction is 2:2, which has long established receptor dimerization as a critical step in EGFR activation.[9] EGFR dimers spontaneously form on the cell surface even in the

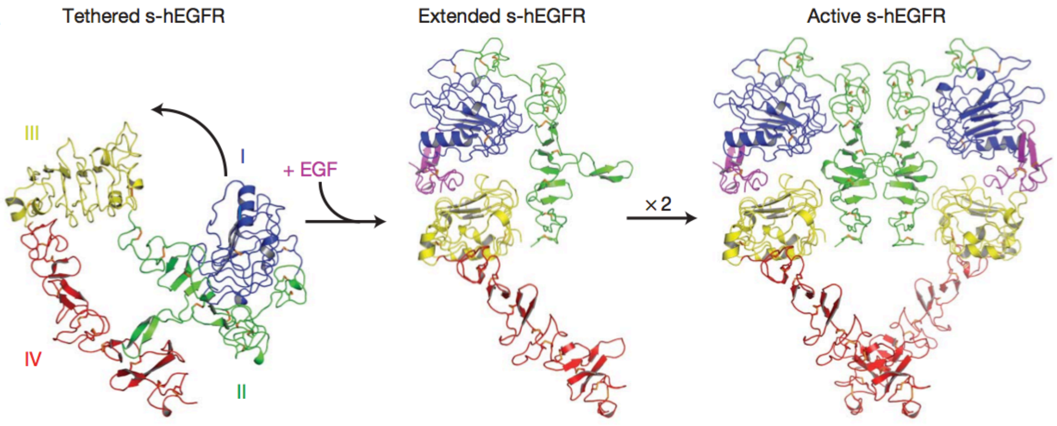

Fig 1.3: Crystal structure of tethered and activated EGFR extracellular domains. The initial tethered EGFR conformation (left) undergoes a rotation that primes the receptor for dimerization (right) through a critical domain (shown in green). The binding of EGF stabilizes the extension of tethered EGF and promotes dimerization.[17]

absence of ligand, and the EGFR has been shown to exhibit different ligand affinities depending on its oligomeric state.[21-23] Furthermore, mutation of critical domains involved in promoting dimerization of the receptor has been shown to interfere with activation.[24] Dimerization alone is not sufficient for activation, however, as the kinase domains undergo an essential allosteric shift after ligand binding and dimer stabilization that positions them in an asymmetric fashion for transphosphorylation (Fig 1.3).[19,22,23,25] In summary, the EGFR is initially autoinhibited but forms transient dimers in the absence of ligand. Dimerized receptor has an increased affinity for ligand, and ligand binding further reinforces the dimer state while also inducing rotation of the cytosolic domains into the proper position for transphosphorylation.

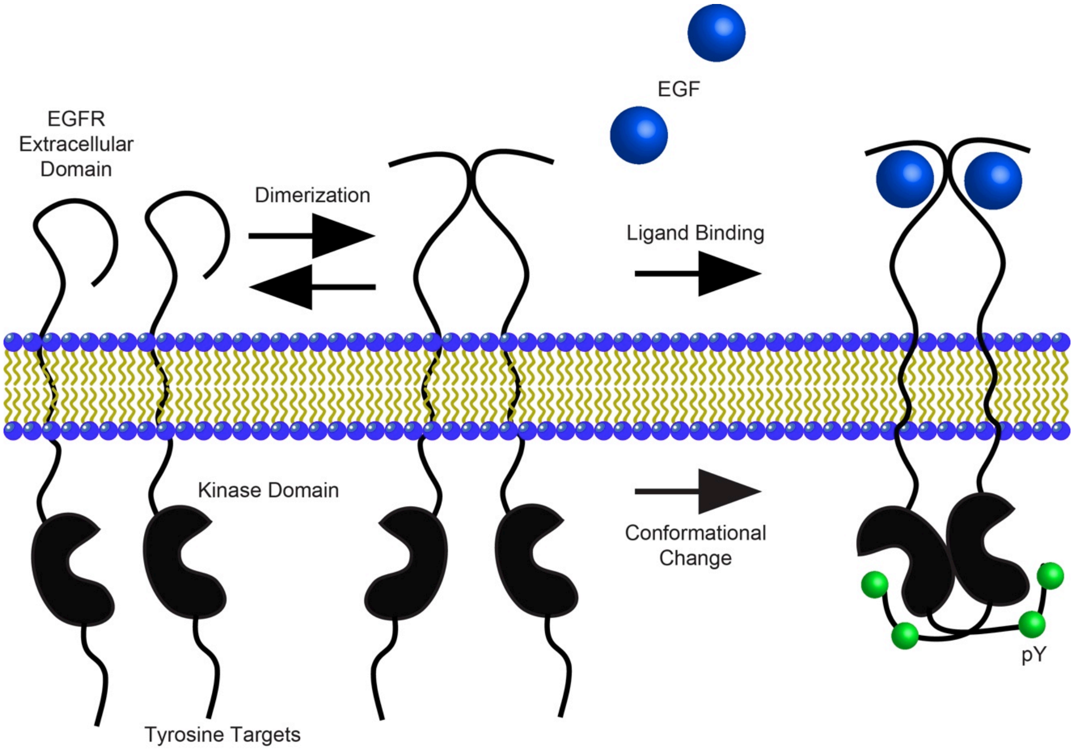

Fig 1.4: Critical steps in the initial activation of the EGFR.
From left to right: The EGFR exists in an autoinhibited state on the cell membrane and dynamically forms dimers through dimerization domain interactions that are primed for ligand binding. Binding of EGF triggers a further conformational change that locks the kinase domains of each receptor into the proper position for transphosphorylation.

Interestingly, EGFR assembly is not limited to the dimer state, and assemblies of higher order are described in the literature. For example, near-field scanning optical microscopy has revealed clusters on the order of 180 nm.[26] EGFR clusters have also been seen via number and brightness analysis and electron microscopy.[27,28] The nature and function of EGFR clusters are discussed at length in chapter 3, and play a critical role in this dissertation. It is also important to note that the EGFR is a member of a family of four similar receptors (the ErbB family) with highly intertwined signaling networks. In addition to the homodimerization described above, the EGFR can form pairs with other members of the ErbB family to affect different signaling outcomes. This heteromeric signaling paradigm is beyond the scope of this dissertation, and is reviewed elsewhere.[29]

Once the kinase domains have been primed by proper positioning, several key tyrosine residues are phosphorylated that trigger rapid recruitment of other kinases and adapter proteins with varying functions. For example, c-Src is recruited to activated EGFR and can directly phosphorylate the receptor, leading to strengthening of the signal.[30] Adaptor proteins such as AP-2, Grb2 and the ubiquitin ligase cbl are also recruited, and serve to initiate sorting of the receptor into clathrin-coated pits for internalization.[31-33] The EGFR phosphorylation cascade is extremely varied, but one of the

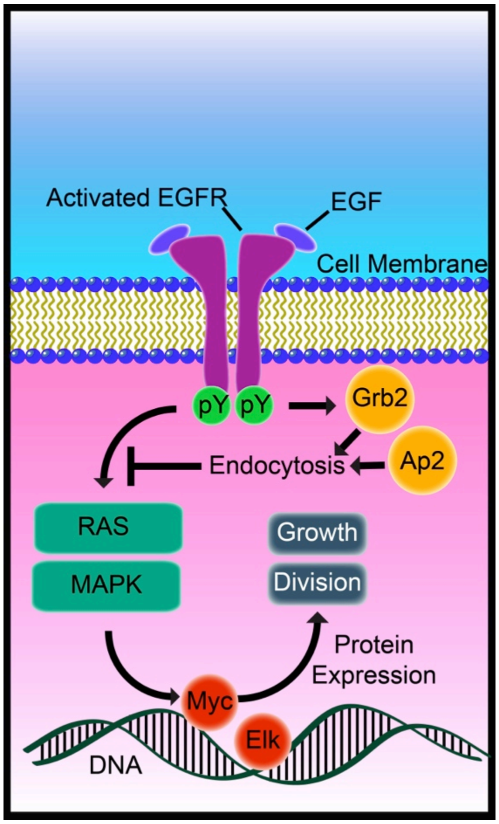

Fig 1.5: Schematic describing the basic tenets of the EGFR signaling pathway.

most common routes proceeds through the MAPK pathway via activation of RAS through secondary messengers that bind to key phosphotyrosine residues on the EGFR intracellular domain.[29,34] The endpoint of this cascade is the activation of transcription factors such as c-fos, Myc, and Elk which upregulate genes responsible for cell growth and division.[29,35] In this way, EGFR signals are highly mitogenic and regulation of their intensity and duration must be maintained in order to ensure normal cell behavior (Fig 1.4).

Regulation of EGFR surface concentration and signaling is primarily accomplished through endocytosis, the process by which activated receptor is internalized. As mentioned above, adapter proteins such as cbl, Grb2, and AP-2 interact with activated receptor in order to facilitate sorting into clathrin-coated pits. From this stage, the EGFR is either recycled back to the surface in its inactive state, or degraded via lysozomes. Different ligands can impact the outcome of this process, allowing ligand identity further control over signal duration and intensity. For example, EGF activation tends to result in degradation of active receptors, while TGF- α biases the outcome towards recycling.[36] Importantly, receptors that are trafficked to endosomal compartments during this process continue to generate signals which impact the downstream networks differently than receptors at the cell surface.[37] Internalization of the receptor, therefore, serves as both a signal repressor as well as a signal modulator, and is critical to the EGFR signaling pathway. Clathrin-mediated endocytosis of the EGFR is highly important to the work described herein, and will be described in greater detail in the subsequent section.

The previous discussion has focused on paracrine signaling of the EGFR, wherein soluble ligand interacts with receptors. It is important to note, however, that the EGFR has paracrine, autocrine, and juxtacrine signaling modes. In autocrine signaling, GPCRs can upregulate metalloproteases that cleave membrane-bound ligands such as heparin-binding EGF, freeing them to bind EGFR.[38] Juxtacrine signaling occurs between membrane-bound ligands on one cell and receptors on another. In the case of EGFR, ligands such as amphiregulin, HB-EGF, and TGF- α have all been shown to have juxtacrine signaling modes under certain conditions.[39] This diversity serves to illustrate the wide and varied nature of EGFR signaling and highlights the need to approach the study of EGFR in the context individual systems. Without this perspective, the immense magnitude of the signaling network makes general conclusions difficult to draw.

1.2.2 EGFR Endocytosis

Upon activation by its ligand, EGF, the duration of EGFR signals is regulated by a

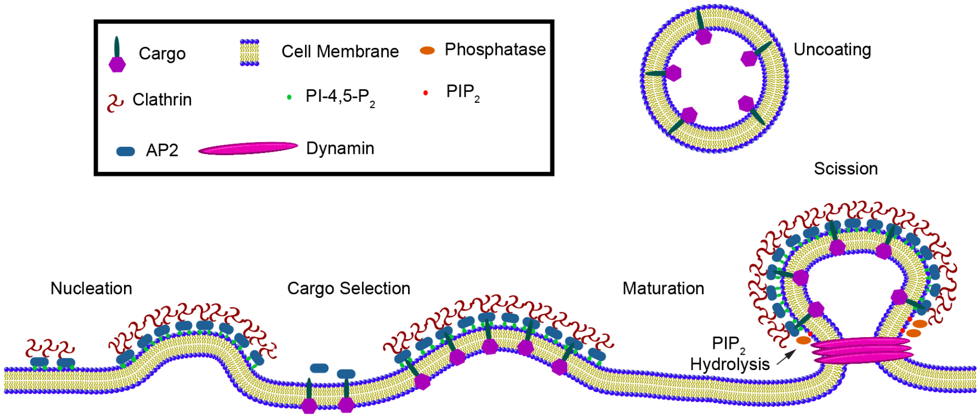

Fig 1.6: Schematic depicting the steps involved in clathrin mediated endocytosis (CME). Initially, AP-2 binds weakly to the lipid molecules PI-4 and 5-P$_2$ at specific locations in the cell membrane. If a clathrin molecule encounters two AP-2 molecules that are simultaneously associated with the membrane, pit nucleation will proceed. Next, cargo is sorted into the pit through interactions with adapter proteins (including AP-2 itself). When cargo has been properly selected, the pit will continue to mature through curvature-based recruitment of dynamin and phosphatases that hydrolyze PIP$_2$. Dynamin serves to protect proximal PIP$_2$ from hydrolysis, giving rise to an interfacial force that eventually causes the vesicle to pinch off from the membrane (scission). After the vesicle is released the assembled proteins disassociate and the cargo is trafficked to its eventual fate through endosomes.

process known as clathrin-mediated endocytosis (CME), wherein receptors are trafficked from the cell surface to the cell interior and rendered inactive.[31,37] CME serves as a generic transport mechanism for cargo that does not have transport proteins, and functions through specific protein self-assembly events that form pits of invaginated membrane on the cell surface followed by pinching off of a vesicle inside of the cell.

CME is initiated through a stochastic sampling process at the cell surface and this process is independent of receptor activation. The phosphoinositide PI-4,5-P_2 is naturally dispersed in the plasma membrane, and is capable of weakly binding to the protein AP-2, while clathrin itself cannot directly associate with the cell membrane. The initial nucleation events that trigger the eventual self-assembly of clathrin involve a coincidence detection step, wherein a single clathrin molecule encounters two membrane-anchored AP-2 molecules at the same time.[40] Once this stoichiometric threshold is crossed the multivalency of the interaction stabilizes the complex at the membrane, and clathrin lattice assembly will progress. The next critical step is the recruitment of cargo to pre-formed pits. In the case of EGFR, this occurs primarily through the action of the cbl ubiquitin ligase acting on the activated receptor, and recruitment of Grb2 and subsequent interaction with AP-2.[31,33,41] These adaptor proteins effectively trap activated EGFR in the pit by binding to both the receptor and the pit superstructure. It is important to note that the exact state of the pre-formed pits before cargo recruitment is relatively unknown, but that cargo recruitment is essential for the process to continue. In the event that proper cargo is not recruited to the pit, the entire process will abort and the involved proteins (and the pit itself) will disassemble.[42-44] Towards the end of the pit lifetime, a protein called dynamin is recruited that is strongly associated with vesicle scission.[45-47] Although it has been shown that dynamin hydrolizes GTP and is essential for vesicle scission, dynamin activity alone is not sufficient to account for the pinching off of vesicles.[45,46,48] A recent model proposes that dynamin serves to sterically hinder phosphatases from accessing phosphatidylinositol 4,5-bisphosphate (PIP_2) molecules at binding sites, and that preferential hydrolysis of exposed PIP_2 molecules gives rise to an interfacial force that results in scission.[49] It should be noted that this model has yet to be explicitly demonstrated in mammalian cells, however. After scission, the EGFR cargo is sorted into early endosomes and is eventually trafficked either to lysozomes for degradation or back to the surface in the recycling pathway.[36] In some cases where the local membrane tension is high, the actin cytoskeleton will be cross-linked to pits to assist their formation.[50] See Figure 1.5 for a visual summary of these processes.

The process of clathrin-mediated endocytosis is a prime example of the criticality of mechanical force to cell biology. In order to deform the membrane and bud off a vesicle, force must be exerted. These forces are generated through protein self-assembly as well as hydrolysis of integral lipid molecules and polymerization of the cytoskeleton. Prior to the work presented herein, there were few techniques capable of studying the mechanical tension exerted through individual receptors during mechanically active processes. Chapter 2 describes the development of a novel method for this purpose, and uses this method to quantify the forces exerted during clathrin-mediated endocytosis of the EGFR. Furthermore, the dynamics of clathrin-mediated endocytosis are extremely difficult to study, owing to the sub-diffraction limit size of clathrin-coated pits and the fast time scales on which protein assembly events occur. Chapter 4 describes a fluorescence microscopy imaging technique that is capable of nanoscale resolution at millisecond imaging intervals, overcoming some of the barriers to real-time characterization clathrin-mediated endocytosis.

1.3 The aims and scope of this dissertation.

As described in section 1.2, the signaling networks of the EGFR are quite well understood, as evidenced by the fact that the EGFR signaling pathway can be traced through a multitude of branches from each of its many ligands all the way to the transcriptional level. In spite of this, many questions still remain about EGFR function. For example, the most widely accepted model of EGFR activation focuses on receptor dimerization that has been shown to be critical to promote ligand-receptor interaction and properly align the kinase domains for transphosphorylation.[19,22] More recent work, however, has revealed that the EGFR is capable of forming larger oligomer structures, and the function of these assemblies remains unknown.[26-28] Further questions stem from the involvement of the EGFR in clathrin-mediated endocytosis. The involvement of mechanical force in the process is likely due to the degree of membrane deformation involved, but to date no direct measurement of force transduction on the receptor during the process of internalization has been reported. Some of the important remaining questions surrounding the EGFR include the following:

1) Does the endocytosis of the EGFR involve mechanical force, and what magnitude of force is applied during the process?
2) Does clustering of the EGFR affect its signal output, and if so, in what way?

3) What are the spatiotemporal dynamics of EGFR z position during recruitment to clathrin coated pits?

In order to answer these questions, it is necessary to develop new methods to characterize the EGFR. In general, this dissertation focuses on the development of new methods as a first step towards the investigation of these long-standing questions. Chapter 2 describes the development of a novel fluorescent force sensor that is capable of characterizing the forces exerted by cell surface receptors in real time. This platform is used in investigating the forces exerted during EGFR endocytosis and provides the first quantitative measurement thereof. In chapter 3 we investigate the role of large-scale (>500 nm) EGFR oligomers (clusters) that form when EGFR is exposed to membrane-tethered ligand. This phenomenon is studied using the supported lipid bilayer technique, in which lipid bilayers are formed on glass surfaces and functionalized with EGF that remains laterally mobile. Supported lipid bilayers are patterned with nanoscale diffusion barriers that control clustering of the EGFR, thus allowing the elucidation of the effect of cluster formation on signaling. Chapter 4 describes the development of a new fluorescence microscopy technique, simultaneous two-wavelength axial ratiometry (STAR) that allows super-resolution imaging of samples along the optical axis with the speed of standard epifluorescence imaging. This method allows access to much faster time domains than traditional super-resolution approaches and is capable of accurate measurement even when target proteins undergo dynamic self-assembly processes. Accordingly, STAR was used to study the real-time (ms) dynamics of EGFR internalization with nanometer accuracy, providing new insight into a process that has been traditionally difficult to study in living cells.

Finally, chapter five gives a final perspective on the dissertation as a whole with summaries and detailed commentary on future directions for each chapter. The findings presented herein not only demonstrate new methods that allow access to difficult to answer questions about biological systems, but also represent a first step toward a more complete understanding of EGFR function. Future experiments will focus primarily on the maturation of the methods described within this dissertation towards application to other difficult to study biological questions. Through refinement of these techniques, it is our hope that they will be widely adopted and assist the scientific community at large in investigating difficult-to-study biological questions in other systems.

1.4 References

1. Cohen, S., *J Biol Chem* **234** (5), 1129 (1959).

2. Cohen, S., *J Biol Chem* **237**, 1555 (1962).

3. Cohen, S. and Elliott, G. A., *The Journal of Investigative Dermatology* **40** (1), 1 (1963).

4. Cohen, S., *Developmental Biology* **12** (3), 394 (1965).

5. Carpenter, G., Lembach, K. J., Morrison, M. M., and Cohen, S., *Journal of Biological Chemistry* **250** (11), 4297 (1975).

6. Cohen, S., Carpenter, G., and King, L., *Journal of Biological Chemistry* **255** (10), 4834 (1980).

7. Ushiro, H. and Cohen, S., *Journal of Biological Chemistry* **255** (18), 8363 (1980).

8. Ullrich, A., Coussens, L., Hayflick, J. S., Dull, T. J., Gray, A. et al., *Nature* **309** (5967), 418 (1984).

9. Garrett, T. P. J., McKern, N. M., Lou, M., Elleman, T. C., Adams, T. E. et al., *Cell* **110** (6), 763 (2002).

10. Stamos, J., Sliwkowski, M. X., and Eigenbrot, C., *Journal of Biological Chemistry* **277** (48), 46265 (2002).

11. Sealy, L., Privalsky, M. L., Moscovici, G., Moscovici, C., and Bishop, J. M., *Virology* **130** (1), 155 (1983).

12. Yamamoto, T., Hihara, H., Nishida, T., Kawai, S., and Toyoshima, K., *Cell* **34** (1), 225 (1983).

13. Nicholson, R. I., Gee, J. M. W., and Harper, M. E., *European Journal of Cancer* **37, Supplement 4** (0), 9 (2001).

14. Barker, A. J., Gibson, K. H., Grundy, W., Godfrey, A. A., Barlow, J. J. et al., *Bioorganic & Medicinal Chemistry Letters* **11** (14), 1911 (2001).

15. Martinelli, E., De Palma, R., Orditura, M., De Vita, F., and Ciardiello, F., *Clinical & Experimental Immunology* **158** (1), 1 (2009).

16. Soulieres, D., Senzer, N. N., Vokes, E. E., Hidalgo, M., Agarwala, S. S. et al., *Journal of Clinical Oncology* **22** (1), 77 (2004).

17. Alvarado, D., Klein, D. E., and Lemmon, M. A., *Nature* **461** (7261), 287 (2009).

18. Ferguson, K. M., Berger, M. B., Mendrola, J. M., Cho, H.-S., Leahy, D. J. et al., *Molecular cell* **11** (2), 507 (2003).

19. Zhang, X., Gureasko, J., Shen, K., Cole, P. A., and Kuriyan, J., *Cell* **125** (6), 1137 (2006).

20. Jorissen, R. N., Walker, F., Pouliot, N., Garrett, T. P. J., Ward, C. W. et al., *Experimental Cell Research* **284** (1), 31 (2003).

21. Yu, X., Sharma, K. D., Takahashi, T., Iwamoto, R., and Mekada, E., *Molecular Biology of the Cell* **13** (7), 2547 (2002).

22. Moriki, T., Maruyama, H., and Maruyama, I. N., *Journal of Molecular Biology* **311** (5), 1011 (2001).

23. Chung, I., Akita, R., Vandlen, R., Toomre, D., Schlessinger, J. et al., *Nature* **464** (7289), 783 (2010).

24. Mattoon, D., Klein, P., Lemmon, M. A., Lax, I., and Schlessinger, J., *Proceedings of the National Academy of Sciences of the United States of America* **101** (4), 923 (2004).

25. Cao, H., Bangalore, L., Dompe, C., Bormann, B., and Stern, D., *Journal of Biological Chemistry* **267** (28), 20489 (1992).

26. Abulrob, A., Lu, Z., Baumann, E., Vobornik, D., Taylor, R. et al., *Journal of Biological Chemistry* **285** (5), 3145 (2010).

27. Yang, S., Raymond-Stintz, M. A., Ying, W., Zhang, J., Lidke, D. S. et al., *Journal of Cell Science* **120** (16), 2763 (2007).

28. Nagy, P., Claus, J., Jovin, T., and Arndt-Jovin, D., *Proceedings of the National Academy of Sciences* **107** (38), 16524 (2010).

29. Yarden, Y. and Sliwkowski, M. X., *Nat Rev Mol Cell Biol* **2** (2), 127 (2001).

30. Biscardi, J. S., Maa, M.-C., Tice, D. A., Cox, M. E., Leu, T.-H. et al., *Journal of Biological Chemistry* **274** (12), 8335 (1999).

31. Rappoport, J. Z. and Simon, S. M., *Journal of Cell Science* **122** (9), 1301 (2009).

32. Haglund, K., Shimokawa, N., Szymkiewicz, I., and Dikic, I., *Proceedings of the National Academy of Sciences* **99** (19), 12191 (2002).

33. Jiang, X., Huang, F., Marusyk, A., and Sorkin, A., *Molecular Biology of the Cell* **14** (3), 858 (2003).

34. Blagoev, B., Kratchmarova, I., Ong, S.-E., Nielsen, M., Foster, L. J. et al., *Nat Biotech* **21** (3), 315 (2003).

35. Leaman, D. W., Pisharody, S., Flickinger, T. W., Commane, M. A., Schlessinger, J. et al., *Molecular and Cellular Biology* **16** (1), 369 (1996).

36. Roepstorff, K., Grandal, M. V., Henriksen, L., Knudsen, S. L. J., Lerdrup, M. et al., *Traffic* **10** (8), 1115 (2009).

37. Vieira, A. V., Lamaze, C., and Schmid, S. L., *Science* **274** (5295), 2086 (1996).

38. Prenzel, N., Zwick, E., Daub, H., Leserer, M., Abraham, R. et al., *Nature* **402** (6764), 884 (1999).

39. Singh, A. B. and Harris, R. C., *Cellular Signalling* **17** (10), 1183 (2005).

40. Kirchhausen, E. C. F. A. S. B. T., Aguet, F., Boulant, S., and Kirchhausen, T., *Cell* **150** (3), 495 (2012).

41. Goh, L. K., Huang, F., Kim, W., Gygi, S., and Sorkin, A., *The Journal of Cell Biology* **189** (5), 871 (2010).

42. Ehrlich, M., Boll, W., van Oijen, A., Hariharan, R., Chandran, K. et al., *Cell* **118** (5), 591 (2004).

43. Cureton, D. K., Massol, R. H., Saffarian, S., Kirchhausen, T. L., and Whelan, S. P., *PLoS pathogens* **5** (4), e1000394 (2009).

44. Loerke, D., Mettlen, M., Yarar, D., Jaqaman, K., Jaqaman, H. et al., *PLoS biology* **7** (3), e1000057 (2009).

45. Pucadyil, T. J. and Schmid, S. L., *Cell* **135** (7), 1263 (2008).

46. Marks, B., Stowell, M. H. B., Vallis, Y., Mills, I. G., Gibson, A. et al., *Nature* **410** (6825), 231 (2001).

47. Mattheyses, A. L., Atkinson, C. E., and Simon, S. M., *Traffic* **12** (10), 1394 (2011).

48. Itoh, T., Erdmann, K. S., Roux, A., Habermann, B., Werner, H. et al., *Developmental cell* **9** (6), 791 (2005).

49. Liu, J., Sun, Y., Drubin, D. G., and Oster, G. F., *PLoS biology* **7** (9), e1000204 (2009).

50. Boulant, S., Kural, C., Zeeh, J.-C., Ubelmann, F., and Kirchhausen, T., *Nat Cell Biol* **13** (9), 1124 (2011).

Chapter 2: Visualizing Mechanical Tension Across Membrane Receptors with a Fluorescent Sensor

Adapted from Stabley, D.R., Jurchenko, C., Marshall, S.S., Salaita, K.S., Visualizing Mechanical Tension Across Membrane Receptors with a Fluorescent Sensor, *Nat. Meth.* **2012**, 9 (1), 64-67, with permission from the Nature Publishing Group.

2.1 Introduction

The interplay between physical inputs and chemical reaction cascades coordinates a diverse set of biological processes that range from epithelial cell adhesion and migration to stem cell differentiation and immune response[1,2]. The majority of these mechanical inputs are sensed and transduced through membrane receptors that mount a signaling cascade that is dependent on the mechanical properties of their specific cognate ligands[2]. A major challenge to elucidating the molecular mechanisms of mechanotransduction lies in the development of tools that can measure forces applied to specific receptors on the cell surface[3]. To address this challenge, two main classes of techniques have been developed. The first class employs single-molecule force spectroscopy (SMFS) methods such as atomic force microscopy (AFM), and optical or magnetic tweezers to measure forces at specific sites on the cell surface[3,4]. These approaches provide key proof-of-concept measurements for cell surface receptors, but the inherent serial nature of SMFS methods coupled with the need for statistically significant data sets in cell biology has thus far hampered their wide-spread adoption[4]. The second category of approaches to measuring biophysical forces in vivo is the genetically encoded protein tension sensors[5-7]. These sensors are comprised of three domains that include a pair of fluorescent proteins linked to an elastic amino-acid domain and inserted into a suitable site within a host protein. Fluorescent-protein tension sensors are gaining widespread use due to the biocompatible, non-invasive, and high-throughput nature of fluorescence imaging. However, up to 30% of all human genes are predicted to encode for membrane-associated proteins[8], and the vast majority of these proteins and many cytoplasmic proteins will not regain wild-type function upon splitting and insertion of the three domains within the host protein. Therefore, in the absence of methods for measuring mechanical tension across the hundreds or thousands of proteins on the cell membrane or structurally sensitive soluble proteins, elucidating chemo-mechanical couplings will remain a significant challenge.

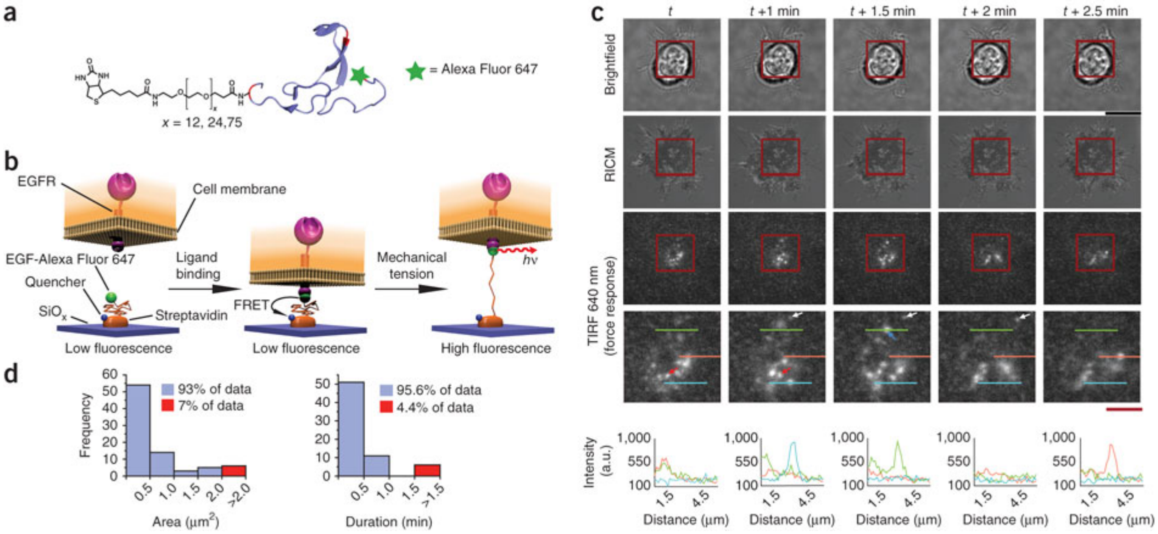

Figure 2.1: Design and response of the EGFR tension sensor.

(**a**) Schematic of the EGF-PEG*x* (*x* = 12, 24 or 75) tension sensor, comprised of a PEG polymer of length *x* that is flanked by fluorescently labeled (Alexa Fluor 647) EGF ligand and a biotin moiety for surface immobilization via streptavidin capture. EGF crystal structure adapted from Protein Data Bank (identifier IJL9). Residues in red in the crystal structure represent lysine and the N terminus, which are the available sites for PEG and fluorophore modification. (**b**) Schematic of the mechanism of sensor function. When EGFR exerts a force on its ligand, the flexible PEG linker extends. The displacement of the EGF ligand results in an increase in the measured fluorescence intensity, thus reporting the transmission of mechanical tension through the EGF-EGFR complex. *hv*, emission of a photon. (**c**) Representative brightfield, reflection interference contrast microscopy (RICM) and EGFR tension sensor TIRF response of HCC1143 cells plated onto sensor surfaces at 37 °C for the indicated time points (*t* represents the start of imaging). Images on the bottom show magnification of the boxed regions. Colored line scans represent 34 pixel profiles through the indicated region; the color of each line corresponds to the graph shown below each set of frames. The white, red and blue arrows highlight fluorescent spots that persisted for 90 s, 60 s and 30 s, respectively. Black scale bar, 20 µm; red scale bar, 4 µm. Fluorescence intensity is given in arbitrary units (a.u.). (**d**) Histograms of the areas (*n* = 82) and the durations (*n* = 68) of fluorescent points under a cell that was observed for 10 min.

2.2 Sensor Design and Fabrication

Herein we developed a molecular tension sensor capable of spatial and temporal mapping of forces exerted by cell surface receptors. The sensor consists of a flexible linker that is covalently conjugated to a biological ligand at one terminus and anchored onto a surface such that mechanical forces do not result in sensor translocation (**Fig. 2.1a-b**). The ligand and the surface are functionalized with fluorophore and quencher molecules, respectively. Cellular forces exerted on the ligand will extend the linker from its relaxed conformational state and remove the fluorophore from proximity to the quencher, thus displaying increased fluorescence intensity and providing a signal to map mechanical tension transduced through specific receptor targets (**Fig. 2.1b).** Due to the inherent properties of fluorescence imaging, the approach is, in principle, non-invasive and can map forces with single molecule spatial resolution and high temporal resolution in living cells. Importantly, this method only requires the use of a conventional fluorescence microscope and precludes the necessity of genetic engineering of target receptors. The flexible linker in the molecular sensor is comprised of a polyethylene glycol (PEG) polymer that was selected over polypeptide or oligonucleotide chains because of its unique properties that include: a) well-characterized and reversible

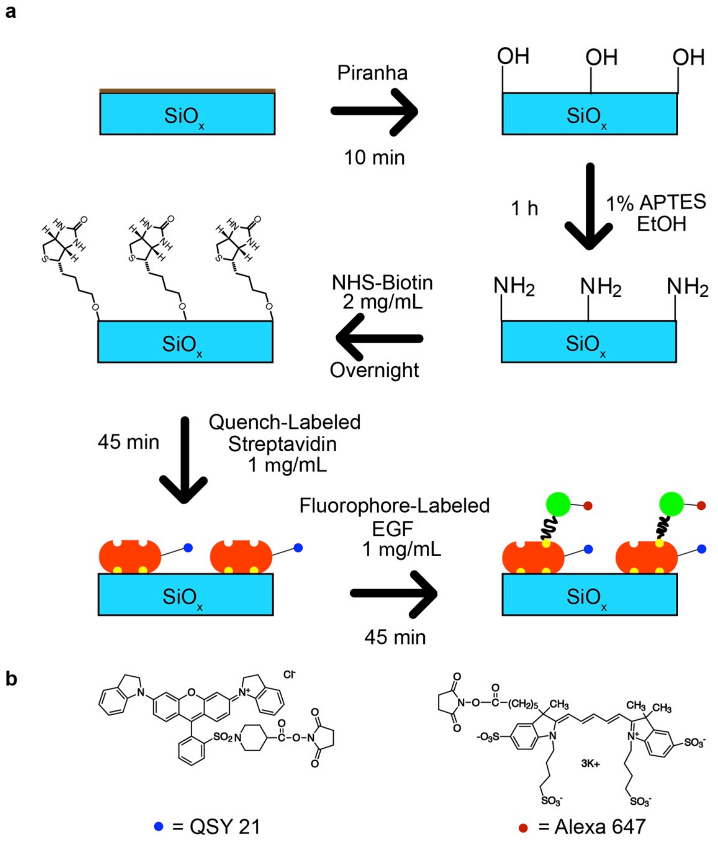

Figure 2.2: Fabrication of glass surface-functionalized force sensors.

(**a**) Schematic describing the steps used to generate the force biosensors. See methods section for detailed description. (**b**) Molecular structures of the reactive NHS esters of QSY 21 and Alexa 647.

force-extension curves[9,10] , b) biocompatibility[11], and c) minimal non-specific interactions with other biomolecules[12].

As a proof-of-concept, we employed the molecular force sensor to map out forces associated with initial uptake and trafficking of the epidermal growth factor receptor

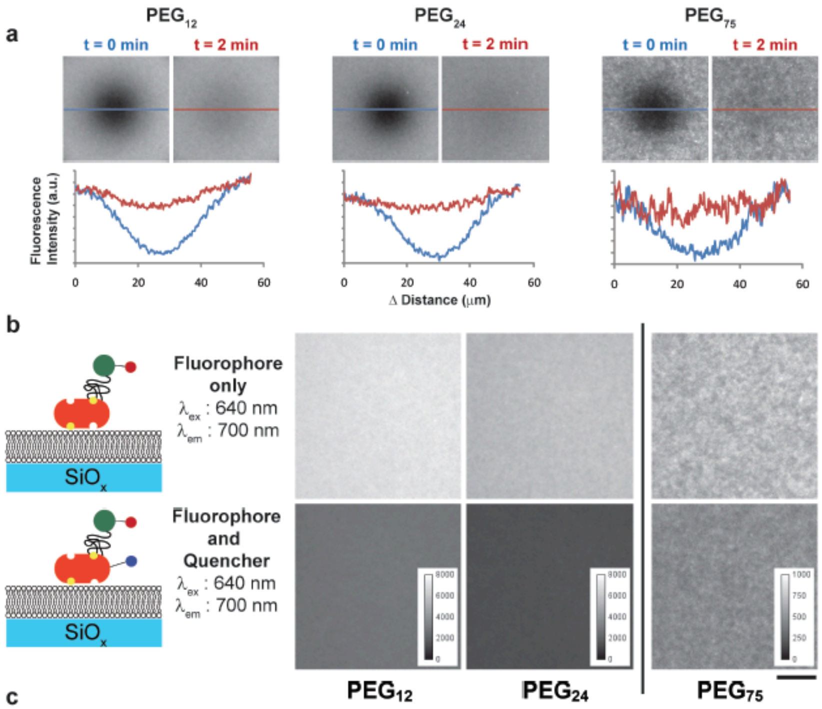

c

	PEG12	PEG24	PEG75
Measured Quenching Efficiency	0.79 ± 0.01	0.85 ± 0.02	0.48 ± 0.03
Fluorophore-Quencher Distance (nm)	5.5 ± 0.1	5.2 ± 0.2	7.0 ± 0.2
Predicted Distance Based on Flory Model (nm)	4.6	5.4	7.7

Figure 2.3: Zero-force conformation of the sensor.

(**a**) The force sensor surfaces are laterally fluid as indicated by FRAP (fluorescence recovery after photobleaching) experiments. Line plots show the fluorescence intensity immediately after photobleaching (blue) and the fluorescence intensity 2 min after recovery (red). (**b**) The resting state of EGF-PEG_{12}, EGF-PEG_{24}, and EGF-PEG_{75} sensors was determined by measuring the fluorescence intensity of surfaces containing the sensor in the absence (top row) and in the presence (bottom row) of the quencher. (**c**) The quenching efficiency for each surface was then calculated, and the experimental distance between chromophores in the resting state was determined and compared to the distance calculated from the Flory radius of each PEG polymer (see methods for calculation details). All measurements were taken in 1x PBS at RT. Error represents SEM, *n* = 3. Scale bar is 10 μm.

(EGFR) upon binding to its cognate ligand. The EGFR pathway plays important roles in cell survival, proliferation, and differentiation, and internalization is an important regulatory component within the normal physiology of this pathway[13]. Importantly, the EGFR pathway is one of the most widely studied experimental systems for investigating ligand-induced receptor endocytosis. A fundamental question in the molecular mechanism of ligand-induced receptor endocytosis pertains to the role and even the existence of forces in shuttling the receptor from the cell membrane to endosomal compartments[3]. It seems rational then to conclude that the process of endocytosis requires the application of a force to transport the EGFR-EGF complex, but specific evidence is thus far lacking[14]. We synthesized tension sensors that present the EGF ligand and specifically measure force transmission through the EGFR (**Fig. 2.2**). In order to characterize the conformation of the sensor in the resting state, i.e. in the absence of cellular forces, the EGF-PEG conjugate was tethered to a fluid supported lipid bilayer (SLB). The SLB surface provides a well-controlled bio-mimetic environment in which the protein density can be quantitatively measured and tuned[15]. The sensors are homogeneously displayed on the laterally mobile SLB surface as indicated by fluorescence recovery after photobleaching (FRAP) (**Fig. 2.3a**). Quantitative fluorescence resonance energy transfer (FRET) efficiency measurements show that the force sensor conjugates adopt a condensed mushroom-like conformation with the EGF located 5.5 ± 0.1 nm, 5.2 ± 0.2 nm, and 7.0 ± 0.2 nm from the surface for the EGF-PEG_{12}, EGF-PEG_{24}, and EGF-PEG_{75} linkers, respectively (**Fig. 2.3b**). These distance values suggest that the EGF-PEG_{24} and EGF-PEG_{75} linkers adopt their predicted Flory radii[9,10,16].

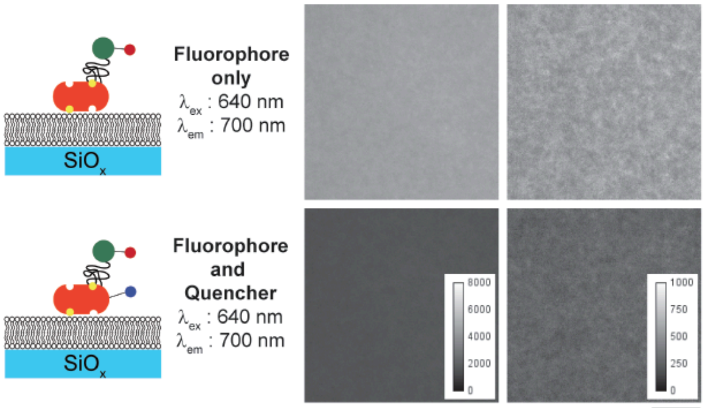

	PEG_{24}	**PEG_{75}**
Measured Quenching Efficiency	0.81 ± 0.03	0.58 ± 0.04
Fluorophore-Quencher Distance (nm)	5.4 ± 0.2	6.6 ± 0.3
Predicted Distance Based on Flory Model (nm)	5.4	7.7

Figure 2.4: Zero-force conformation of the sensor at physiological conditions.

Representative fluorescence images of the EGF-PEG_{24} and EGF-PEG_{75} force sensor surfaces that were generated either with labeled or unlabeled streptavidin. The PEG sensor conformation was determined using equations 1 and 2 as described in Supplementary Fig. 2. The conformation of the sensor at 37 °C is similar to that shown previously for the sensor at 25 °C (Fig. 3). Error represents the standard deviation of intensity measurements from ten different areas across two separate surfaces. Scale bar is 10 μm.

Consequently, the resting state structures of the EGF-PEG_{75} and EGF-PEG_{24} sensor conjugates are at ~25% and ~57%, respectively, of their full contour lengths, which implies that the fluorescence intensity is expected to increase significantly as the PEG linkers are fully extended. Although the conformation of PEG polymers in solution is temperature and solvent dependent[9,16], we found that the equilibrium conformation of the force sensor is not significantly altered at physiological conditions (37 °C and 1x PBS) (**Fig. 2.4**). Therefore, these data, along with experimental and theoretical literature precedent investigating the force extension of PEG polymers and their protein conjugates[9,10,17,18], predict that the dynamic range of the EGF-PEG force sensors will directly depend on the length of the PEG linker. For example, the dynamic range of EGF-PEG_{24} conjugates is expected to fall between 0 and 20 pN, and >95% of the maximum fluorescence intensity will be observed with the application of a 20 pN force (**Fig. 2.5**).

This range is compatible with the range of forces inherent to many biological processes[1,3,5].

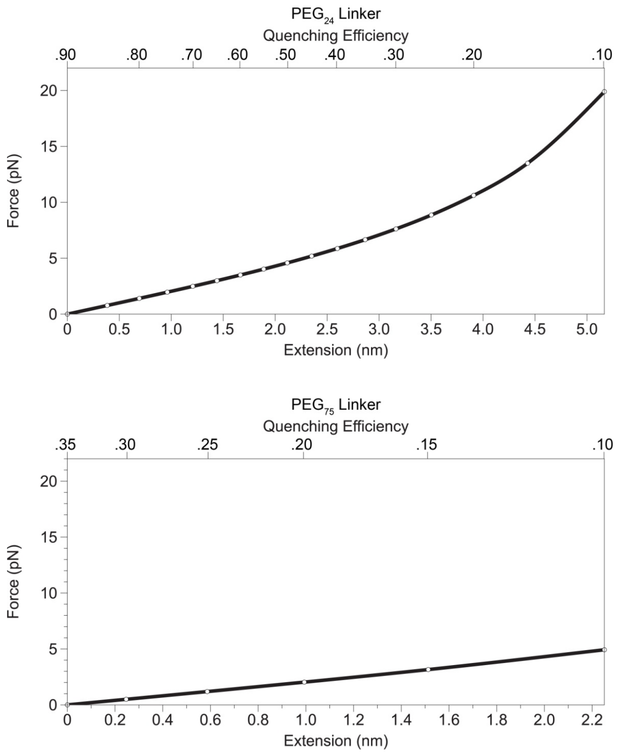

Figure 2.5: Theoretical plots of PEG$_{24}$ and PEG$_{75}$ extension and quenching efficiency as a function of applied force.

The extended worm-like chain model (WLC) was used to generate a plot of the applied forces as a function of linker displacement, which is calculated from quenching efficiency (Eqn. 3-7). A range of quenching efficiencies from 10% to 90% was converted into PEG extension lengths using the FRET relation for the QSY 21 Alexa 647 quencher-fluorophore pair (Eqn. 4). The zero force resting state distance between the chromophores was calculated by subtracting the resting state of the polymer and the dimensions of the EGF and streptavidin proteins from the simulated distances. The resting state of the PEG$_{24}$ linker was determined experimentally and corresponds to the polymer length at 90% quenching efficiency, while the PEG$_{75}$ linker resting state was determined from the Flory model. The displacement from this resting state distance was then converted into a force using the extended WLC model. The PEG$_{24}$ linker displays a wider dynamic range compared to PEG$_{75}$ given the polymer conformations and the Förster radius of the QSY 21 and Alexa 647 pair.

2.3 Imaging Force in Live Cells

When immortalized human breast cancer cells (HCC1143) were engaged to the EGF force sensor surface, receptors expressed in the cell membrane bound to their cognate ligands. Within 20-30 min of cell spreading, transient and localized increases in fluorescence intensity were observed in time-lapse total internal reflection fluorescence (TIRF) microscopy, which exclusively probes molecules within 100-150 nm of the substrate (**Fig. 2.1c**). The bright spots were diffraction limited (**Fig. 2.1c-d**), thus suggesting that the observed events are localized to punctate points that experience mechanical tension. Further analysis revealed that the localized increases in fluorescence are short lived, seldom persisting beyond 30 s, and that there is a range of lifetime distributions for points across the cell-substrate contact plane (**Fig. 2.1c-d**). The fluorescence intensity at these spots then returned to the background level, which indicates that the fluorophore-labeled EGF remains bound to the sensor surface. Significant photobleaching is typically not observed under these time-lapse imaging conditions during the first 20-30 frames. The recovery of the fluorescence intensity to the background level after the transient increase may be a consequence of ligand-receptor dissociation or diminished cellular pulling, and it is not possible to distinguish between these two events within these experiments. The mechanism of complete internalization is most likely stalled because the ligand is tethered to the substrate, and thus the measured mechanical forces are associated with the initial steps of ligand uptake.

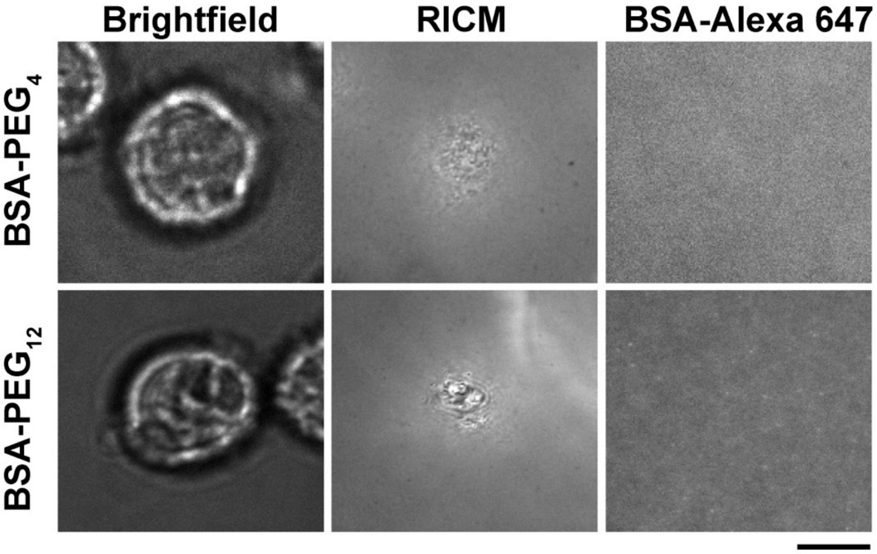

Figure 2.6: Specific EGF-EGFR interactions are required to activate the force sensor.

Representative brightfield, RICM, and epifluorescence images of two cells on the indicated force sensor SLB (at *t* = 30 min) . The fluorescence channel does not show any localized increases in signal, thus suggesting that a specific ligand-receptor interaction is necessary for force sensor activation. Scale bar is 10 μm.

Given that a wide array of adhesion receptors may interact with the underlying substrate, we tested the specificity of the optical force sensor to the EGF receptor using three different sets of control experiments. First, BSA-force sensor conjugates were synthesized and cells were plated onto these substrates. The BSA-conjugates underneath the cells displayed no fluorescence response under TIRF imaging at t = 30 min (**Fig. 2.6**). Second, we pretreated cells with 1.7 nM soluble EGF for 5 min, then plated these cells onto the EGF-force sensor surfaces, and also did not observe an optical response (**Fig. 2.7**). Finally, to determine the role of an apposed ligand in the specificity of the force response, a cyclic RGD (Arg-Gly-Asp) peptide ligand was incorporated into the BSA-force sensor surface. Unlike the first two controls, cells strongly engaged these surfaces, as indicated by reflection interference contrast microscopy (RICM) imaging but no significant fluorescence response was observed (**Fig. 2.8**). Taken together, these experiments confirm that the measured responses are specific to force transmission through the EGF receptor.

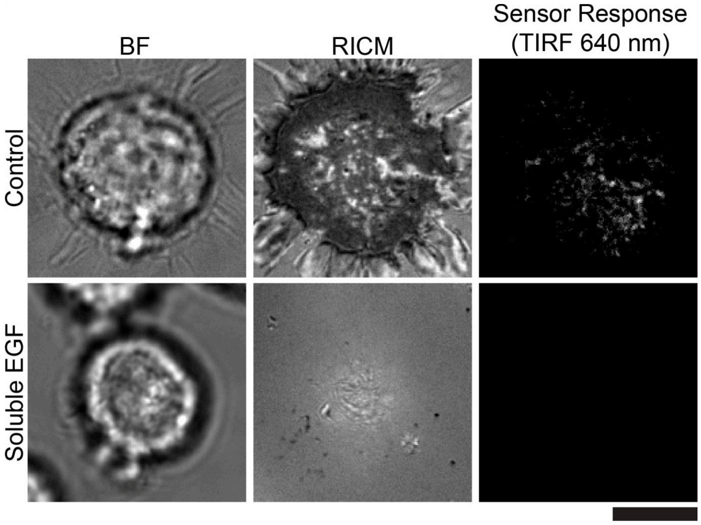

Figure 2.7: Force Sensor response requires a specific ligand-receptor interaction.

Cells were plated on an EGF functionalized sensor surface either in the presence or absence of soluble EGF ligand (1.7 nM). Cells treated with soluble EGF exhibited poor adhesion to the surface and did not trigger a force sensor response, whereas control cells adhered strongly and generated the characteristic response. This indicates that the force sensor response is primarily mediated by the EGF-EGFR interaction. Scale bar is 10 µm.

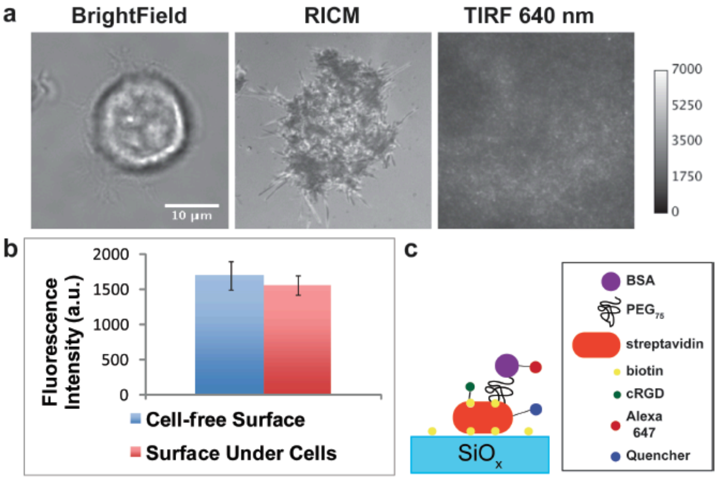

Figure 2.8. Specific EGF-EGFR interactions are required to activate the force sensor: role of apposed ligand.

Brightfield, RICM, and TIRF (640 nm) images of a representative cell plated on a force sensor functionalized glass substrate. Cyclic RGD peptide (10 nM, Peptides Int'l) and BSA-PEG$_{75}$-Alexa 647 (15 nM) were co-adsorbed to the surface in order to provide two apposing ligands. The cRGD peptide engages integrins and enhances adhesion while the BSA provides a control force sensor ligand. The brightfield and RICM images (**a**) indicate that the cells are engaged to the surface. The TIRF image does not show any observable localized increases in signal, thus confirming that a specific ligand-receptor interaction is necessary for force probe response. (**b**) Comparison of the fluorescence intensities observed for the blank sensor surface with the area under the cells does not show a significant difference. Analysis represents the average of 10 cells. Error bars represent standard deviation. (**c**) Scheme depicting the BSA control force sensor.

To examine the role of the PEG linker and the specific fluorophore (Alexa 647) - quencher (QSY 21) pair (Förster radius, R_0 = 6.9 nm according to the manufacturer) in the observed fluorescence response, cell tension measurements were performed with sensors displaying short linkers (contour length = 2.2 nm) or with sensors that lacked the quencher tags. In these experiments, the force response was quantified at the single cell level and normalized to the background signal (**Fig. 2.9**). Experiments with force probes synthesized with the 2.2 nm linker showed minimal response when compared to the 26 nm PEG$_{75}$ linkers (**Fig. 2.10a**). Similarly, sensors that lack the quencher do not display a significant signal (**Fig. 2.10a, Fig. 2.11**). To eliminate the possibility that direct ligand-receptor binding may lead to sensor response, EGF-force probe surfaces were treated with monoclonal EGF antibody. This treatment did not result in a sensor response (**Fig. 2.12**). To ensure that the biological activity of the EGF ligand was not influenced by the length (flexibility) of the different linkers, cells were immunostained with an antibody specific to pY 1068 of EGFR to measure the relative activation levels. Single-cell fluorescence analysis indicated no significant differences in immunostaining levels between cells that were activated with tension sensor surfaces that employed 2.2 nm or 26 nm linker contour lengths, thus showing that cells were similarly activated (**Fig. 2.13**). Overall, these experiments show that the molecular sensor requires a flexible linker that is appropriately matched to the Förster radius of the dye pair, and that this approach provides for an optical and non-invasive approach for generating receptor-specific mechanical tension image maps.

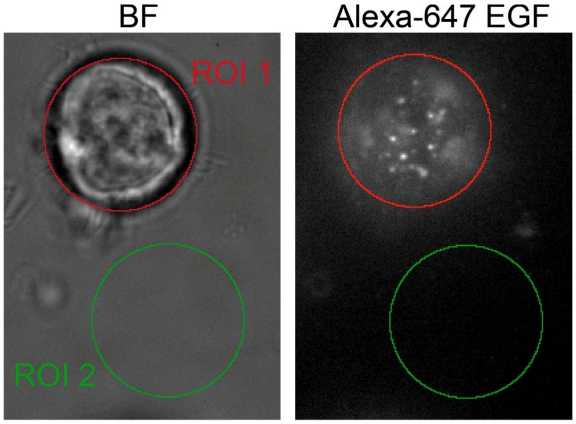

Figure 2.9: Data analysis of force sensor response.

Using the brightfield images as a guide, each Alexa 647 EGF image is analyzed by placing a circular region of interest (ROI) over the area of a cell (ROI 1 (red) in images) as well as placing an ROI over an off-cell area (ROI 2 (green) in images). The average intensity of the fluorescence signal in each ROI is measured, and the mean intensity of ROI 1 is divided by the mean intensity of ROI 2. This is repeated for many cells, and the quotients are averaged into a mean, generating the normalized fluorescence increase values used in plots. The error reported is that of the measured quotients.

2.4 Correlating Force to Endocytosis

EGF endocytosis is thought to primarily proceed through an internalization pathway that is mediated through the cytoskeleton and clathrin-coated pits[13]. In order to provide evidence for the role of the cytoskeleton in mechanotransduction, cells were treated with Latrunculin B (LatB, - a cytoskeletal inhibitor that targets the assembly of F-actin). This led to a 70% reduction in sensor response, indicating that physical tension is dependent on proper

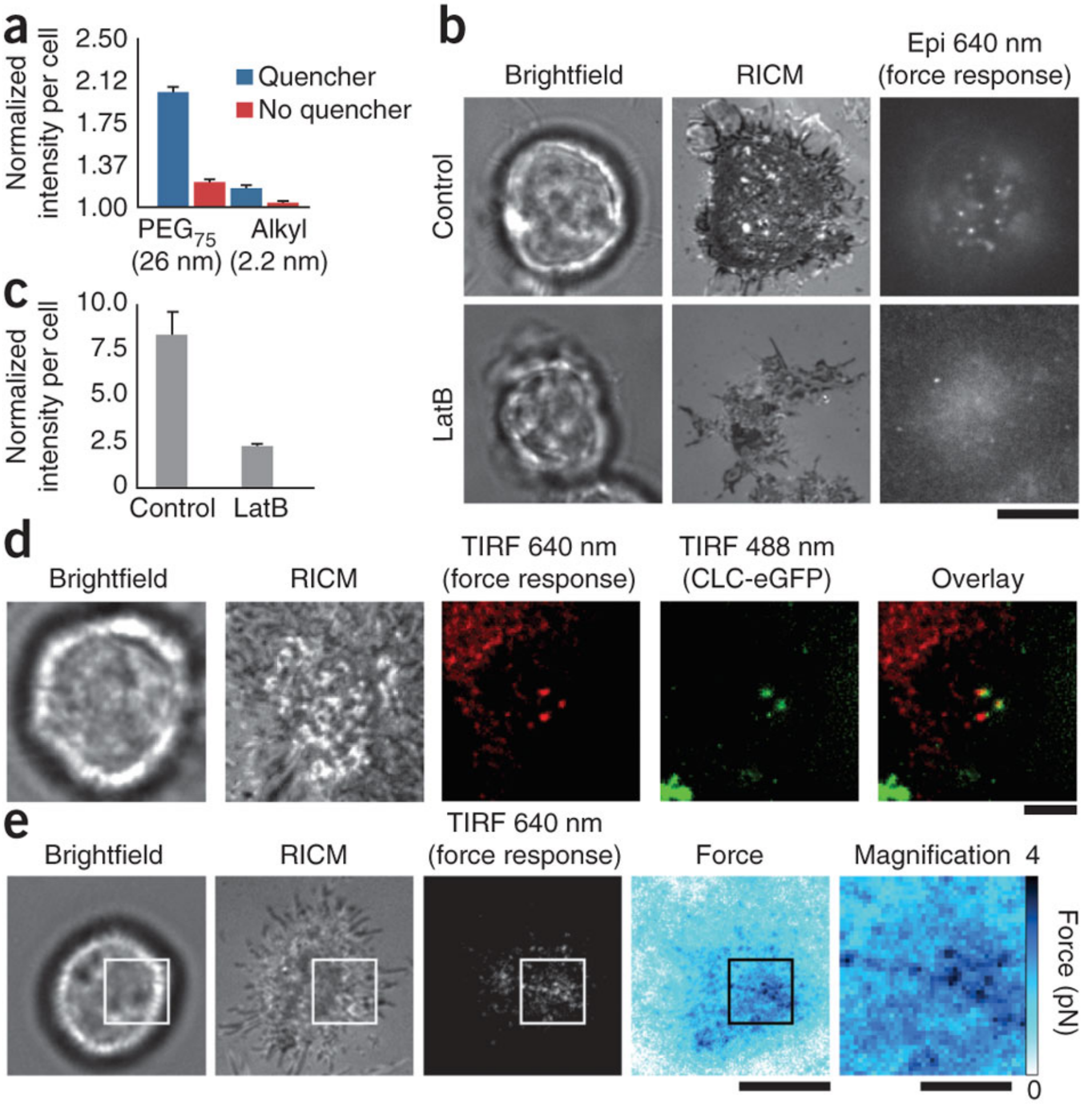

Figure 2.10: Characterization and quantification of the EGFR tension sensor.

(**a**) Role of the flexible linker (alkyl, 2.2 nm or PEG75, 26 nm) and the quencher in the EGFR tension sensor response. Error bars, s.e.m. (*n* = 77 cells). (**b**) Representative brightfield, reflection interference contrast microscopy (RICM) and EGFR tension sensor response (epifluorescence (epi) 640 nm) channels for cells treated with latrunculin B (LatB) or control (DMSO). Scale bar, 5 μm. (**c**) Measured EGF force response (normalized fluorescence intensity) between LatB-treated (*n* = 33 cells) and untreated (*n* = 32 cells). Error bars, s.e.m. (**d**) Representative dual channel TIRF microscopy images of a *CLC-eGFP*–transfected cell engaged to the force-sensing surface. Overlay channel shows colocalization of CLC-eGFP and the EGF-force response. Scale bar, 5 μm. (**e**) Representative brightfield, RICM and fluorescence response for a cell engaged to an EGF-PEG24 force sensor surface. The sensor fluorescence response was converted into a force map by using the extended WLC model for PEG24. Scale bars, 10 μm (3.2 μm in the magnified image).

function of the cytoskeleton (**Fig. 2.10b-c**). To confirm that mechanical force is associated with clathrin-coated pit invagination, the HCC1143 cells were transiently transfected with a clathrin light chain-eGFP construct (CLC-eGFP). Live-cell dual-channel TIRF microscopy was performed to measure the association of CLC-eGFP with the EGFR tension sensor. Diffraction-limited bright spots were observed in both fluorescence channels (**Fig. 2.10d**). Taken together, the average lifetimes and dimensions of the punctate points along with actin-dependence and clathrin-colocalization data all confirm that the mechanical pulling events are consistent with a clathrin-mediated EGF internalization mechanism[19].

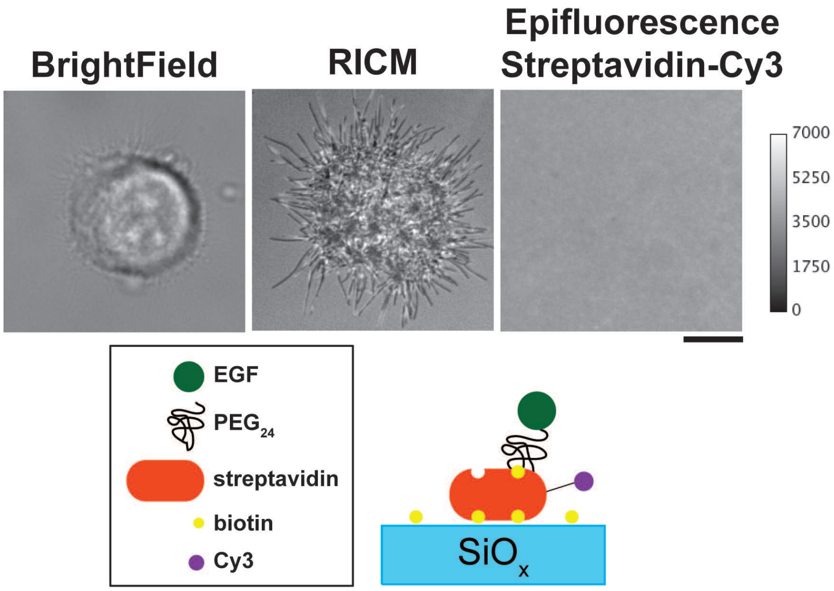

Figure 2.11: Cell binding does not induce clustering of sensor.

HCC1134 cells were incubated for 30 min on surfaces functionalized with EGF-PEG$_{24}$-streptavidin-Cy3. Brightfield and RICM images show that the cell engaged the surface. Fluorescence images of the Cy3 channel do not show any observable clustering, which confirms that the streptavidin is immobile on the glass substrate. Scale bar is 10 μm.

2.5 Quantification of Force Signals

The current sensor design allows for precise quantification of the magnitude of the applied force required to extend the PEG linker from its resting state. The physical extension of the linker was determined from the FRET relation, and this displacement was then used to estimate the mechanical tension using the extended worm-like chain (WLC) model[9,10,17]. This conversion is possible due to the fact that PEG is a well-

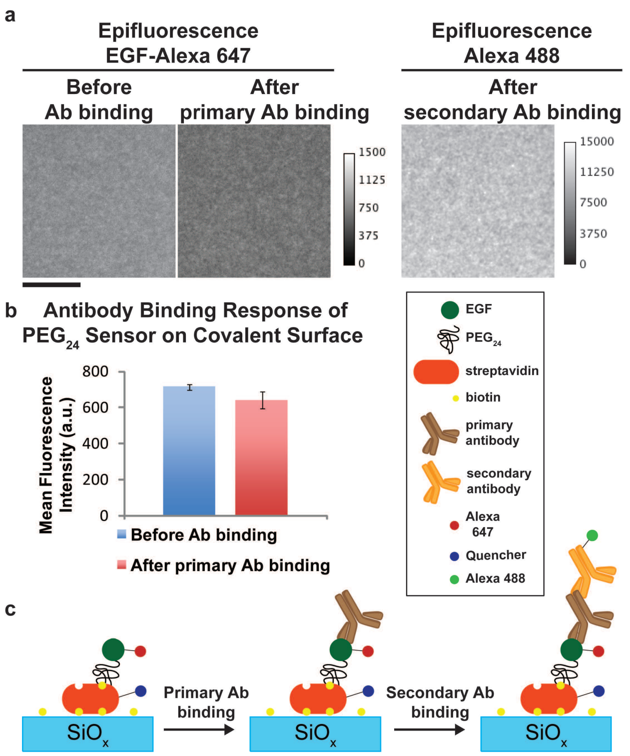

Figure 2.12: Binding of EGF antibody to EGF ligand does not trigger the force sensor.

Surfaces were covalently functionalized with the force sensor containing EGF ligand as described previously. (**a**) Representative fluorescence images of the force sensor surface before and after binding of primary EGF antibody (5 µg ml^{-1}, R&D Systems). To confirm binding of antibody to the surface, the primary antibody surfaces were incubated with secondary IgG antibody-Alexa 488 (2.5 mg ml^{-1}, Invitrogen). (**b**) Bar graph showing the mean fluorescence intensity of force sensor surface before (blue) and after (red) addition of the primary antibody. Error represents the standard deviation of 10 different regions on each surface. (**c**) Scheme depicting the predicted antibody binding to the force sensor surface.

behaved polymer whose force extension profile experimentally fits the extended WLC with high accuracy (less than 1% error) in 1 x PBS buffer[17] (**see Methods and Fig. 2.14**). We employed mono-labeled EGF-PEG$_{24}$ conjugates because of their broad dynamic range for force quantification. A representative force map was generated for a cell that engaged the EGF tension sensor for 30 min (**Figure 2.10e**). The punctate fluorescent regions show a peak force value of approximately 4 pN, which represents the ensemble average force applied by the EGF receptor on that area. This is the first quantification of the forces exerted by EGFR and provides a lower bound of mechanical tension.

2.6 Conclusion

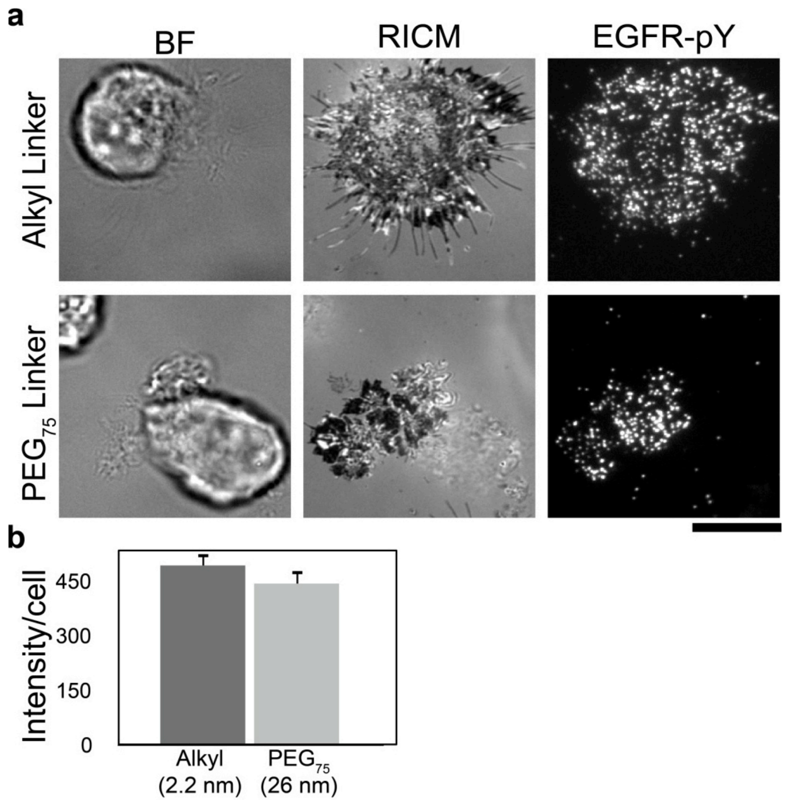

Figure 2.13: The activity of EGF ligand is independent of linker length.

HCC1143 cells were serum starved for 18 h and plated onto sensor surfaces in supplemented RPMI media at 37 ˚C and incubated for approximately 30 min, after which cells were imaged live (see methods for imaging details). (**a**) Representative brightfield, images of two cells that were incubated onto the indicated sensor surface and then fixed and stained with anti-EGFR-pY 1068 antibody (Cell Signaling Technologies 3777s). Scale bar is 12µm. (**b**) Graph showing the average background-subtracted fluorescence intensity of cells immunostained for EGFR-pY 1068. Intensity indicates the level of receptor phosphorylation remains similar for both the alkyl and PEG$_{75}$ linkers. Error bars represent the standard error of the mean (SEM). Alkyl, *n* = 52 cells; PEG$_{75,}$ *n* = 47 cells.

In summary, we report on the development of a general method for mapping the mechanical tension that is experienced by specific membrane proteins on the surface of living cells. As a proof-of-concept, we generate tension maps that provide the first direct evidence showing that mechanical forces are associated with the initial stages of EGF ligand internalization. This method can be applied to nearly any receptor, and thus opens the door to rapidly studying chemo-mechanical interactions across the thousands of membrane-bound receptors on the surface of virtually any cell type. The inherent flexibility of the platform may also enable the investigation of mechanical force transmission across cell-cell junctions, such as those between T-cells and antigen-presenting cells, as well as epithelial cell junctions, which are typically not amenable to direct investigations by other methods.

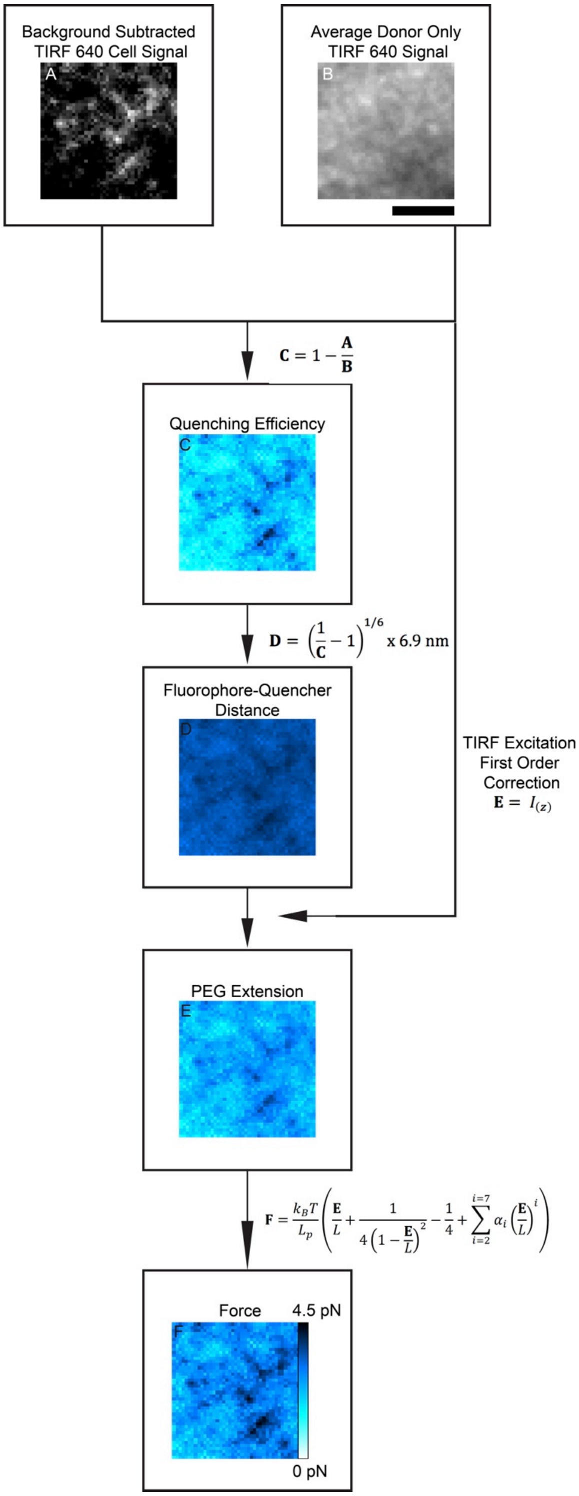

Figure 2.14: Flow chart of data analysis for converting quenching efficiency to force maps.

In order to quantify the forces detected by the sensor, a series of image operations were performed. First, the background subtracted TIRF 640 image (**A**) was divided by a composite donor only signal image (**B**) to generate a quenching efficiency image map (**C**). Note that (**B**) is an average of the signal over five regions of the donor only sample. The quenching efficiency map is then converted to a distance map (**D**) using the FRET relationship. This distance map is then used to perform a first order correction for TIRF excitation intensity falloff. After the dimensions of EGF streptavidin and the resting state of the polymer were subtracted out, the *z* extension of PEG was mapped (**E**). This extension image was then converted to force (**F**) using the extended WLC model (see Methods for more details). Scale bar is 3.2 µm.

2.7 Methods

Synthesis and Characterization of Streptavidin-Quencher Conjugates

A streptavidin labeling ratio of one was desired in order to accurately use the FRET relation and determine the zero-force conformation of the sensor. Recombinant streptavidin (Rockland Immunochemicals) was labeled with quencher by mixing 300 μg of the protein in 150 μL of 1x phosphate buffered saline (PBS, 10 mM phosphate buffer, 137 mM NaCl) with 15 μL of 1 M sodium bicarbonate and a 20 fold molar excess of QSY 21 NHS ester (Invitrogen). The reaction was allowed to proceed for 60 min at RT on a rotating platform. Purification was performed by size exclusion chromatography using Bio-Gel P4 resin (Bio-Rad) swollen with 1x PBS. The final product was characterized using MALDI-TOF and absorbance spectrometry. The labeling ratio was determined to be 0.8 by UV-Vis absorbance measurements of the gel-purified product.

For all other experiments, recombinant streptavidin was labeled with quencher by mixing 1 mg ml^{-1} of the protein in 1 x PBS with an excess of QSY 21 NHS ester. The reaction was allowed to proceed for 60 min at RT, and the tube was inverted every 15 min to ensure proper mixing. The product was purified with a Slide-a-Lyzer MINI dialysis column (Thermo Fisher) with a cutoff of 3,500 g mol^{-1} following manufacturer recommendations and performing a 30 min dialysis in a 2 L bath of 1x PBS twice. The final product was characterized using MALDI-TOF and absorbance spectrometry. Empirically, we found that a 5 fold molar excess of QSY 21 achieved a labeling ratio of approximately 0.9-1.1. In contrast, a 20 fold molar excess of QSY 21 yielded streptavidin with a labeling ratio of approximately 2 when using this method, based on UV-Vis absorbance measurements.

Synthesis and Characterization of EGF-PEG Conjugates

EGF was simultaneously labeled with a flexible biotinylated PEG linker (PEG_{12}, Thermo Scientific; PEG_{24}, Quanta Biodesign; PEG_{75}, Nanocs) and fluorescent dye (Alexa 647, Invitrogen) in a single pot reaction using standard NHS bioconjugation chemistry. A mono-labeled product for both PEG and dye was desired for quantitative experiments. The optimal reaction concentrations were empirically determined to be 120 μM EGF, 0.1 M sodium bicarbonate, and a 5 fold molar excess of both the biotin-PEG NHS ester and the Alexa 647 NHS ester. The reaction was incubated on a rotating platform at RT for 30 min and purified using the Bio-Gel P6 resin (Bio-Rad). MALDI-TOF mass spectrometry and UV-Vis were used to determine the overall EGF:PEG:dye ratio (data not shown). Mass spectrometry indicated that the predominant product under these reaction conditions had an EGF:PEG:dye ratio of 1:1:1. Note that other EGF:PEG:dye stoichiometries existed in the sample, the most abundant of which was dual labeled with dye but not conjugated to the biotin-PEG anchor (1:0:2), and therefore would not adhere to the streptavidin functionalized surfaces.

In some cases, EGF was labeled with biotinylated PEG_{75} (Nanocs) and Alexa 647 (Invitrogen) in a step-wise fashion. First, 10 μL of 1 M sodium bicarbonate was added to 100 μL of EGF (1 mg mL^{-1}), then 20 fold molar excess of Alexa 647 NHS ester was added and the reaction allowed to proceed for 10 min at RT. Subsequently, a 15 fold molar excess of biotin-PEG_{75} NHS ester was added to the reaction mixture and allowed to incubate for an additional 30 min. The reaction was purified using Bio-Gel P6 resin (Bio-Rad). The final labeling ratio of dye:protein, as measured by UV-Vis absorbance, was 0.8. The EGF that was used for the alkyl linker controls was labeled in a single pot reaction with NHS-Sulfo-LC-LC-Biotin (Pierce) and Alexa 647 NHS ester (Invitrogen). 20 μL of 1 M sodium bicarbonate was added to 200 μL of 1 mg mL^{-1} EGF, after which a 20 fold molar excess of both biotinylated linker and dye was added. After reagent addition, the reaction was incubated for 1 h at RT and inverted every 15 min to ensure mixing. The reaction mixture was subsequently purified with Bio-Gel P4 resin (Bio-Rad), yielding EGF with an Alexa 647 labeling ratio of 1.9.

Cell Culture

HCC1143 cells were cultured in RPMI 1640 media (Mediatech) supplemented with 10% FBS (Mediatech), HEPES (9.9 mM, Sigma), Sodium Pyruvate (1 mM, Sigma), L-glutamine (2.1 mM, Mediatech), penicillin G (100 IU mL^{-1}, Mediatech) and streptomycin (100 μg mL^{-1}, Mediatech) and were incubated at 37 °C with 5% CO_2. Cells were passaged at 90-100% confluency and plated at a density of 50% using standard cell culture procedures. All experiments were conducted with HCC1143 cells that had been serum starved for ~18 h.

Functionalization of Glass Substrate Biosensors (Figure 2.2)

Glass coverslips were functionalized based on literature precedent[20]. Briefly, glass coverslips (No. 2 - 25mm diameter, VWR) were sonicated in Nanopure water (18.2 mΩ) for 10 min and then etched in piranha (a 3:1 mixture of sulfuric acid (Avantor Performance Materials) and hydrogen peroxide (Sigma)) for 10 min - please take caution - piranha is extremely corrosive and may explode if exposed to organics. The glass coverslips were then washed twice in a beaker of Nanopure water (18.2 mΩ) and placed into three successive wash beakers containing EtOH (Decon Labs) and left in a final fourth beaker containing 1% (3-aminopropyl)triethoxysilane (APTES, Sigma) in EtOH for 1 h. The substrates were then immersed in the EtOH three times and subsequently rinsed with EtOH and dried under nitrogen. Substrates were further baked in an oven (~100 °C) for 10 min. After cooling, the samples were incubated with NHS-Biotin (Thermo Fisher) at 2 mg mL^{-1} in dry DMSO (Sigma) overnight. Subsequently, the substrates were washed with EtOH and dried under nitrogen. The substrates were then washed with 1x PBS (3 x 5 mL aliquots) and incubated with BSA (EMD Chemicals, 100 µg µL^{-1}, 30 min) and washed again with 1x PBS (3 x 5 mL aliquots). Quench labeled streptavidin was then added (1 µg mL^{-1}, 45 min, RT) followed by washing with 1x PBS (3 x 5 mL aliquots) and incubating with the desired EGF construct (biotinylated linker and fluorophore labeled, 1 µg mL^{-1}, 45 min, RT). Substrates were then rinsed with a final wash of 1x PBS (3 x 5 mL aliquots) and used within the same day.

Functionalization of Supported Lipid Bilayers

Lipids consisted of 99.9% 1,2-dioleoyl-*sn*-glycero-3-phosphocholine (DOPC, Avanti Polar Lipids) and 0.1% 1,2-dioleoyl-*sn*-glycero-3-phosphoethanolamine-N-(cap biotinyl) (sodium salt) (DPPE-biotin, Avanti Polar Lipids). After being mixed in the correct proportions in chloroform, lipids were dried with a rotary evaporator and placed under a stream of N_2 to ensure complete evaporation of the solvent. These lipid samples were then resuspended in Nanopure water and subjected to 3 freeze/thaw cycles by alternating immersions in an acetone and dry ice bath and a warm water bath (40 °C). To obtain small unilamellar vesicles (SUV's) lipids were extruded through a high-pressure extruder with a 100 nm nanopore membrane (Whatman).[21]

Supported lipid bilayers (SLB) were assembled by adding SUV's to base etched 96 well plates with glass-bottomed wells. At the biotinylated lipid doping concentration used (0.1%) the calculated streptavidin density is 690 molecules per μm^2 and therefore it is expected that streptavidin bound to the surface is at sufficiently low density to avoid fluorophore self quenching[22]. This is confirmed by measuring fluorescence intensity as a function of biotin doping concentration (data not shown). After blocking with BSA (0.1 mg mL^{-1}) for 30 min, bilayer surfaces were incubated with either unlabeled streptavidin (1 µg 400 μL^{-1}) or streptavidin QSY 21 (1 µg 400 μL^{-1}) for one h. Wells were rinsed 3 times with 5 mL of 1x PBS, then incubated with EGF-PEG$_x$-Alexa 647 (100 nM) for 1 h and rinsed 3x with 5 mL of 1x PBS before imaging.

Characterization of the Zero-Force Sensor Conformation

FRET efficiency was measured using Eqn. 1,

$$E = \left(1 - \frac{I_{DA}}{I_D}\right)\frac{1}{f_A} \qquad \text{Eqn.1}$$

where I_{DA} refers to the intensity of the EGF-PEG$_x$-Alexa 647 surface containing quench labeled streptavidin, I_D is the intensity of the EGF-PEG$_x$-Alexa 647 surface with unlabeled streptavidin and f_A is the labeling ratio of the acceptor[23]. These values were obtained by averaging the fluorescence intensity measured in 5 different areas for each substrate. The reported values are the average of three independent experiments. The calculated efficiency for each surface was then used to determine the average distance between fluorophore and quencher by,

$$E = \frac{1}{1+\left(\frac{r}{R_0}\right)^6} \qquad \text{Eqn. 2}$$

where R_0 is the Förster distance of the dye pair (6.9 nm according to the manufacturer) and r is the average distance between the fluorophores[23]. The predicted value for r was determined by adding the PEG Flory radius to the radii of the proteins that comprise the force sensor. The protein radius for EGF was estimated at 1 nm based on its crystal structure [PDB: 2KV4], and for streptavidin the radius was estimated at 2 nm based on the crystal structure [PDB: 1SWB]. The predicted r value was then compared to the FRET measured r value and reported in Supplementary Fig. 2.

Fluorescence Microscopy

Live cells were imaged in serum free RPMI 1640 (Mediatech) media formulated as described in the cell culture section at 37 °C, and fixed cells were imaged in 1% BSA in 1x PBS at RT. During imaging, physiological temperatures were maintained with a warming apparatus consisting of a sample warmer and an objective warmer (Warner Instruments part no.'s 641674D and 640375). The microscope used was an Eclipse *Ti* driven by the Nikon Elements software package (Nikon). The microscope features an Evolve EM CCD (Photometrics), an Intensilight epifluorescence source (Nikon), a CFI Apo 100x (NA = 1.49) objective (Nikon), and a TIRF launcher with two laser lines: 488 nm (10 mW) and 640 nm (20 mW). This microscope also includes the Nikon Perfect

Focus System, an interferometry-based focus lock that allowed the capture of multipoint and time-lapse images without loss of focus. The microscope is equipped with the following Chroma filter cubes: TIRF 488, TIRF 640, Cy5, and RICM.

Image Analysis

Images from sensor experiments are processed (using a custom macro in imageJ (NIH)) from a single multipoint image file into individual tiff stacks containing each imaging channel. Separate macros are then used to isolate and background subtract the Alexa 647 EGF force channel. For all images, the LUT is linear and represents the full range of data as represented by the calibration bar accompanying each image set. Analysis of images was performed with ImageJ and Nikon Elements software packages. ND2 image processing was done with several custom imageJ macros (available upon request) in combination with the LOCI bio-formats plugin (University of Wisconsin), as well as the Nikon Elements software package. Sensor spot duration analysis was performed manually with the assistance of the SpotTracker 2D (Daniel Sage, École polytechnique fédérale de Lausanne) and Multi Measure (Wayne Rasband) ImageJ plugins.

Quantitative Force Maps

In order to determine the absolute magnitude of forces detected by the sensor, a series of image operations were performed. First, the quenching efficiency image map was derived from the background subtracted TIRF 640 sensor signal image by using equation 3,

$$C = 1 - \frac{A}{B} \qquad \text{Eqn. 3}$$

where A is the background subtracted TIRF 640 sensor signal image, B is the average TIRF 640 image of a donor-only force probe obtained from a sample lacking the quencher, and C is the resulting image which is a map of the quenching efficiency. Next, an image mapping the distance between the fluorophore and quencher was obtained by rearranging the FRET relation and applying equation 4,

$$D = R_0\left(\frac{1}{C} - 1\right)^{\frac{1}{6}} \qquad \text{Eqn. 4}$$

where R_0 is the Förster radius of the quencher-fluorophore pair, and D is the resulting distance map[23]. This fluorophore-quencher distance image is then used to correct for the TIRF excitation intensity, since the evanescent field intensity drops off exponentially in the z axis. The penetration depth of the TIRF evanescent field is determined by equation 5,

$$d = \frac{\lambda}{4\pi\sqrt{n_2^2 Sin^2\theta - n_1^2}} \qquad \text{Eqn. 5}$$

where d is the penetration depth of the evanescent field, n_2 is the index of refraction of glass (1.51), n_1 is the index of refraction of water (1.33), λ is the wavelength (640 nm), and θ is the incident angle of the laser (~65°)[23]. The penetration depth can then be used along with the distance map to determine the corrected TIRF excitation intensity at each pixel. This is accomplished by applying equation 6,

$$S = Be^{-D}/d \qquad \text{Eqn. 6}$$

where S is the scalar correction image, B is the donor only averaged image, D is the distance map image, and d is the penetration depth of the evanescent field. The product of multiplying S by B gives the illumination intensity corrected distance map, E. To determine the average PEG resting conformation, the dimensions of EGF and streptavidin were subtracted from the corrected distance map, *E*. To calculate the extension of PEG from this resting state, the PEG resting state conformation was subtracted from the entire image. Finally, a quantitative force map was inferred by applying the extended worm-like chain (WLC) model to the distance map. The extended worm-like chain approximation is made by applying equation 7 to image *E*,

$$F = \frac{k_B T}{L_p}\left(\frac{E}{L} + \frac{1}{4\left(1-\frac{E}{L}\right)^2} - \frac{1}{4} + \sum_{i=1}^{i=7} \alpha_i \left(\frac{E}{L}\right)^i\right)$$

Eqn. 7

where *F* is the resulting quantitative force map image, k_B is the Boltzman constant, *T* is the temperature, L_p is the persistence length of PEG (0.38 nm), *E* is the corrected distance map, and *L* is the end-to-end length of PEG_{24} (8.4 nm)[17].

Determination of EGFR Phosphorylation and Activation

HCC1143 cells were seeded onto the biosensor surfaces displaying EGF and incubated on the substrates for 30 min at 37 °C. Following initial imaging, the cells were fixed with 4% paraformaldehyde (Sigma) in 1x PBS and permeabilized with 0.1% TritonX (Sigma) in 1x PBS. Cells were then blocked overnight in 1% BSA at 4 °C. The next day, cells were incubated with anti-EGFR-pY-1068 primary antibody (Cell Signaling Technologies 3777s) at 1:200 dilution for 1 h at RT. The primary antibody was then washed out with 1x PBS and the cells were incubated with Alexa-488 Anti-Rabbit IgG secondary antibody (Invitrogen) at 1:1000 dilution for 45 min. The secondary antibody was then rinsed out with 1x PBS and the sample was imaged in TIRF mode at

488 nm as well as in the Alexa 647, brightfield, and RICM channels using an epifluorescence source.

Actin Inhibition

HCC1143 cells were serum starved for approximately 18 h and split into two aliquots, one of which was treated with 4 µm Latrunculin B (Sigma) for 30 min in DMSO (EMD Chemicals), while the other was treated with an equivalent amount of DMSO. Each aliquot was then plated onto an EGF functionalized biosensor surface and incubated for 30 min at 37 °C. Cells were then imaged in the Alexa 647, BF, and RICM channels.

CLC-eGFP Transfection

HCC1143 cells were seeded on a 24 well plate in antibiotic-free media at a density of ~300,000 cells per well overnight. The cells were then transfected with the CLC-eGFP construct using Lipofectamine 2000 (Invitrogen) and following standard transfection protocols. These cells were then serum starved overnight and used for experiments as indicated within 24 h of the transfection.

2.8 Author Contributions and Acknowledgments

Author Contributions

D.S. adapted the FRET surface sensor for use with human cells expressing the EGFR and performed the majority of the human cell experiments. C.S. developed the force sensor and performed the quantitative characterization of the zero-force sensor conformation and its components. S.M. optimized and performed the CLC-eGFP transfections. K.S. was responsible for devising the overall experimental strategy.

Acknowledgements

We thank Alexa Mattheyses for the CLC-eGFP plasmid, Rita Nahta for the HCC1143 cells, as well as Daniel Sage for the SpotTracker 2D ImageJ plugin, Wayne Rasband for the MultiMeasure ImageJ plugin, and Ulf Dittmer for the Expression ImageJ plugin. We would also like to acknowledge the Winship Cancer Center for logistics support. K.S. acknowledges the Georgia Cancer Coalition Cancer Research Award for its support.

2.9 References

1. Vogel, V. and Sheetz, M., *Nat. Rev. Mol. Cell Biol.* **7** (4), 265 (2006).
2. DuFort, C. C., Paszek, M. J., and Weaver, V. M., *Nat. Rev. Mol. Cell Biol.* **12**, 308 (2011).
3. Dufrene, Y. F., Evans, E., Engel, A., Helenius, J., Gaub, H. E. et al., *Nat. Methods* **8** (2), 123 (2011).
4. Muller, D. J., Helenius, J., Alsteens, D., and Dufrene, Y. F., *Nat. Chem. Biol.* **5**, 383 (2009).
5. Grashoff, C., Hoffman, B. D., Brenner, M. D., Zhou, R., Parsons, M. et al., *Nature* **466**, 263 (2010).
6. Iwai, S. and Uyeda, T. Q. P., *Proc. Natl. Acad. Sci. U.S.A.* **105** (44), 16882 (2008).
7. Meng, F. and Sachs, F., *J. Cell Sci.* **124**, 261 (2011).
8. Krogh, A., Larsson, B., von Heijne, G., and Sonnhammer, E. L. L., *Journal of Molecular Biology* **305** (3), 567 (2001).
9. Oesterhelt, F., Rief, M., and Gaub, H. E., *New J. Phys.* **1** (6), 6.1 (1999).
10. Kienberger, F., Pastushenko, V. P., Kada, G., Gruber, H. J., Riener, C. et al., *Single Molecules* **1** (2), 123 (2000).
11. Roberts, M. J., Bentley, M. D., and Harris, J. M., *Adv. Drug Deliv. Rev.* **54** (4), 459 (2002).
12. Harder, P., Grunze, M., Dahint, R., Whitesides, G. M., and Laibinis, P. E., *J. Phys. Chem. B* **102** (2), 426 (1998).

13. Goh, L. K., Huang, F., Kim, W., Gygi, S., and Sorkin, A., *J. Cell Biol.* **189** (5), 871 (2010).

14. Martin, A. C., Welch, M. D., and Drubin, D. G., *Nat. Cell Biol.* **8**, 826 (2006).

15. Salaita, K., Nair, P. M., Petit, R. S., Neve, R. M., Das, D. et al., *Science* **327** (5971), 1380 (2010).

16. de Gennes, P. G., *Macromolecules* **13**, 1069 (1980).

17. Bouchiat, C., Wang, M. D., Allemand, J. F., Strick, T., Block, S. M. et al., *Biophys. J.* **76** (1), 409 (1999).

18. Sulchek, T. A., Friddle, R. W., Langry, K., Lau, E. Y., Albrecht, H. et al., *Proc. Natl. Acad. Sci. U.S.A.* **102** (46), 16638 (2005).

19. Saffarian, S., Cocucci, E., and Kirchhausen, T., *PLoS Biol.* **7** (9), e1000191 (2009).

20. Clack, N. G., Salaita, K., and Groves, J. T., *Nat. Biotech.* **26** (7), 825 (2008).

21. Nair, P. M., Salaita, K., Petit, R. S., and Groves, J. T., *Nat. Protocols* **6** (4), 523 (2011).

22. Galush, W. J., Nye, J. A., and Groves, J. T., *Biophys. J.* **95** (5), 2512 (2008).

23. Lakowicz, J. R., *Principles of Fluorescence Spectroscopy*, 3 ed. (Springer, New York, 2006).

Chapter 3: Manipulating the Lateral Diffusion of Surface-Anchored EGF Demonstrates that Receptor Clustering Modulates Phosphorylation Levels

Adapted from Stabley, D., Retterer, S., Marshall, S, and Salaita, K., Manipulating the Lateral Diffusion of Surface-Anchored EGF Demonstrates that Receptor Clustering Modulates Phosphorylation Levels, *Integr. Biol.* **2013**, 5 (4), 659-668, with permission from The Royal Society of Chemistry.

3.1 Introduction

Cellular communication is vital for the survival of multicellular organisms, and dictates cellular processes that range from tissue patterning and organization to mounting an immune response to specific threats. Much of the information exchanged between cells is in the form of chemical signals that are received and interpreted by thousands of receptors found in the cell membrane. While the field has generally been focused on chemical inducers that regulate specific pathways, recent evidence has shown that the spatial organization of cell surface receptors on length scales spanning the molecular to the size of the cell itself can also play a role in cellular signal regulation.[1-4] Some of the earliest evidence suggesting that oligomerization of membrane receptors plays a role in signaling comes from studies of the FCεRI receptor, where oligomers showed increasing levels of activation in comparison to monomers and dimers.[5] Further experiments making use of synthetic multivalent ligands have likewise revealed signaling outcomes that are unique to multivalent ligands.[6,7]

Many membrane receptors, including the toll-like,[8] EGF,[9-17] ErbB family,[17,18] T-cell,[2,19,20] Fas (CD95),[21-23] and Ephrin[1] have been found to assemble into higher-order structures comprised of tens to thousands of receptors whose signaling levels are correlated to cluster formation. In the immunological synapse, it has been observed that spatial patterning of antigens and their cognate T-cell receptors dictates the intensity of T-cell activation.[2,19,24] Recent studies have also shown that levels of metalloprotease recruitment to the EphA2 receptor is related to receptor clustering.[1,25] Additionally, progressive clustering of Fas (CD95) induced by ligand binding has been shown to stabilize the individually weak interactions of the death-induced signaling complex.[23]

These results suggest that signal transduction is not exclusively the result of ligand-receptor binding, and is rather an ensemble process that transcends chemical recognition to include supramolecular organization and spatial patterning within the fluid membranes of cells. In light of this, a more detailed understanding of how ligand organization influences cell signaling pathways is needed in order to achieve system-level control of cell fate and function.

The epidermal growth factor receptor (EGFR) is one of the most well studied receptors in cell biology, and is a member of the ErbB family of receptor tyrosine kinases that also includes ErbB2 (HER2), ErbB3, and ErbB4. It has long been a receptor of interest due to its involvement in many types of cancer, and was one of the first mitogenic receptors to be characterized.[26] In the conventional model of EGFR activation, the receptor binds its ligand (EGF) and undergoes dimerization and autophosphorylation, thus triggering a signaling cascade that proceeds to the transcriptional level.[18,27] Homo- and hetero-dimerization are hallmarks of ErbB family signaling, and these dynamic receptor associations have broad biochemical and biomedical significance.[18]

Several lines of biophysical studies confirm the formation of EGFR clusters across different cell line models. For example, near-field scanning optical fluorescence microscopy (a super-resolution imaging technique) provided high-resolution images of ligand-bound EGFR clusters on the surface of fixed HeLa cells. The data showed that cells formed a range of cluster sizes with an average diameter of 150 nm ± 80 nm after 10 min of ligand incubation.[10] Another validation comes from an investigation using transmission electron microscopy (TEM) of gold nanoparticle-antibody conjugates specific for EGFR which showed the assembly of nanometer scale clusters on the surface of SKBR3 cells.[28] Image correlation spectroscopy (ICS) and its derivative techniques have also contributed to the quantification and characterization of EGFR clustering. Number and brightness analysis (a type of ICS) revealed the formation of EGFR oligomers in A431 cells after 30 min of EGF treatment. Importantly, these oligomers contained three-fold higher levels of phosphorylated molecules of EGFR than bound EGF molecules.[29] In another study, imaging of surface plasmon coupling between gold nanoparticles attached to EGFR revealed the formation of large EGFR assemblies on the surface of A431 cells but cluster size was not quantified.[17] Förster resonance energy transfer-fluorescence lifetime imaging microscopy (FRET-FLIM) imaging in combination with ICS also showed that ligand bound and activated EGFR exists primarily as a higher-order oligomer, and that clusters of activated EGFR contain at minimum four times the amount of receptor as inactive clusters in HEK293 cells.[13] When combined with flow cytometry, FRET-FLIM data showed that after ligand treatment, EGFR homocluster size increased from 4 to 10 molecules per cluster on the surface of A431 cells.[14] Finally, single molecule tracking experiments showed a slowed rate of EGFR diffusion within 20 s of ligand binding, which suggested that EGFR forms large oligomers.[9] Taken together, these experiments indicate that upon ligand binding EGFR assembles into clusters that may contain tens to tens of thousands of molecules and diffuse as a single unit in the plasma membrane.

One of the major challenges in the field pertains to developing a quantitative relationship between EGFR clustering and receptor activation. To address this goal, we use the recently developed nanopatterned supported lipid bilayer technique along with surface immobilization methods to control EGFR clustering levels in living cells and then quantify the effect of EGFR organization on its phosphorylation levels.[1,30] We find that large-scale clustering of EGFR dampens its phosphorylation intensity in HCC1143 breast cancer cells, and that kinase and cytoskeleton activity, and endocytosis machinery contribute to this clustering behavior.

3.2 Experimental Platforms to Study EGFR Clustering

To investigate the role of EGFR cluster formation on activation levels, it is necessary to use methods that allow one to externally control receptor clustering within the cell membrane and to measure its corresponding level of activation within individual

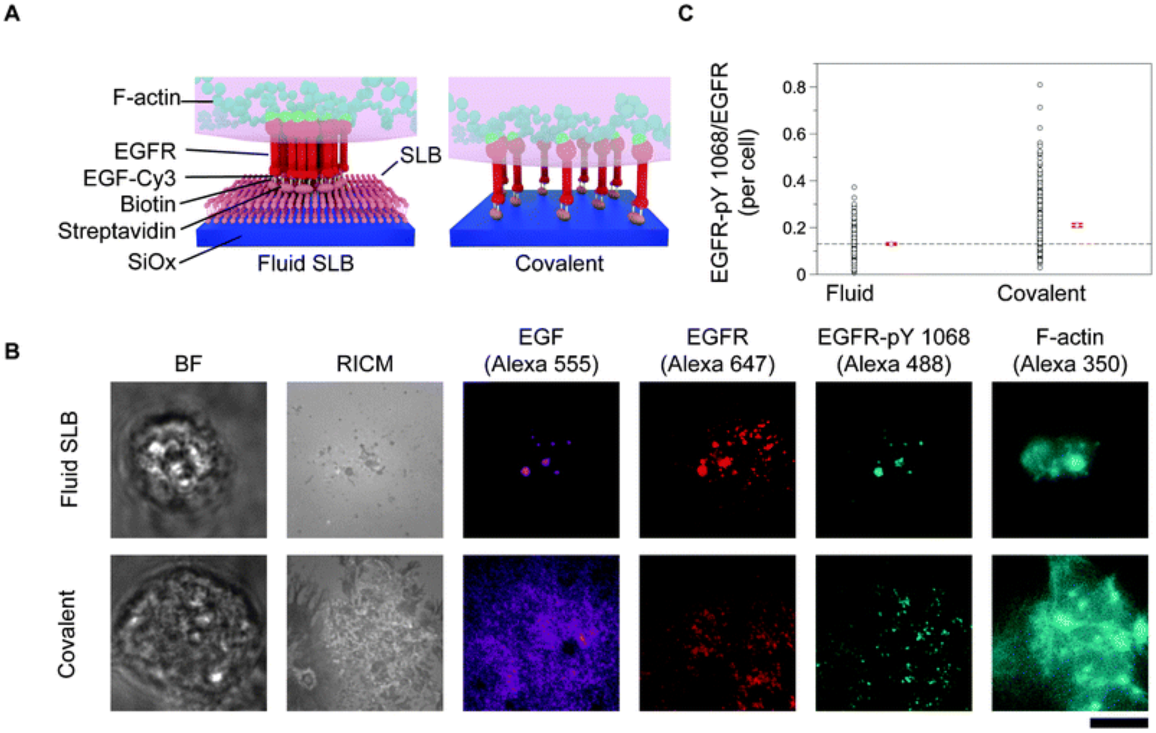

Figure 3.1: EGFR stimulation using mobile and immobile surface-tethered ligands. (A) Schematic illustration of the EGF-functionalized surfaces employed in this study. Supported lipid bilayer surfaces were formed by exposing lipid vesicles to etched glass surfaces, while the covalent substrates were fabricated using silane coupling as described in the Methods section. In both of these surfaces, a biotinylated EGF ligand was anchored to streptavidin-functionalized substrates. (B) HCC1143 cells were plated onto the EGF-functionalized surfaces and incubated for 1 h at 37 °C, 5% CO_2. After fixing and staining, cells were imaged, revealing the formation of large ligand (EGF, Alexa-555) clusters on the fluid surfaces that colocalized with EGFR-pY 1068 (Alexa 488), EGFR (Alexa 647), and F-actin (Alexa 350). Cells plated on covalently functionalized substrates displayed activated (phosphorylated) EGFR, however cell-induced clustering of the ligand was not observed. Scale bar is 10 µm. (C) Plot showing the EGFR-pY 1068/EGFR ratio for each type of surface. The red dot and error bars represent the mean and standard error of the ratio for individual cells, respectively. $n = 257$ and 332 cells for the fluid and covalent surfaces, respectively.

cells. To initially explore this question, we tethered the EGF ligand onto two different types of surfaces (Fig. 3.1A). The EGF ligand was anchored either to a laterally mobile fluid supported lipid bilayer, or to a covalently functionalized glass slide that prevents lateral diffusion of ligand (Fig. 3.1A). The motivation for using these surfaces was to contrast the activation levels of ligand-bound receptors that self-assemble into molecular clusters compared to receptor complexes that are spatially constrained.

Fluid supported lipid bilayers were formed on the surface of clean glass slides by exposing the surface to 1,2-dioleoyl-*sn*-glycero-3-phosphocholine (DOPC) vesicles that spontaneously rupture and fuse onto the glass in the presence of aqueous buffer.[2,16,20,30] The supported lipid bilayers were doped with biotin-functionalized lipids (0.01%- 0.1%) to tether the EGF through biotin-streptavidin conjugation. The lipid membrane and surface-anchored EGF were laterally fluid as confirmed by fluorescence recovery after photobleaching experiments (Fig. 3.2). The surface density of EGF was found to be 280 ± 20 EGF molecules per µm^2 for the membrane surfaces doped with 0.1% biotin-functionalized lipid, and this value was determined by using quantitative

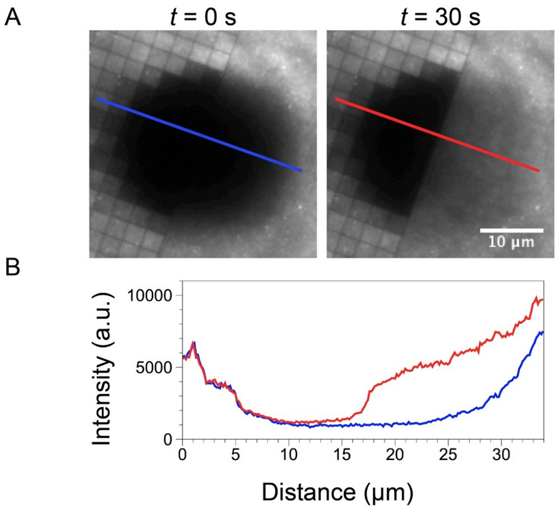

Figure 3.2: Nanopatterns act as barriers to limit tethered-EGF diffusion.
(A) A fluorescence recovery after photobleaching (FRAP) experiment was performed in the TIRF 647 channel at the edge of a 3 mm grid patterned region of an EGF-Alexa 647 functionalized supported lipid bilayer (see methods for details on the preparation of supported lipid bilayers). Outside of the patterned regions, fluorescence recover is apparent due to the free diffusion of the tethered EGF-Alexa 647 conjugates. However, fluorescence recovery was abolished in the patterned region as the EGF-Alexa 647 conjugates were unable to diffuse. (B) Line scan intensity profiles of FRAP experiment indicate that recovery was primarily observed outside of the patterned region, thus showing that long-range diffusion of the EGF ligand is confined by diffusion corrals.

fluorescence imaging using TRITC-DHPE doped supported lipid bilayers as a reference (see methods for details).[31] The density of tethered EGF on the 0.1% biotin-doped fluid membrane matches the density of receptor expressed on the surface of breast cancer cell lines, such as BT474 (~900 EGFR molecules/μm^2 assuming a 15 μm diameter cell), that overexpress EGFR, within one order of magnitude.[32]

In order to immobilize the EGF ligand onto a surface and to prevent its lateral mobility, we directly anchored the EGF ligand to glass surfaces covalently functionalized with biotin and bound to streptavidin (Fig. 3.1A). Substrates covalently functionalized with biotin groups were prepared by etching glass coverslips in piranha (3:1 H_2SO_4 (glacial):H_2O_2 (30%)) and then functionalizing with aminopropyltriethoxy silane. The terminal amine of the silane was then coupled to an N-hydroxysuccinimidyl ester-biotin linker and subsequently incubated with streptavidin. These surfaces presented the EGF ligand at a density of 250 ± 20 molecules/μm^2 and this density matched the density of a 0.075% biotin-doped lipid bilayer (230 ± 20 EGF molecules/ μm^2). Therefore, these two types of surfaces were used to stimulate cells since they display similar EGF surface densities and use the same conjugation chemistry, but the difference is that the ligand is not capable of lateral movement with the covalently modified glass slides.

3.3 The Formation of Clusters Affects Signaling

In a typical experiment, human breast cancer cells that overexpress the EGFR (HCC1143) were plated onto each surface and allowed to incubate for 1 h at 5% CO_2, 37˚C. Cells were then fixed and stained via immunohistochemistry for the EGFR, phosphorylated tyrosine residue 1068 of the intracellular domain of EGFR (EGFR pY 1068), and also stained for F-actin using phalloidin-Alexa 350. We found that cells engaged the EGF-functionalized fluid supported lipid bilayer surface and formed large-scale assemblies of receptor that were colocalized with EGF, EGFR-pY 1068 and F-actin (Fig. 1B). In contrast, cells that were plated on the non-mobile EGF ligand substrates were strongly adhered to the surface through EGF-EGFR binding interactions, but did not translocate ligand-receptor complexes (Fig. 3.1B). Nonetheless, ligand-bound receptors, as indicated by the EGF and EGFR immunostains, were highly phosphorylated and colocalized with F-actin in both cases (Fig. 3.1B). Note that although the fluorescence immunostaining images of EGFR on the fluid and non-fluid surfaces suggests the formation of dense receptor aggregates, only the fluid membrane surfaces allow for lateral translocation and molecular assembly of ligand-receptor complexes. Note that the lack of complete colocalization between the covalently tethered EGF and receptor is due to incomplete ligand-receptor binding. In contrast, the fluid EGF is free to diffuse and concentrate at the locations of EGFR cluster assemblies (Fig 3.1B).

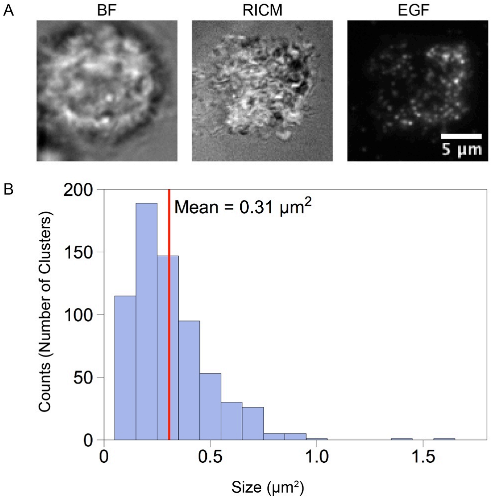

Figure 3.3: Soluble EGF stimulation leads to EGFR clustering.
(A) HCC1143 cells were incubated for 1h on supported lipid membrane surfaces functionalized with cRGD peptide at 37º C, 5% CO_2. Cells were then treated with soluble EGF-Alexa 647 (1.65 nM) for 5 min and fixed. Cells exhibited clusters of EGFR, though they were generally smaller than those observed with tethered ligand. (B) Histograms of cluster size for cells in (A). Fluorescent images of EGF-647 were background subtracted and then run through an enhancement filter (Spot Tracker 2D Spot Enhancing Filter for ImageJ) and then subjected to binary thresholding and a watershed algorithm. Finally, particles were automatically analyzed in ImageJ (native function). *n* = 668 clusters over 5 cells.

To compare EGFR clustering induced by membrane-tethered ligand to that induced by soluble EGF, HCC1143 cells were incubated on cyclic Arg-Gly-Asp-Phe-Lys (cRGDfK, an integrin-binding peptide that facilitates cell adhesion) functionalized supported membranes for 1h and then treated with 1.65 nM EGF-Alexa 647 for 5 min. Soluble ligand-stimulation generated clusters of EGFR on the surface of HCC1143 cells, in agreement with literature precedent.[10,29] We found that the mean diameter of soluble EGF-induced clusters was generally smaller than that observed during stimulation with fluid membrane-tethered EGF. While this experiment does show that clusters form when EGFR-expressing cells are treated with soluble EGF, any further comparison is not possible due to the inherent differences between tethered and soluble ligand.[33,34] (Fig. 3.3).

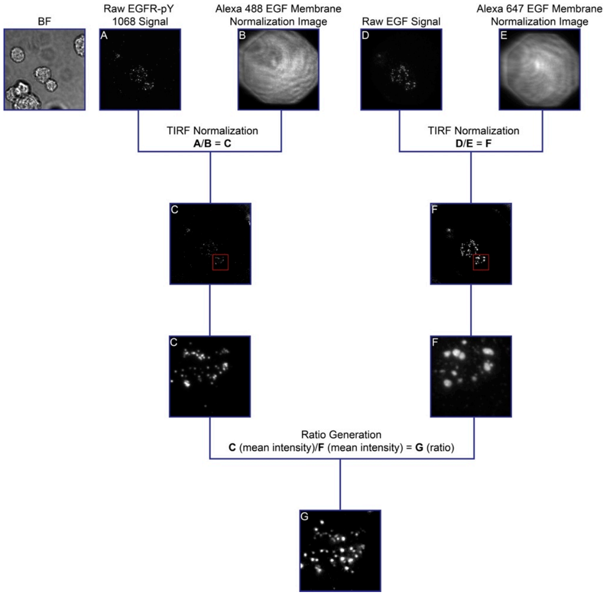

Figure 3.4: Schematic illustrating the image processing routine used for ratio measurement. After obtaining fluorescence data from cell experiments, images must be properly normalized and measured in order to yield ratio measurements of the EGFR-pY and EGF signals. First, raw fluorescence images of each channel were background subtracted. Then each image was normalized for difference in laser excitation intensity using control fluid membranes functionalized with the dye of interest. Once the images were normalized in this manner, the mean fluorescence intensity under each individual cell was measured by placing an identical ROI over the cell of interest *(note that no thresholding was used – only the raw mean fluorescence values were measured)*. Finally, the mean intensity from each channel was divided to yield the EGFR-pY 1068/EGF ratio.

To compare receptor activation levels across the immobilized and laterally fluid EGF surfaces, we normalized the EGFR-pY 1068 level by the EGFR signal intensity in order to determine the ratio of activated receptor to total receptor within individual cells plated on each surface type. We did not use the EGF intensity under each cell due to the fact that not all ligand was bound to receptor on the non-mobile surfaces. Image analysis indicated differences between the average EGFR-pY 1068/EGFR ratio for cells on each type of substrate (Fig. 3.4). The covalent surfaces displayed a 62% (0.21 ± 0.007) larger

EGFR-pY 1068/EGFR ratio, respectively, compared to the fluid supported lipid bilayer surface ratio (0.13 ± 0.004). This suggests that the assembly of ligand-receptor complexes within clusters on the fluid membrane surfaces dampens receptor activation at this experimental time point (t = 60 min) (Fig. 3.1C).

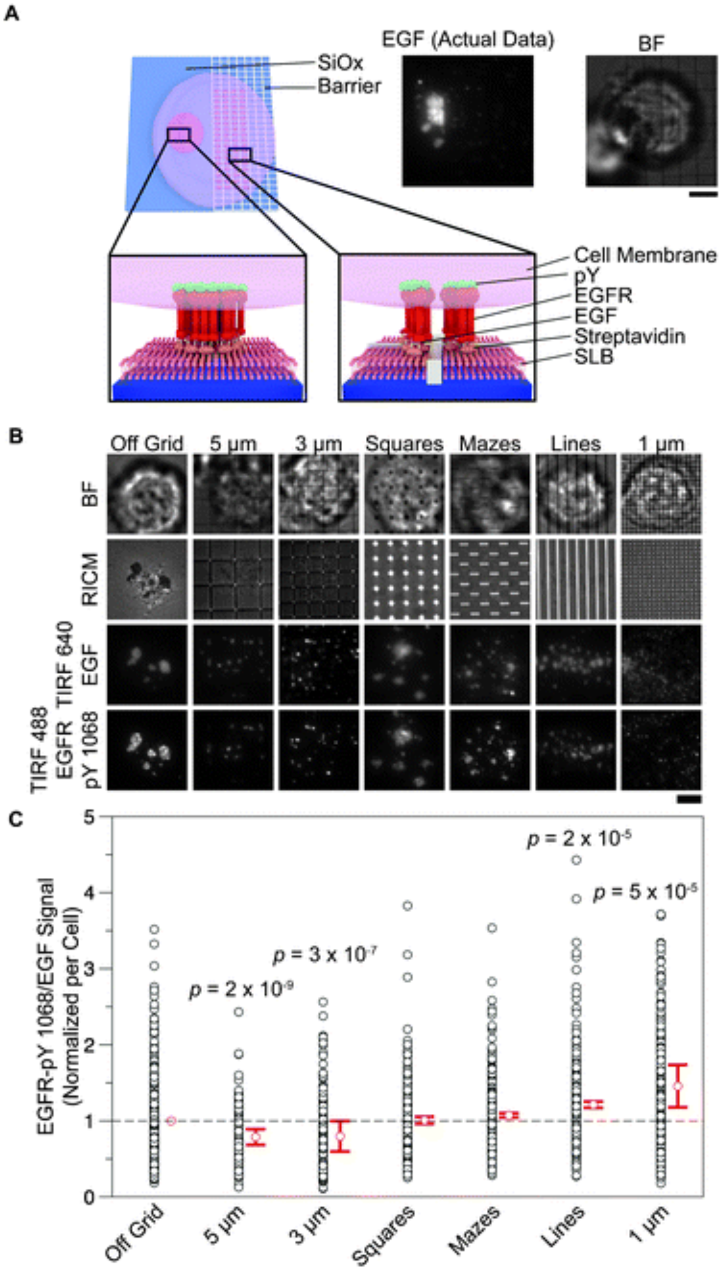

Figure 3.5 Lipid diffusion barriers limit EGFR clustering and allow quantification of the relationship between cluster size and activation level. (A) Scheme illustrating a cell engaged with a patterned and non-patterned region of a supported lipid membrane. Fluorescence image of the EGF organization under a cell on the border of a 3 µm nanopatterned grid functionalized supported lipid bilayer. Scale bar is 5 µm. (B) Representative images of cells in the BF, RICM, TIRF 640 (EGF), and TIRF 488 (EGFR-pY 1068) channels interacting with nanopatterns (or non-patterned areas) on a supported lipid bilayer functionalized with EGF. Barriers directly controlled cluster size and pattern according to their respective dimensions and shapes. Image contrast levels have been adjusted to highlight cluster size for each representative image. Scale bar is 5 µm. (C) Vertical scatter plot showing the relationship between feature size and EGFR-pY 1068/EGF ratio. Ratios were taken from the mean intensities of the TIRF 488 (EGFR-pY 1068) and TIRF 647 (EGF) channels. Each dot represents the ratio of an individual cell. The data points are pooled from 4 independent experiments. The p values listed for the 5 µm, 3 µm, 1 µm, and line control features correspond to a Student's t-test between the given feature and the off-grid control. n = 401, 206, 210, 418, 245, 221, and 243 cells for the off-grid, 5 µm, 3 µm, 1 µm, square control, maze control, and 2 µm lines, respectively.

3.4 Cluster Size Modulates Receptor Phosphorylation

To quantify how clustering influences receptor activation, we manipulated receptor cluster size by patterning metal lines into the supported lipid bilayer. In this approach, nanopatterned chromium lines are fabricated on a glass slide and act as physical diffusion barriers to confine lipid diffusion within discrete corrals (schematic: Fig. 3.5A, Fig. 3.6).[24] The diffusion barriers were fabricated using e-beam lithography (see methods for fabrication details). The typical width of each line was ~100 nm, and the height was commiserate with that of a streptavidin conjugated lipid bilayer (~ 10 nm) (Fig. 3.6 A-B). The patterned diffusion barriers only affect cells through the specific ligand-receptor interaction rather than surface topography, thus diffusion constraints are exerted only on ligand-bound EGF receptors.

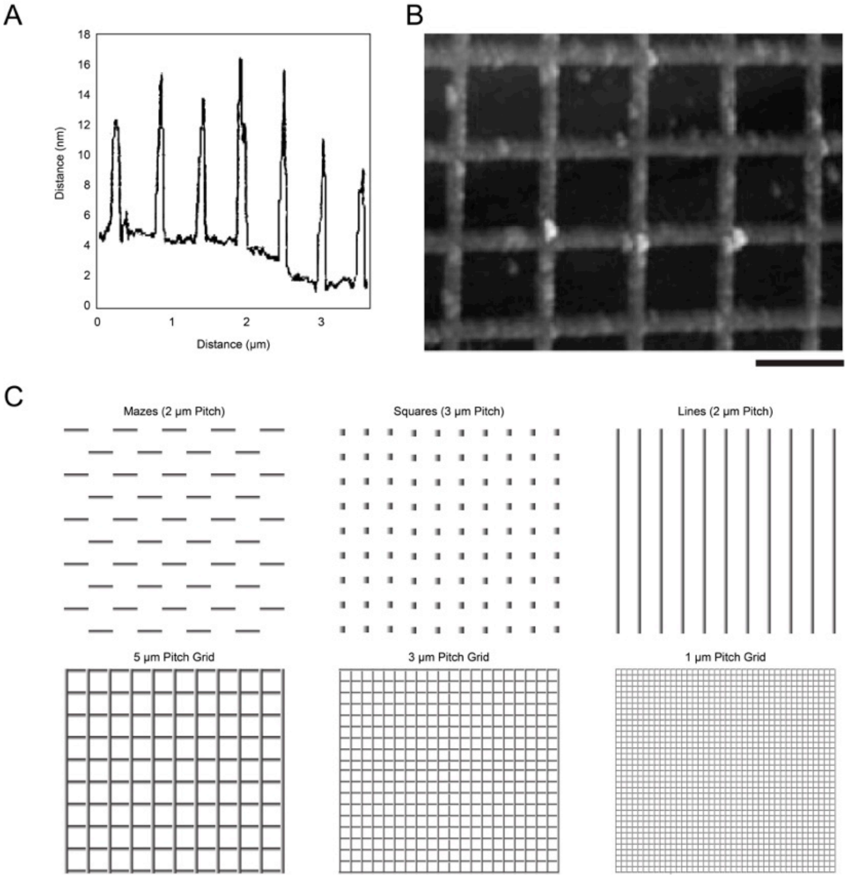

Figure 3.6: Dimensions of nanopatterned features.
(A) AFM line scan taken from of a representative AFM image (B) that was collected over a region of a nanopatterned grid surface with a 500 nm pitch. The line width is 110 ± 10 nm, and the line height is 10 ± 2 nm. Scale bar is 500 nm. (C) Representative schemes of the six different features used to manipulate ligand-induced EGFR clustering in live cells.

This technique allows the direct manipulation of EGFR receptor clustering while also permitting quantification of receptor activation in living cells. Metal patterning of surfaces with supported lipid bilayers has previously been used to elucidate the role of spatial organization in T-cell receptor activation, [2,24] EphA2 receptor activation,[1,25] and has also been used to track single protein diffusion in a position dependent manner via a nano-antenna patterning approach.[35]

In these experiments, each substrate had an array of six types of nanopatterns: 5 µm, 3 µm, and 1 µm pitch grids, 3 µm pitch squares, 2 µm pitch mazes, and 2 µm pitch lines (Fig. 3.6 C). The total size of each patterned area within the array was 400 by 400 µm^2. The grid nanopatterns were designed to allow for molecular reorganization and assembly, while preventing large-scale clustering across the chromium barriers. The square and maze features were included as additional controls for potential artifacts due to chromium metal. For all nanopatterned

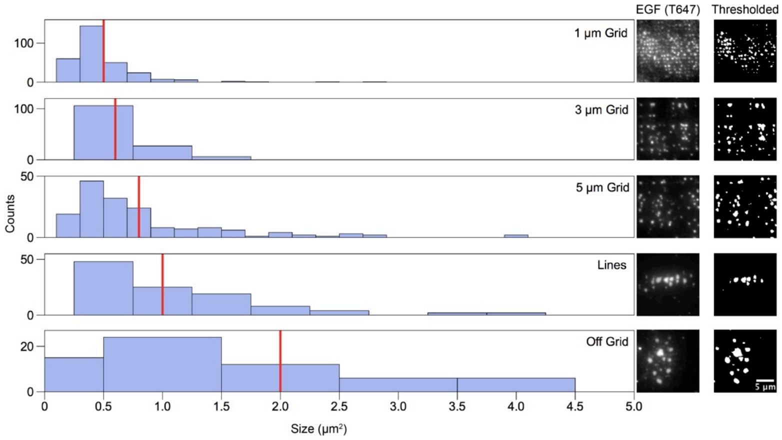

Figure 3.7: Histograms comparing EGF cluster size as a function of pattern type.
To estimate EGF cluster size, the raw fluorescence images collected from each nanopattern experiment were subjected to the same manual thresholding routine, resulting in a binary image delineating cluster size and location. These binary images were then automatically filtered with a watershed algorithm to reduce the number of adjacent clusters counted together during analysis. Analysis of the binary images was performed in imageJ with the standard plugin set using a 0.35 µm^2 filter to prevent counting of diffraction limited spots. Clusters for each pattern type shown were then binned according to area (red lines represent mean areas, 2, 1, 0.8, 0.6, and 0.5 µm^2 for the off grid, lines, 5 µm, 3 µm, and 1 µm grids, respectively). The size of the diffusion pattern directly dictated the mean cluster area in each cell. *n* = 5 cells for the 5, 3, and 1 µm nanopatterns and 7 and 6 cells for the off grid and line patterns, respectively.

experiments, supported lipid bilayers were formed on chromium barrier surfaces and functionalized with Alexa 647-EGF as described above.

HCC1143 cells were seeded onto nanopatterned EGF- Alexa 647 supported lipid bilayer surfaces and incubated for 1 h at 5% CO_2, 37˚C. Cells were subsequently fixed and permeabilized and then immunostained for EGFR-pY 1068. The cells that were engaged to each of the six different types of nanopatterns, along with the non-patterned regions, were imaged and analyzed. Representative images and live cell imaging showed that the patterns restricted EGF-EGFR clustering (Fig. 3.5B), and altered the average cluster size. To quantify the average cluster size for cells that engaged each type of pattern, we applied a threshold to each EGFR image and used an automated script to detect particles and generate histograms of their sizes. The 1 µm, 3 µm, 5 µm pitch grid, and line patterns restricted the average cluster area to ~0.5 µm^2**,** ~0.6 µm^2, ~0.8 µm^2, and ~1 µm^2, respectively (Fig. 3.5B, Fig. 3.7).

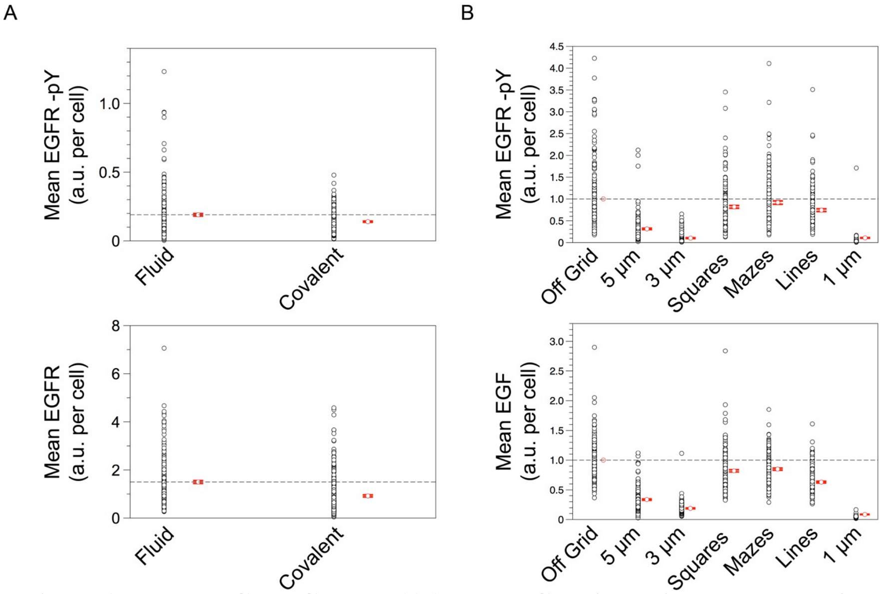

Figure 3.8: Raw EGF, EGFR-pY1068, and EGFR intensity values used for ratio analysis in Figures 1 and 2.
(A) Vertical scatter plots showing the mean cell values of the EGFR-pY and EGFR signal as taken during the experiments shown in figure 1. (B) Vertical scatter plots of the mean EGFR-pY and EGF values taken under each cell during the nanopatterned supported lipid bilayer experiments shown in figure 2

In order to determine if cluster size influenced activation levels, the normalized EGFR-pY-1068/EGF fluorescence ratio was measured for individual cells on each type of pattern, as well as cells outside of the patterned region (Fig. 3.5C). This measurement was performed without any thresholding of the raw fluorescence intensities, assuring that the ratio was a faithful measure of the amount of receptor activated per ligand on the surface. This experiment was repeated four times, and each run was combined into a single data set (see methods and Fig. 3.4 for analysis details, and Fig. 3.8 for raw EGF and pY values). The mean EGFR-pY 1068/EGF value decreases slightly (~10%) when cells engaged the 5 μm or 3 μm grid in comparison to the non-patterned region. However, cells engaged to 1 μm grid patterns exhibited a significant (46%) increase in EGFR-pY1068/EGF ratio. The control patterns that allow free diffusion of the lipids (mazes and squares) showed minimal deviation from the off-pattern cell mean, while the line pattern showed a ~20% increase in ratio. This result suggests that large scale clustering (> 1 μm grid pattern) dampens receptor activation levels (Fig. 3.4C). In order to further assess the validity of these results, population statistics were performed on each pattern subtype. The *p* value (according to Student's t test) between the off grid control and the 1 μm grid was 5×10^{-5}, indicating that the increase in ratio due to limiting the cluster size of the EGFR receptor is significant (Fig. 3.4C).

The smallest pitch nanopatterns (1 μm spaced grid array) were found to reduce the effective EGF ligand density by ~50% due to blocking access to the glass surface, and thus reducing the lipid membrane total area. To verify that the observed increase in EGFR-pY 1068/EGF ratio was not due to reduced EGF surface density, we measured the ratio across a series of substrates that presented decreasing concentrations of EGF (less than ~280 ligand molecules/mm^2). Supported lipid bilayer surfaces with reduced amounts of EGF ligand were generated by doping the 1,2-dioleoyl-*sn*-glycero-3-phosphocholine (DOPC) lipid vesicles with decreasing concentrations of biotinylated lipid (0.1%, 0.075%, and 0.045%) through mixing with DOPC/Biotin-DPPE vesicles (99.9%, .1%),

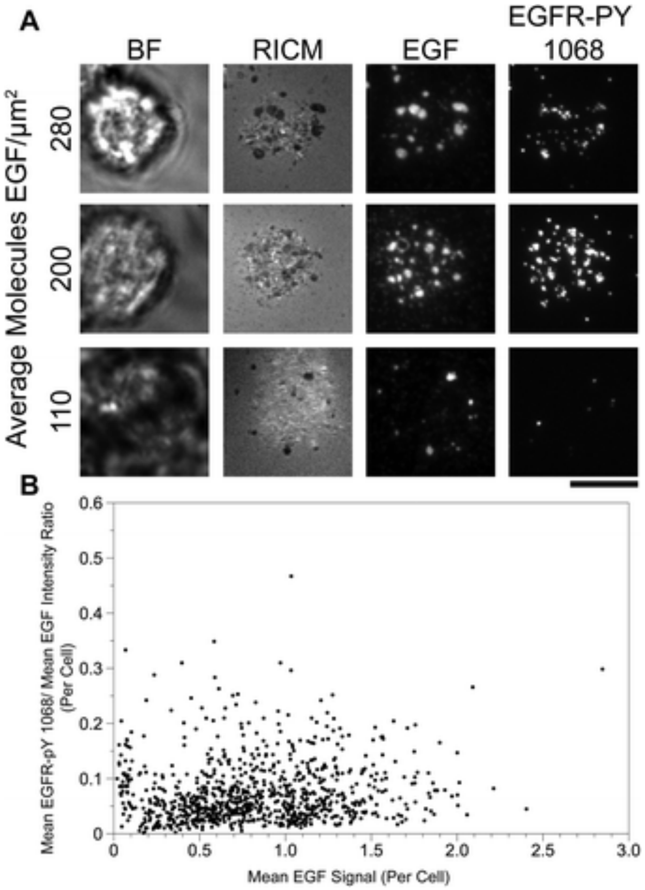

Figure 3.9: Ligand concentration does not alter the EGFR-pY 1068/EGF ratio within experimentally relevant EGF densities.
(A) Representative images of cells plated on EGF functionalized supported lipid bilayers featuring EGF densities that were 40% (110 ± 20 molecules per μm^2) and 70% (200 ± 20 molecules per μm^2) of the EGF density on the 0.1% biotin membrane (280 ± 20 molecules per μm^2). EGF intensity values are averages of the mean EGF signal intensities per cell for each population of cells. Scale bar is 10 µm. (B) Scatter plot of the EGFR-pY 1068/EGF ratio *versus* mean EGF intensity for approximately 1700 cells on the surfaces described in (A).

resulting in substrates of varying EGF densities. Importantly, the lipid membranes doped with 0.035% and 0.075% biotin presented EGF densities that were ~63% and ~26% smaller than the EGF density of the control surface, respectively. These densities were chosen because they better matched the range of EGF densities observed in the nanopattern experiments. When we measured the EGFR-pY 1068/EGF ratio for these cells, we observed no correlation between EGF concentration for each cell and EGFR-pY 1068/EGF ratio (Fig. 3.9). Therefore, the observed increase in phosphorylation per

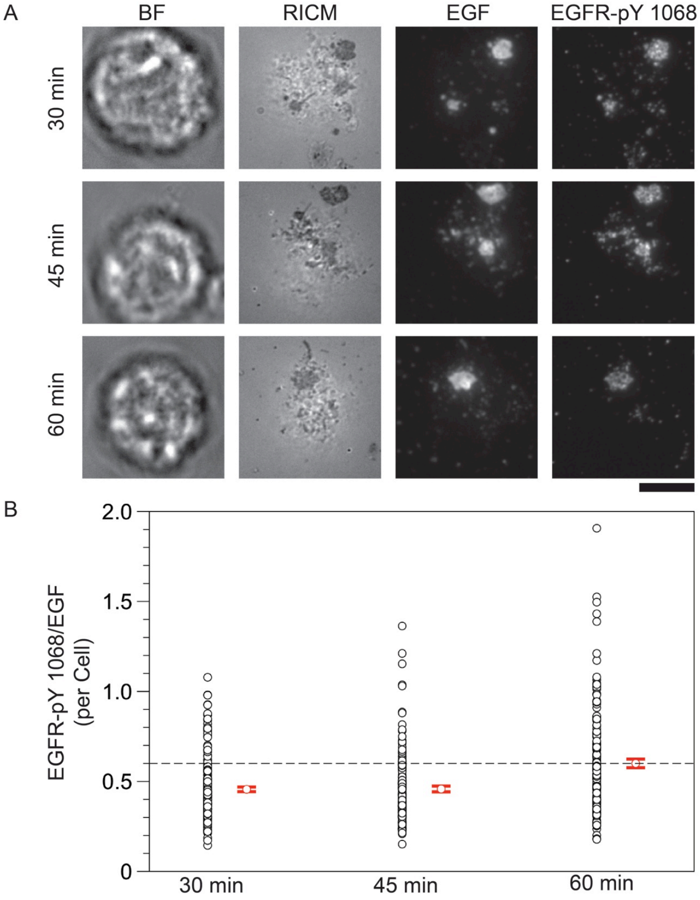

Figure 3.10: Incubation time does not significantly affect the EGFR-pY 1068/EGF ratio. (A) Representative images of HCC1143 cells that were plated onto EGF functionalized SLBs and allowed to incubate for 30, 45, and 60 minutes before fixation. The samples were then stained for EGFR-pY 1068 and imaged in the BF, RICM, EGF, and EGFR-pY 1068 channels (scale bar is 10 µm). (B) Quantification of the EGF to EGFR-pY 1068 ratio for n = 478 cells revealed that there is no significant difference between the 30 and 45 min time points, and that there is a slight increase at the 60 min time point.

receptor on the nanopatterned substrates (1 µm grid, Fig. 3.4C) is not due to reduced EGF concentration. We also performed controls to determine if the experimental time point had an effect on the EGFR-pY 1068/EGF ratio. HCC1143 cells were plated onto fluorescent EGF functionalized supported lipid bilayers and fixed after 30, 45, and 60 min incubation times. The samples were then stained for EGFR-pY 1068 and imaged. Ratio analysis did not find a significant difference in EGFR-pY 1068 to EGF ratio between the tested time points (Fig. 3.10). This is in agreement with literature precedent measuring the time dependence of receptor activation by surface tethered EGF ligand.[33]

3.5 Investigating the Mechanisms of EGFR Cluster Formation

Having shown that EGFR clustering impacts its phosphorylation level we next wanted to investigate the mechanism of EGFR assembly into larger clusters. Live cell time-lapse TIRF microscopy imaging indicated that there were two stages of EGFR clustering. The initial stage consisted of spontaneous formation of small sub-micron

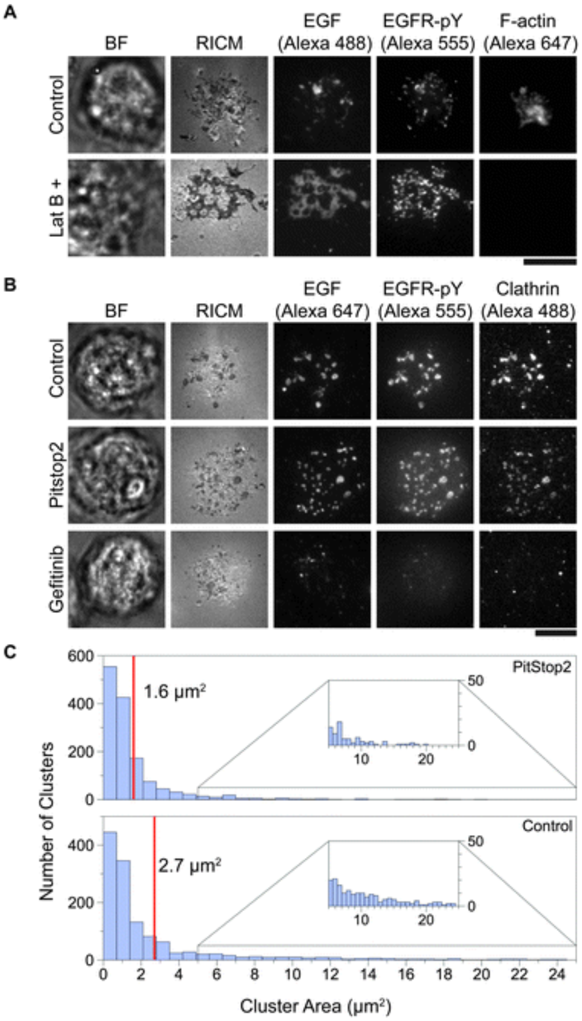

Figure. 3.11 Inhibition of F-actin, EGFR kinase activity, and clathrin terminal domain associations alters EGFR clustering. (A) HCC1143 cells were serum starved overnight and treated with either Lat B (25 µM) or vehicle DMSO for 20 min. Cells were then plated on supported lipid bilayers functionalized with EGF-Alexa 488 and incubated for 1 h at 37 °C, 5% CO_2. After incubation, cells were stained for EGFR-pY 1068 and F-actin. Lat B treatment resulted in the near complete abrogation of F-actin and the formation of large EGFR clusters as compared to the control. Scale bar is 10 µm. (B) Cells were treated with either Gefitinib (10 µM, 20 min), PitStop2 (30 µM, 20 min), or vehicle DMSO and then incubated on supported lipid bilayers functionalized with EGF for 1 h at 37 °C, 5% CO_2 after which they were fixed and permeabilized (see Methods for details). The cells were then stained for clathrin and EGFR-pY 1068. Control cells exhibited typical clusters. Cells treated with PitStop2 showed decreased cluster size, while clustering was abolished in cells affected by Gefitinib. Additionally, clusters colocalized with clathrin-eGFP. Scale bar is 10 µm. (C) Histogram comparing cluster sizes in control and PitStop2 samples. PitStop2 decreased the cluster size by 1.1 μm^2 on average as compared to control. *n* = 204 control cells and 138 PitStop2 treated cells.

receptor clusters that formed across the cell-supported membrane contact area. After approximately 15 min, clusters coalesced into larger (sub-micron to micron sized) clusters that generally translocated to the center of the cell-supported membrane junction. The directed transport of EGFR assemblies suggested that the cytoskeleton was involved in receptor translocation. Clustering of other receptors has been shown to depend on actin polymerization,[36] and EGF-EGFR complexes are subject to retrograde flow of actin.[37,38] In light of this, we tested the role of F-actin EGFR clustering. HCC1143 cells were pre-treated with 25 μM Latrunculin B (a drug that prevents actin polymerization by binding actin monomers, LatB) for 20 min or DMSO control and incubated on EGF-functionalized supported lipid bilayers for ~30 min. The cells were then fixed and stained for F-actin to confirm the effect of the drug at these concentrations. Surprisingly, cells treated with LatB exhibited large irregular EGFR clusters that typically covered the entire cell-supported membrane contact area (Fig. 3.11A). In contrast, control cells treated with DMSO exhibited typical clusters that were considerably smaller as previously shown (Fig. 3.1B, 3.4B, Fig. 3.11A). This suggests that F-actin association with EGFR oligomers initially prevents coalescence into

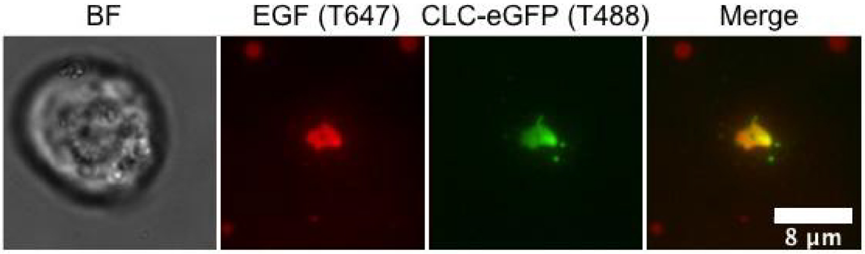

Figure 3.12: EGF clusters colocalize with clathrin light chain-associated structures.
HCC1143 cells were transfected with a construct encoding clathrin light chain-enhanced green fluorescent protein (CLC-eGFP). After ~24 h of transfection, cells were incubated on an EGF-functionalized supported lipid bilayer for 1 h, and imaged using TIRF in the 488 and 647 nm channels. Representative brightfield, TIRF 647 (EGF), TIRF 488 (CLC-eGFP), and an overlay of the two TIRF channels is shown. The data indicates the formation of the characteristic EGF clusters, which were highly colocalized with clathrin assemblies.

large clusters.

To further probe the dynamics of this F-actin association, HCC1143 cells were transfected with an actin-eGFP plasmid and plated on EGF functionalized supported lipid bilayers. Dual-channel time-lapse TIRF microscopy of these samples revealed F-actin and EGF co-movement. This suggests coupling between F-actin and EGFR, which has been reported previously using single particle tracking and agrees with the initial phalloidin stain results.[37]

The surface concentration of EGFR is primarily regulated by clathrin-mediated endocytosis and recycling, a process by which the cell exerts a force on the receptor during internalization.[16,39] To investigate the role of this process in EGFR clustering and translocation, cells were transfected with a clathrin light chain-eGFP construct and incubated on EGF-functionalized supported lipid bilayers (see methods for experimental details). Live cell TIRF imaging of EGF and CLC-eGFP revealed assemblies that colocalized, suggesting a role for clathrin in clustering (Fig. 3.12). Clathrin binds to a host of adapter proteins through its terminal domain motif, or TD, and these proteins play a vital role in regulating the process of endocytosis.[40] In light of this, we used PitStop2, a small molecule which inhibits clathrin TD associations (but does not prevent clathrin assembly), to interrogate whether clathrin terminal domain associated proteins contribute to EGFR clustering.[41] When cells were treated with PitStop2, EGFR-EGF clusters were still observed, however, the average cluster size was reduced to ~1.6 μm^2 (as compared to ~2.7 μm^2 for the control) and the clusters were more evenly distributed across the cell membrane (Fig. 3.11B-C). Furthermore, cells in which the EGFR kinase domain was inhibited by Gefitinib showed the formation of small receptor clusters but drastically reduced formation of larger-scale assemblies (Fig. 3.11B). Taken together, these data suggest that receptor activation (but not ligand binding), and clathrin terminal domain-association are critical for the formation of large-scale EGFR clusters.

One possible mechanism to explain the correlation between cluster size and EGFR receptor phosphorylation relates to non-ligand activation of the receptor. For example, it has been observed that kinase-deficient mutants of EGFR can be activated by association with kinase-active receptor,[42] and that inactive, un-liganded EGFR can be activated through lateral interaction with activated EGFR.[12] Taken with the fact that the EGFR has the capability of dynamic self-association and disassociation, it is possible that the observed increase in activity (larger EGFR-pY per ligand) for small clusters is due to a cross-activation effect whereby ligand-bound phosphorylated receptor activates un-liganded receptor at its periphery in a diffusion dependent manner. As small clusters have a higher circumference to area ratio and lower densities, it may suggest that they are capable of activating a larger number of receptors than larger clusters using the same number of ligands.

3.6 Conclusion

Herein we demonstrated that spatial organization of the EGFR modulates receptor activation levels, and conversely we showed that EGFR clustering depends on receptor phosphorylation and interaction with the cytoskeleton as well as involvement of clathrin-mediated internalization. Through the use of nanopatterned diffusion barriers and supported lipid bilayers, EGFR clustering was altered without modifying native proteins.

This approach revealed that EGFR cluster size modulates receptor phosphorylation, as clusters smaller than 1 μm^2 are more efficiently phosphorylated than larger clusters.

These findings may be useful in the area of biomaterials, where surface-tethered growth factors are commonly employed, or for use in drug-delivery strategies that prevent receptor aggregation. It is important to note that while EGF is generally a soluble ligand, it has been shown that tethering EGF does not prevent receptor activation,[33,34,43,44] and supported lipid bilayer surfaces have previously been used for EGF surface display.[15] Importantly, tethering of EGF prevents internalization of the receptor, resulting in sustained activation that differs from the activation spikes seen with soluble EGF.[33] For this reason, surface tethered EGF-polymers have been used to improve the survival of mesenchymal stem cells (MSCs) and promote attachment, opening up the possibility for functionalized polymer scaffolds that could be used to repair tissue damage.[34] Additionally, EGFR has natural juxtacrine ligands such as the EGF homologues heparin-binding EGF-like growth factor and transforming growth factor alpha (TGF-**α**).[45] Thus, differences in the spatial arrangement of juxtacrine ligands may play a role in signal regulation. Moreover, these findings help elucidate how the cytoskeleton and the endocytotic machinery can influence the signaling outputs of membrane tethered growth factors. Therefore, investigating surface-tethered ligand activation of EGFR is broadly relevant despite some limitations in specifically applying the results of this study to the typical soluble ligand stimulation pathway.

Importantly, while these results represent a step towards understanding how receptor clustering affects the EGFR signaling cascade, more thorough investigations are hindered by the difficulty of combining conventional biochemical techniques such as qRT-PCR and Western blotting with nanoscale cell receptor manipulation methods.[46] Future studies will need to overcome these limitations to further probe the effects of EGFR clustering and determine the extent of its regulatory influence over the global EGFR signaling network.

3.7 Methods

Data Processing

Data processing was performed with the imageJ (NIH) software package using the LOCI bioformats plugin for proprietary image handling.

Determination of EGFR-pY 1068/EGF (EGFR) Ratios

In order to generate the EGFR-pY 1068/EGF (EGFR) ratios, we performed a series of operations. First, the raw fluorescence images from each channel were background subtracted. Next, each subtracted image was divided by a normalization image taken at identical settings in order to correct for the TIRF excitation intensity of each channel. Finally, a uniform cell-sized circular region of interest (ROI) was manually placed over regions of cell fluorescence and used to measure the intensity in each channel. *Note that there was no thresholding applied to these images, thus the mean fluorescence under each cell was not altered from the original 16 bit image format.* The ratio of the intensities was used to calculate the given signal ratio and averaged for many cells on each type of surface.

Cell Fixation Procedure

After incubating cells on the specific surface, the wells were rinsed with 5 mL of 4° C 1X sterile PBS to remove media from the sample. Next, each sample was rinsed with 5 mL of 4º C 4% paraformaldehyde (Sigma) in 1X PBS and incubated for 12 min at RT. After incubation, the sample was again rinsed with 5 mL of 1X PBS, and then permeabilized with 5 mL 0.1% Triton-X (Sigma) in 1X PBS (vol/vol %) and incubated for 5 min at RT. Finally, cells were washed with a 5 mL aliquot of 1X PBS and 5 mL 1% BSA (fraction V, heat shock isolation, Calbiochem) in 1X PBS. Cells were then blocked overnight at 4º C.

Antibody Staining

The anti-EGFR-pY-1068 primary rabbit IgG antibody (Cell Signaling Technologies, #3777S) was diluted at a 1:800 volume:volume ratio in 1% BSA (1X PBS) and added to each sample and incubated for 1h at RT. In experiments where the EGFR was also stained the anti-EGFR rat IgG primary antibody (Santa Cruz #71035) was incubated at the same dilution concurrently. Each sample was then rinsed with 5 mL of 1% BSA in 1X PBS. Next, a 1:1000 dilution of anti-rabbit Alexa 488 (Invitrogen) and anti-rat Alexa 647 (when the EGFR primary was used, Invitrogen) were added to each sample and incubated for 30 min. The samples were then rinsed once more with 5 mL of 1% BSA in 1X PBS and then imaged. In experiments where clathrin was imaged, samples were stained with 1:800 Covance antibody # MMS-423P (clathrin light chain, mouse IgG) and an appropriate anti-mouse secondary following the same procedure as described above.

Cell Culture

All cell lines were maintained at 37˚ C and 5% CO_2. HCC1143 cells were cultured in RPMI-1640 media with the addition of 10% fetal bovine serum (FBS, Mediatech), 100 IU ml^{-1} penicillin G (Mediatech), 100 μg ml^{-1} streptomycin (Mediatech) and 2.5 mM L-Glutamine (Mediatech) following the ATCC formulation guidelines.

Cell Transfection

HCC1143 cells were seeded on a 24 well plate in antibiotic-free media at a density of ~30,000 cells per well overnight at 37˚ C, 5% CO_2. The cells were then transfected with the construct (either CLC-eGFP or F-actin-eGFP) using Lipofectamine 2000 (Invitrogen) following standard transfection protocols. These cells were then serum starved overnight and used for experiments as indicated within 24 h of the transfection.

Fluorescence Microscopy

Live cells were imaged in serum free RPMI 1640 (Mediatech) media formulated as described in the cell culture section at 37 °C, and fixed cells were imaged in 1% BSA in 1X PBS at RT. During live-cell imaging, physiological temperatures were maintained with a warming apparatus consisting of a sample warmer and an objective warmer (Warner Instruments part numbers 641674D and 640375). The microscope used was an Eclipse *Ti* driven by the Nikon Elements software package (Nikon). The microscope features an Evolve EM CCD (Photometrics), an Intensilight epifluorescence source (Nikon), a CFI Apo 100x (NA = 1.49) objective (Nikon), and a TIRF launcher with two laser lines: 488 nm (10 mW) and 640 nm (20 mW). This microscope also includes the Nikon Perfect Focus System, an interferometry-based focus lock that allowed the capture of multipoint and time-lapse images without loss of focus. The microscope is equipped with the following Chroma filter cubes: TIRF 488, TIRF 640, Cy5, TRITC, FITC, DAPI and RICM.

Preparation of Small Unilamellar Lipid Vesicles

After being mixed in the correct proportions in chloroform, lipids (Avanti Polar Lipids) were dried with a rotary evaporator and placed under a stream of N_2 to ensure complete evaporation of the solvent. These lipid samples were then resuspended in Nanopure (~18.2 mΩ) and subjected to three freeze/thaw cycles by alternating immersions in an acetone and dry ice bath and a warm water bath (45 °C). To obtain small unilamellar vesicles (SUV's), lipids were forced through a high-pressure extruder with a 100 nm nanopore membrane (Whatman).

Supported Lipid Bilayer Preparation

Supported lipid bilayer surfaces were prepared via the vesicle fusion method as previously described in the literature.[16,30] Preparation varied depending on the nature of the vessel used:

A. Glass-Bottomed 96 Well Plate

Wells were rinsed with 5 mL H_2O (18.2 mΩ) and then incubated for 1-2 hours in 1 M NaOH, which was followed by a 5 mL wash with H_2O. All water was then removed from wells and 100 µL of a 1:3 mixture of the desired lipid vesicles and 1X sterile PBS was added to each well and incubated for 5 min at RT. Each well was then rinsed with 5 mL of H_2O and 5 mL of 1X PBS. The wells were then blocked for 30 min at RT with 40 µL of 1 mg/mL BSA (fraction V, cold alcohol isolation, EMD Chemicals), rinsed with 10 mL 1X PBS, and functionalized as described according to the individual experiment. When performing experiments with covalently functionalized glass substrates, it was necessary to adjust the ligand density of the fluid surfaces to the same level. In order to accomplish this, the biotin lipid doping level in the fluid supported lipid bilayers was adjusted by mixing DOPC vesicles with the DOPC/DPPE-Biotin vesicles in a molar ratio of 99.925% to 0.075%. This ratio generated a surface EGF density of 230 ± 20 molecules/μm^2, which closely matches the density of the covalently functionalized glass surfaces.

B. Attofluor Cell Chamber

No 2. Microscope cover glasses (35 mm, VWR) were sonicated in water for 10 min and then etched for 10 min in piranha (a 3:1 mixture of sulfuric acid and 30% hydrogen peroxide, respectively. Please use caution as piranha is extremely corrosive and may explode if it comes into contact with organics). After etching, cover glasses were rinsed well with H_2O and smacked onto a 30 µL droplet of 1:1 lipid vesicle:1X PBS mixture. Cover glasses were then removed from the droplet in a bath of water, and assembled into the attofluor cell chambers (Invitrogen). Chambers were then rinsed with 50 mL H_2O and 50 mL 1X sterile PBS. All samples were then blocked with 100 µL of 1 mg/mL BSA for 30 min at room temperature, then rinsed again with 50 mL 1X PBS and functionalized according to the experiment performed.

Supported Lipid Bilayer Density Calibration

The EGF density on the fluid supported lipid bilayers was measured using quantitative fluorescence microscopy as described in the literature.[31] Briefly, a fluorescence standard curve was determined using fluid supported lipid bilayers (in a 96 well plate) containing various concentrations of TRITC-DHPE lipids. Next, the fluorescence ratio (F factor) between TRITC (the standard dye) and Alexa 555 (the ligand label) was determined by comparing the fluorescence of a range of concentrations of either unilamellar lipid vesicles or Alea 555-EGF-biotin in 1X PBS (fluorescence intensity was determined using the 100X objective focused ~100 µm above the well surface). The F factor was found to be 0.62 ± 0.16. After obtaining the standard curve and the F factor, any image of Cy3-EGF acquired with the same settings as the standard curve can be converted into molecules of EGF molecules/μm^2 through background subtraction and subsequent division by the F factor and the slope of the standard curve.

Synthesis of Biotin-EGF-Dye Conjugates

EGF (R&D Biosystems) was labeled with either Alexa 647, 488, or Cy3 succinimidyl esters (Invitrogen) and NHS-biotin (Pierce) in a single-pot reaction as previously described.[16] Briefly, 100 µL of EGF (1 mg/mL) was combined with 10 µL of 1 M sodium bicarbonate and a ten-fold molar excess of dye and NHS-biotin. The reaction was incubated for 1 h after which it was purified with Bio-Gel P4 resin (Bio-Rad). This reaction typically yielded protein with a labeling ratio between 1 and 2.

Fabrication of Chromium Diffusion Barriers

Clean glass coverslips were spin-coated at 2500 RPM with electron beam resist, NANO™PMMA 495 A4 (MicroChem Co., Newton, MA). A chromium dissipation layer with a thickness of 10 nm was deposited onto the samples via electron beam evaporation. Samples were exposed in a JEOL JBX9300FS electron beam lithography tool operating at 100 kV and 2 nA with a dose of 1200 $\mu C/cm^2$. Following removal of the Cr dissipation layer in Cr etchant, samples were developed for 1 minute in 1:3 Methyl isobutyl ketone (MIBK): isopropyl alcohol (IPA), rinsed with IPA and dried with N_2. Samples were subjected to brief (6 s) oxygen plasma treatments to remove any organic residue in the developed areas. Electron beam evaporation was used to deposit a thin film of Cr as a barrier layer. Sonication of the samples in acetone for approximately

2 minutes removed the patterned PMMA leaving Cr barriers in the areas previously exposed and developed during EBL processing.

3.8 Acknowledgements

Acknowledgements

We would like to thank the Oak Ridge National Lab Center for Nanophase Materials Sciences (CNMS 2009-269) for fabricating the chromium diffusion barrier substrates, and Dr. Rita Nahta at the Winship Cancer Center for the gift of cell lines used herein. K.S. would like to acknowledge support from the National Institutes of Health (NIH) through R01-GM097399-01, seed funding through the NIH NHLBI Program Excellence in Nanotechnology (HHSN268201000043C), and seed funding through the Emory University Research Committee (URC) 00016401.

3.9 References

1. Salaita, K., Nair, P. M., Petit, R. S., Neve, R. M., Das, D. et al., *Science* **327** (5971), 1380 (2010).

2. Manz, B. N., Jackson, B. L., Petit, R. S., Dustin, M. L., and Groves, J., *Proceedings of the National Academy of Sciences of the United States of America* **108** (22), 9089 (2011).

3. Orth, R. N., Wu, M., Holowka, D. A., Craighead, H. G., and Baird, B. A., *Langmuir* **19** (5), 1599 (2003).

4. Wu, M., Holowka, D., Craighead, H. G., and Baird, B., *Proceedings of the National Academy of Sciences of the United States of America* **101** (38), 13798 (2004).

5. Fewtrell, C. and Metzger, H., *Journal of Immunology* **125** (2), 701 (1980).

6. Kiessling, L. L., Gestwicki, J. E., and Strong, L. E., *Angewandte Chemie International Edition* **45** (15), 2348 (2006).

7. Cochran, J. R., Cameron, T. O., and Stern, L. J., *Immunity* **12** (3), 241 (2000).

8. Triantafilou, M., Gamper, F. G. J., Haston, R. M., Mouratis, M. A., Morath, S. et al., *Journal of Biological Chemistry* **281** (41), 31002 (2006).

9. Chung, I., Akita, R., Vandlen, R., Toomre, D., Schlessinger, J. et al., *Nature* **464** (7289), 783 (2010).

10. Abulrob, A., Lu, Z., Baumann, E., Vobornik, D., Taylor, R. et al., *Journal of Biological Chemistry* **285** (5), 3145 (2010).

11. Hofman, E. G., Bader, A. N., Voortman, J., Van Den Heuvel, D. J., Sigismund, S. et al., *Journal of Biological Chemistry* **285** (50), 39481 (2010).

12. Ichinose, J., Murata, M., Yanagida, T., and Sako, Y., *Biochemical and Biophysical Research Communications* **324** (3), 1143 (2004).

13. Clayton, A., Orchard, S., Nice, E., Posner, R., and Burgess, A., *Growth Factors* **26** (6), 316 (2008).

14. Szabó, Á., Horváth, G., Szöllosi, J., and Nagy, P., *Biophysical Journal* **95** (4), 2086 (2008).

15. Nam, J.-M., Nair, P. M., Neve, R. M., Gray, J. W., and Groves, J. T., *ChemBioChem* **7** (3), 436 (2006).

16. Stabley, D. R., Jurchenko, C., Marshall, S. S., and Salaita, K. S., *Nat Meth* **9** (1), 64 (2012).

17. Wang, J., Yu, X., Boriskina, S. V., and Reinhard, B. r. M., *Nano Letters* (2012).

18. Yarden, Y. and Sliwkowski, M., *Nature Reviews Molecular Cell Biology* **2** (2), 127 (2001).

19. Qi, S., Groves, J., and Chakraborty, A., *Proceedings of the National Academy of Sciences of the United States of America* **98** (12), 6548 (2001).

20. Mossman, K. D., Campi, G., Groves, J. T., and Dustin, M. L., *Science* **310** (5751), 1191 (2005).

21. Grassmé, H., Jekle, A., Riehle, A., Schwarz, H., Berger, J. et al., *Journal of Biological Chemistry* **276** (23), 20589 (2001).

22. Grassmé, H., Cremesti, A., Kolesnick, R., and Gulbins, E., *Oncogene* **22** (35), 5457 (2003).

23. Scott, F. L., Stec, B., Pop, C., Dobaczewska, M. K., Lee, J. J. et al., *Nature* **457** (7232), 1019 (2009).

24. Jay T, G., *Current Opinion in Chemical Biology* **10** (6), 544 (2006).

25. Xu, Q., Lin, W.-C., Petit, R. S., and Groves, J. T., *Biophysical Journal* **101** (11), 2731 (2011).

26. Cohen, S., Carpenter, G., and King, L., *Journal of Biological Chemistry* **255** (10), 4834 (1980).

27. Lax, I., Mitra, A. K., Ravera, C., Hurwitz, D. R., Rubinstein, M. et al., *Journal of Biological Chemistry* **266** (21), 13828 (1991).

28. Yang, S., Raymond-Stintz, M. A., Ying, W., Zhang, J., Lidke, D. S. et al., *Journal of Cell Science* **120** (16), 2763 (2007).

29. Nagy, P., Claus, J., Jovin, T., and Arndt-Jovin, D., *Proceedings of the National Academy of Sciences* **107** (38), 16524 (2010).

30. Narui, Y. and Salaita, K. S., *Chemical Science* **3** (3), 794 (2012).

31. Galush, W. J., Nye, J. A., and Groves, J. T., *Biophysical Journal* **95** (5), 2512 (2008).

32. Hu, M., Scollard, D., Chan, C., Chen, P., Vallis, K. et al., *Nuclear Medicine and Biology* **34** (8), 887 (2007).

33. Platt, M., Roman, A., Wells, A., Lauffenburger, D., and Griffith, L., *Journal of Cellular Physiology* **221** (2), 306 (2009).

34. Fan, V. H., Au, A., Tamama, K., Littrell, R., Richardson, L. B. et al., *Stem Cells* **25** (5), 1241 (2007).

35. Lohmüller, T., Iversen, L., Schmidt, M., Rhodes, C., Tu, H. L. et al., *Nano Letters* **12** (3), 1717 (2012).

36. Chiang, E. N., Dong, R., Ober, C. K., and Baird, B. A., *Langmuir*, 110510130404039 (2011).

37. Lidke, D. S., Nagy, P., Heintzmann, R., Arndt-Jovin, D. J., Post, J. N. et al., *Nature Biotechnology* **22** (2), 198 (2004).

38. Lidke, D. S., Lidke, K. A., Rieger, B., Jovin, T. M., and Arndt-Jovin, D. J., *J. Cell Biol.* **170** (4), 619 (2005).

39. Vieira, A., Lamaze, C., and Schmid, S., *Science* **274** (5295), 2086 (1996).

40. Lemmon, S. K. and Traub, L. M., *Traffic* **13** (4), 511 (2012).

41. von Kleist, L., Stahlschmidt, W., Bulut, H., Gromova, K., Puchkov, D. et al., *Cell* **146** (3), 471 (2011).

42. Zhang, X., Gureasko, J., Shen, K., Cole, P. A., and Kuriyan, J., *Cell* **125** (6), 1137 (2006).

43. Marcantonio, N., Boehm, C., Rozic, R., Au, A., Wells, A. et al., *Biomaterials* **30** (27), 4629 (2009).

44. Kuhl, P. R. and Griffith-Cima, L. G., *Nature Medicine* **2** (9), 1022 (1996).

45. Singh, A. B. and Harris, R. C., *Cellular Signalling* **17** (10), 1183 (2005).

46. Nair, P. M., Salaita, K., Petit, R. S., and Groves, J. T., *Nature protocols* **6** (4), 523 (2011).

Chapter 4: Simultaneous Two-Wavelength Axial Ratiometry (STAR) for Real-time Imaging of Protein Dynamics with 20 nm Resolution in Living Cells

4.1 Introduction

The majority of biological processes involve intricate spatial and temporal coordination of many proteins to form assemblies. Accordingly, the advent of super-resolution imaging methods, including STED[1], STORM[2], SIM[3] and PALM[4,5], have greatly advanced our understanding of a range of cellular structures from focal adhesions to the neuronal cytoskeleton[6,7]. While these techniques have been revolutionary in improving optical resolution, they have drawbacks. This is particularly the case for imaging dynamics along the optical axis, perpendicular to the sample. In optical microscopy, the axial, or *z* resolution is generally worse compared to the *x-y* resolution due to the inherent elliptical shape of the Airy disk, according to the laws of Abbe.

4.2 Total Internal Reflection Fluorescence (TIRF)

One of the simplest methods to improve optical axis resolution is total internal reflection fluorescence microscopy (TIRF).[8,9] This imaging mode arises when a laser is shone above the critical angle to a given optical interface, giving rise to a field of non-propagating light that decays exponentially from the surface (the evanescent field). The decay of the field is governed by the following equations:

$$I = I_0 \; e^{-\; z/\mathrm{d}}$$

$$d = \frac{\lambda}{4\pi}\sqrt{(n_1{}^2 sin^2\theta - n_2{}^2)}$$

where I_0 is the intensity at $z = 0$, n_1 and n_2 are the indices of refraction of the glass coverslip and the sample, respectively, λ is the excitation wavelength, and θ is the angle of incidence.

Given this relation, TIRF limits the illumination volume of the sample as compared to epifluorescence excitation, making it an ideal method for imaging cell membrane associated proteins with minimal interference from cytosolic species. While high-contrast imaging of membrane-associated proteins is a key feature of TIRF imaging, a number of elegant approaches have been developed that take advantage of the exponentially decaying nature of the evanescent field to image samples along the z axis with nanoscale resolution. The relative distance of fluorescently labeled targets from the coverslip surface can be obtained via TIRF imaging by comparing the fluorescence value of fluorophores close to the surface with fluorophores that are further away.[10] Quantification of this method is challenging, however, as any change in fluorescence intensity that is not due to z position shift (such as changing dye density) will introduce systematic error into the measurement. Several robust techniques based on TIRF have been developed to minimize these density-dependent effects. For example, differential evanescent nanometry (DiNa) uses pairs of sequential TIRF and epifluorescence images to measure z position.[11] This technique can tolerate some changes in the number of fluorophores due to the fact that all of the TIRF images ratiometrically corrected by epifluorescence images. Therefore, as long as the number of fluorophores does not change more quickly than the sequential pair of TIRF and epifluorescence images can be acquired, the technique reports accurate z measurements. Another technique known as scanning angle TIRF allows z position to be determined by acquiring a series of TIRF images with different incidence angles. Interestingly, both of these approaches predate the popularization of super-resolution imaging, but have not gained widespread use due, in part, to the limitations in characterizing the dynamic nature of most biological structures at the plasma membrane. For example, both the composition and the location of a clathrin-coated pit changes as it matures, which convolutes sequential TIRF-based axial measurements such as scanning angle TIRF. In the case of DiNa, some of these structures can be studied, but any change in the number of fluorophores in the space

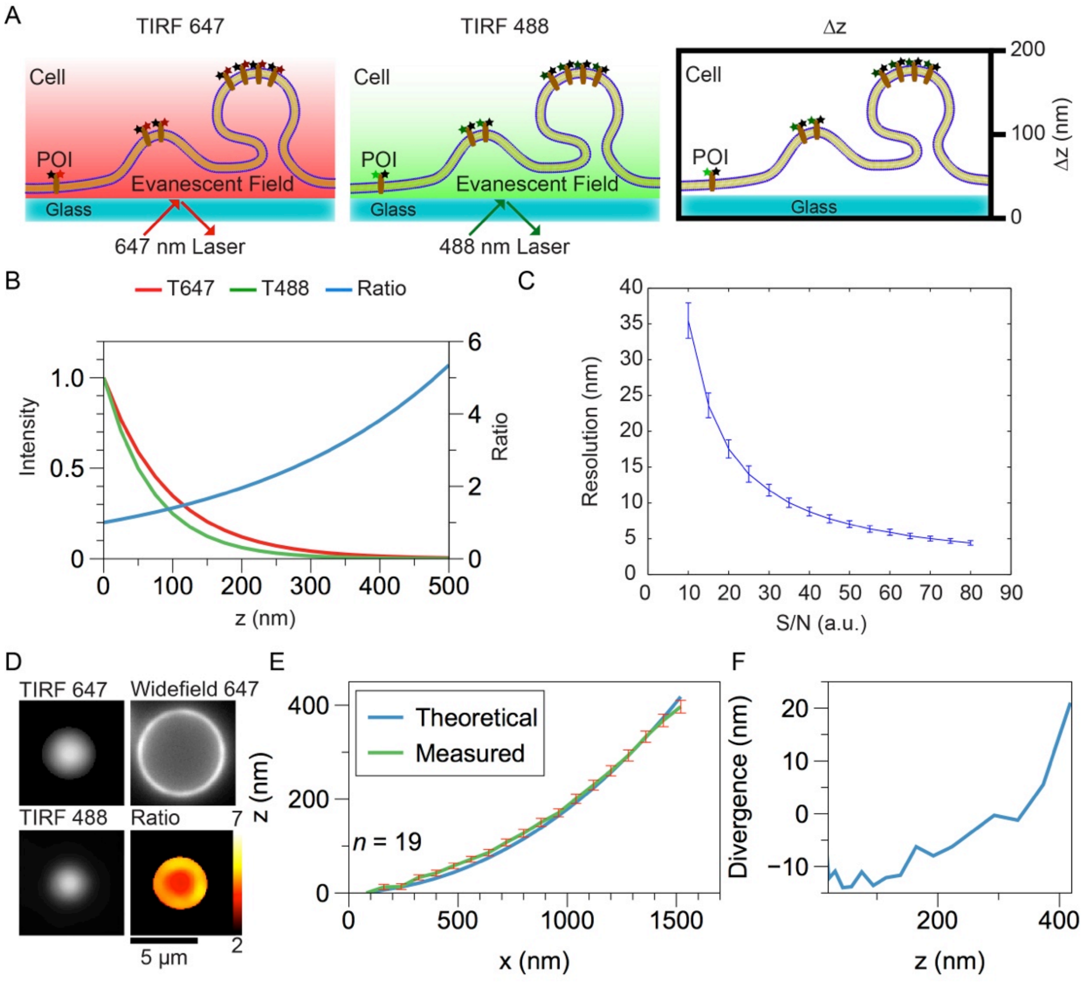

Figure 4.1: Theory and Demonstration of STAR
(A) Schematic showing the basic principal of STAR: the z position of a target protein labeled with two distinct fluorophores is determined by imaging in two TIRF channels and calculating the intensity ratio between the two channels. (B) The theoretical evanescent field intensity for 647 (red) and 488 (green) nm excitation light and the ratio of 647/488 (blue) as a function of distance from the coverslip (z) (C) Relationship between resolution and signal to noise; error bars are standard deviation across delta z from 5-400nm.Isocontours of the expected resolution of STAR plotted as a function of signal to noise in the green fluorescence channel and the z position measured from the coverslip. (D) Representative images of a dual-tagged silica microsphere. (E) The theoretical (blue) and measured (green) *z* position as a function of distance from the center of the bead (x). The measured represents an average of 19 beads of identical diameter. (G) Divergence between the average measured and theoretical z position as a function of z.

between when the TIRF and epifluorescence images are acquired will make any measured *z* positions inaccurate. Likewise, scanning angle interference (an interferometry based imaging technique) provides ~10 nm axial resolution, but also requires collecting a sequence of images (~10 images) of relatively static structures near the plasma membrane (within ~800 nm)[12]. This limits scanning angle interference to imaging structures such as the focal adhesion complex and microtubules that remain relatively static over the relevant time scales.

4.3 Theory

Herein we present a simple method, simultaneous two-wavelength axial ratiometry (STAR), for measuring z positions with 20 nm axial resolution in real-time, overcoming the need for sequential imaging. In STAR, the sample is excited with two wavelengths, each with a unique evanescent decay constant, to measure the axial position of dual-tagged molecules (Fig. 4.1 A). The intensity profile of the excitation field is unique for each wavelength, resulting in an axial position-dependent intensity ratio between of the two fluorescent channels (Fig. 4.1 B). An object tagged with two fluorophores (each specifically excited by only one of the excitation wavelengths) will have a change in fluorescence intensity ratio as it moves along the optical axis. The change in height from a reference point is calculated by:

$$\Delta z = \ln\left[\frac{R}{R_0}\right]\frac{1}{\gamma}$$

where R is the ratio of fluorescence emission intensities between two TIRF channels (in this case excitation of 488 nm and 647 nm), R_0 is the ratio of fluorescence emission intensities at a baseline z-position, and γ is a constant derived from the evanescent fields (see section 4.8 for a derivation of this relationship) . Thus, height can be accurately measured in real-time so long as the angle of incidence and indices of refraction remain fixed. Importantly, the ratio of emission is independent of the concentration of the dyes or fluorescent proteins used to label target species, making

STAR measurements of Δ*z* robust to changes in protein number or concentration as compared to similar techniques. Additionally, the use of an optical splitter with STAR allows real-time imaging of protein assembly events since nanoscale *z* positions can be calculated from a single fluorescence image.

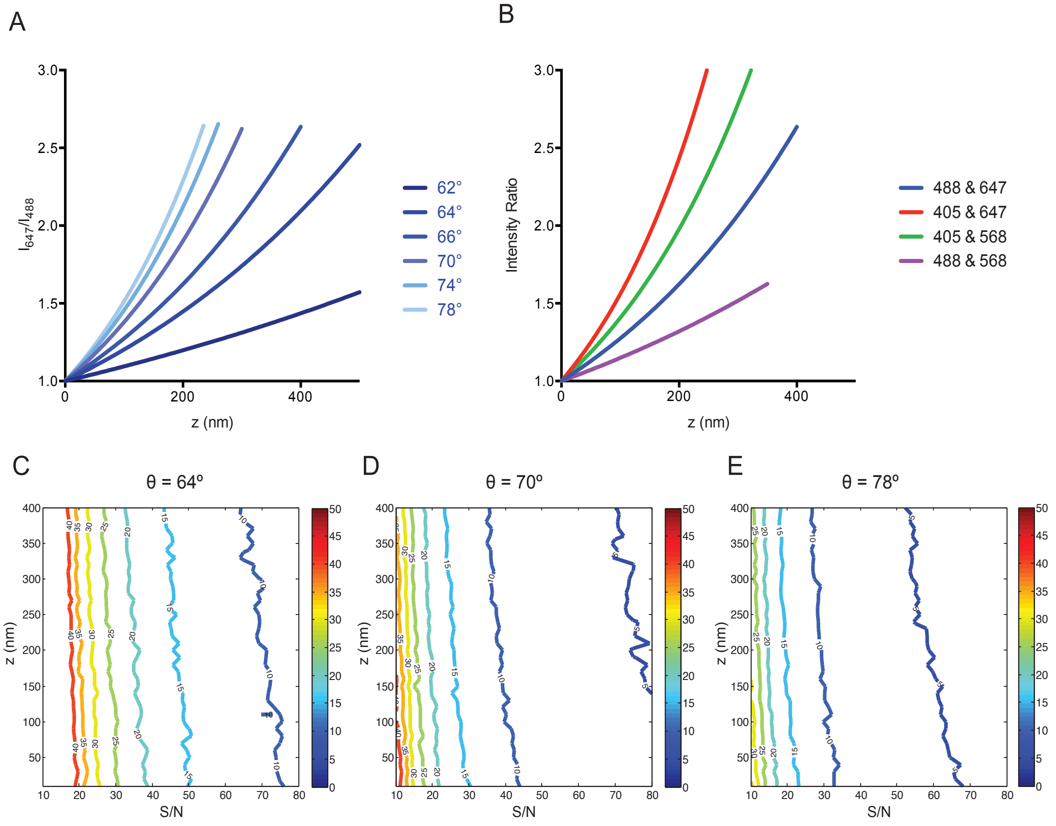

Figure 4.2 Theoretical modeling of STAR
(A) The ratio of the 647 and 488 nm TIRF excitation fields as a function of distance from the coverslip/sample interface for incidence angles ranging from 62-78°. The data is plotted to a z distance where the I_{647} = 5% I_{647} at $z = 0$. The incidence angle controls the rate of change of the ratio and the *z* depth to which the technique is applicable. (B) The ratio of excitation fields for different wavelength combinations where $\theta = 66°$. (C-E) Isosurface contour plots of the theoretical resolution of a z measurement as a function of the S/N of the green channel. Resolution is defined as the minimum distance that two objects could be distinguished. The parameters used were λ= 647 and 488 nm and an incidence angle (C) $\theta = 64°$, (D) $\theta = 70°$, and (E) $\theta = 78°$. For all calculations, $n_1 = 1.515$ and $n_2 = 1.33$.

To determine the theoretical resolution of STAR, we generated a simulation of raw fluorescence data incorporating shot noise, while also varying protein concentration, *z*-position, and incidence angle. This analysis revealed that the theoretical resolution depends heavily on the signal-to-noise ratio (S/N), and can be as small as 5 nm when an object is bright and near the coverslip (Fig. 4.1 C). However, as the object moves away from the coverslip, the S/N will decrease and reduce the resolution of STAR. For example, the localization precision of a structure 10 nm from the coverslip is ± 8 nm, in contrast to the precision of ± 21 nm when the same object is 400 nm away from the coverslip. Note that the resolution can be tailored to specific height ranges by changing the incidence angle (Fig. 4.2).

4.4 The Effects of FRET on STAR Imaging

Since STAR employs simultaneous two-wavelength excitation, it is important to consider how Förster resonance energy transfer (FRET), both intermolecular and intramolecular, may affect height measurements. Assuming that the average molecular conformation of the protein target is constant, intramolecular FRET efficiency between the two reporter dyes will also remain constant. Since FRET efficiency is an inherent molecular property, its value will be independent of labeling density.

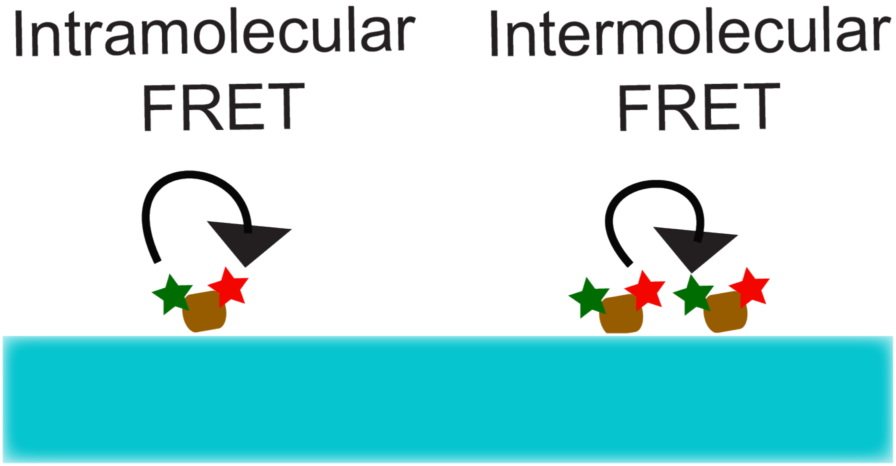

Figure 4.3: Schematic illustrating the process of intramolecular and intermolecular FRET, which may alter the accuracy of STAR.

FRET can occur between two distinct fluorophores on the same target molecule (intramolecular FRET) or between two distinct fluorophores in proximity but on separate molecules in the case of intermolecular FRET (Fig. 4.3). Each of these cases has a distinct effect on STAR measurements that is further compounded by the microscope configuration used during data acquisition. Samples are either imaged in each channel sequentially (for the bead and microtubule experiments) or simultaneously, using an optical splitter (for the live cell EGFR experiments). The following sub-sections will discuss each case in detail, and describe what corrections (if any) must be made in order to acquire accurate height information.

The first case to consider is that of intramolecular FRET with sequential excitation. In this case, samples are imaged using a quad-band TIRF filter cube that passes the emission and excitation light from both channels, but the sample is excited with the wavelengths corresponding to the individual donor and acceptor channels. An important consideration regarding intramolecular FRET is that the FRET efficiency is

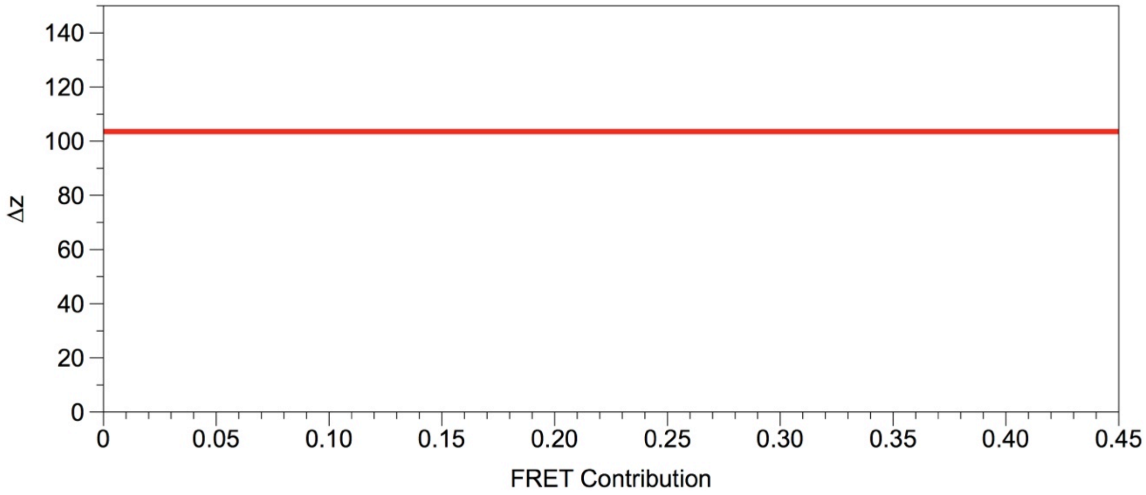

Figure 4.4: Simulation showing that the STAR height measurement is independent of intramolecular FRET. Plot displays the resulting Δz that is obtained from sequential excitation of donor and acceptor over a range of intramolecular FRET efficiencies.

constant. Therefore, the additional signal in the acceptor channel due to FRET remains as a constant percentage throughout the entire sample. When the sample is exposed to donor excitation, the resulting signal is a composite of the donor emission, as well as FRET emission (due to the fact that the quad-band cube passes the emission of both channels). Importantly, since this signal is solely the result of donor excitation, it will vary according to the evanescent field decay function of the donor. Given that the acceptor excitation only yields acceptor signal, intramolecular FRET does not affect the final measurement (Fig. 4.4). Thus, when sequentially exciting the donor and acceptor channels, no correction is necessary for intramolecular FRET. The equation for the donor signal in this case is given by the equation:

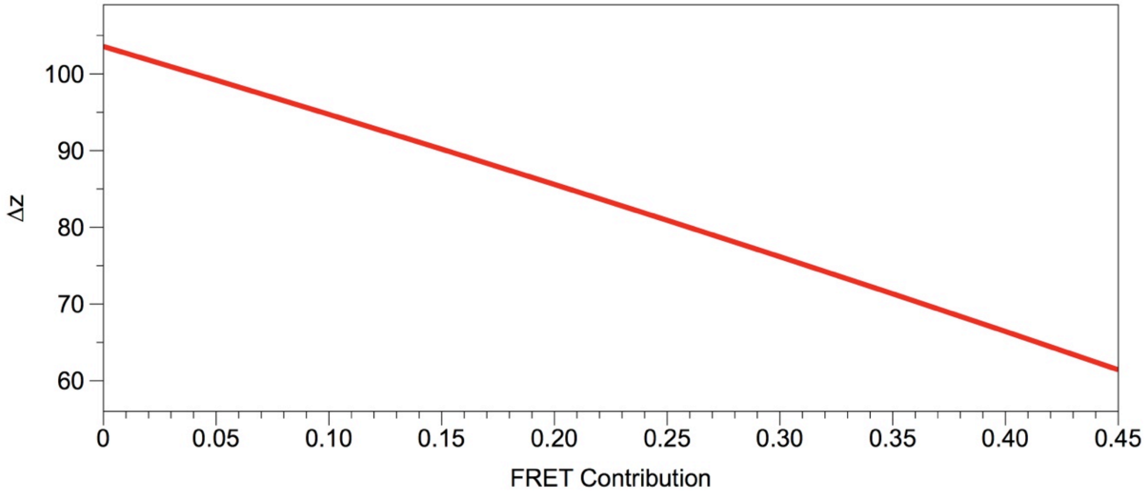

Figure 4.5: Simulation showing resulting Δz from simultaneous excitation of donor and acceptor over a range of intramolecular FRET efficiencies.

$$I_D = I_{0D}(e^{-z/d_D}) + E_{FRET}(I_{0D}(e^{-z/d_D}))$$

where I_D is the total measured signal in the donor channel, I_{0D} is the donor intensity at z = 0, d_D is the evanescent field decay function for the donor excitation wavelength, and E_{FRET} is the FRET efficiency. When intramolecular FRET is present and the sample is imaged with simultaneous dual-channel excitation on an emission splitter, there are additional factors to consider. Importantly, intramolecular FRET will alter both acceptor and donor intensities (as all emission light from the acceptor sent to the same part of the sensor by the splitter). This creates a situation where the acceptor signal has components corresponding to two separate decay functions: the acceptor signal which corresponds to the decay function from the acceptor excitation wavelength, as well as the acceptor signal due to FRET which corresponds to the decay function from the donor excitation wavelength. This convolution of two decay functions creates a discrepancy in the ratios, leading to inaccurate reporting of height values (Fig. 4.5), while the donor signal remains unaffected. The equation for the acceptor signal is as follows:

$$I_A = I_{0A}(e^{-z/d_A}) + E_{FRET}(I_{0D}(e^{-z/d_D}))$$

where I_A is the total measured signal in the acceptor channel, I_{0A} is the acceptor intensity

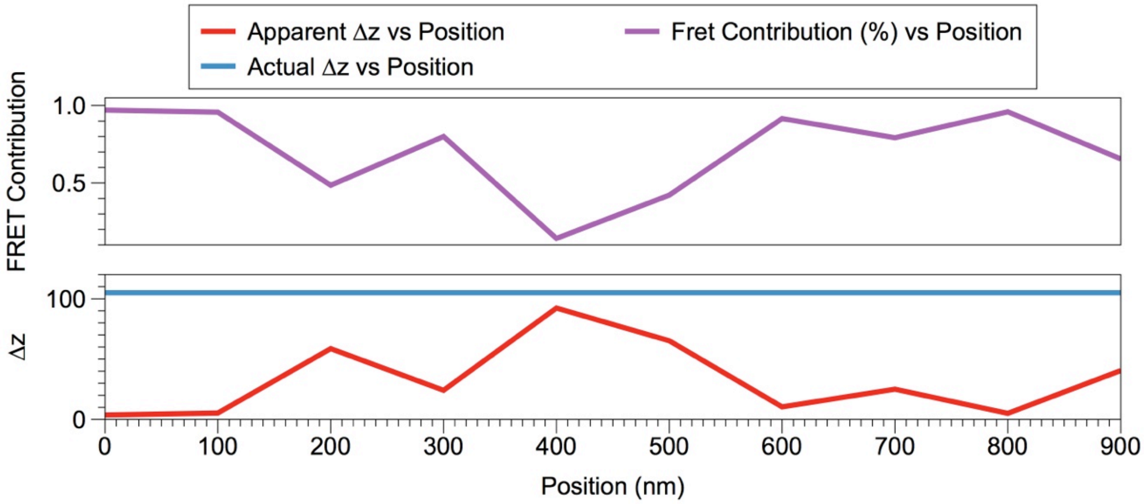

Figure 4.6: Simulation showing the effect of intermolecular FRET on measured Δz across a theoretical sample where FRET efficiency varies as a function of label density.

at z = 0, and d_A is the evanescent field decay function for the acceptor excitation wavelength. The discrepancy in such cases can be overcome by subtracting the FRET contribution directly from the acceptor image. This can be accomplished by measuring the FRET contribution to the acceptor channel and then multiplying this percentage by the donor image, followed by subtracting the resulting correction image from the acceptor image.

In the case of intermolecular FRET, the signal behaves exactly as described in the above sections, depending on the imaging setup. The difference, however, is that intermolecular FRET efficiencies will change depending on the density of target proteins. This means that across a labeled sample the FRET efficiency could vary, giving rise to a non-constant discrepancy in the measured Δz (Fig. 4.6).

When intermolecular FRET occurs during sequential excitation, the FRET signal will be added to the donor channel as seen previously. As the FRET efficiency will vary over the sample in this case, however, this contribution cannot be ignored. In this case, the intermolecular FRET discrepancy can be corrected by normalizing the TIRF ratio image. This method is effective, as the widefield ratio is identical to the TIRF ratio at z = 0. This means that dividing the TIRF ratio image by the widefield ratio image will function as an accurate baseline, as each position of the widefield image consists of the correct ratio according to the local FRET efficiency. In the case of intermolecular FRET with simultaneous donor and acceptor excitation, the only way to correct the discrepancy is to measure the FRET efficiency at every position of the image across all time points. As this would greatly slow down the rate of imaging for dynamic cell experiments, it is best to engineer live cell experiments such that intermolecular FRET is minimized.

4.5 Proof of Concept

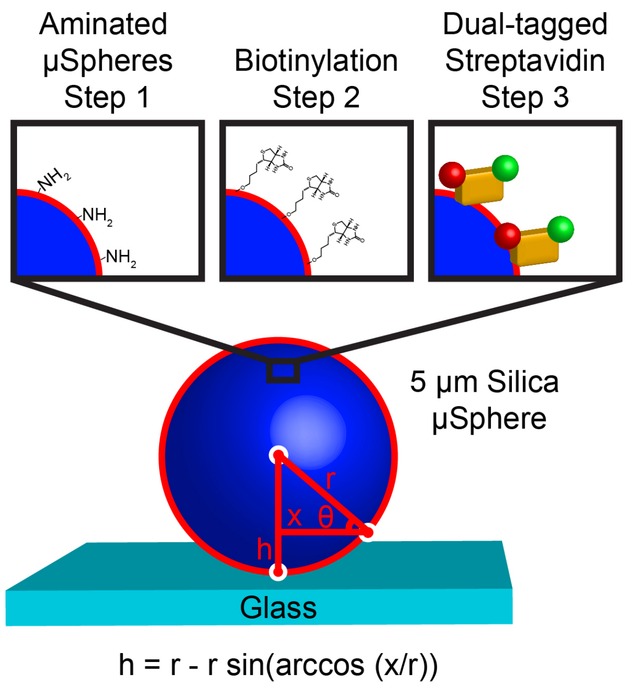

Figure 4.7: Schematic showing the use of silica microspheres for proof of concept measurements.

To validate the accuracy of STAR measurements, we imaged fluorescently labeled silica microspheres with a known geometry and a low refractive index.[13] The height of the bead from the coverslip is a function of the distance from the center of the sphere, and can be described by simple trigonometry (Fig. 4.7). 5-micron biotin-modified silica microspheres were functionalized with dual-labeled streptavidin (Alexa647 and Alexa488). These particles were deposited onto a glass coverslip and then mounted in index-matched media and imaged using STAR (Fig. 4.1 D). In order to expedite the analysis of the silica microspheres used for proof of concept experiments, custom software was written in MATLAB. The following is an overview of how the software functions.

First, the gamma constant is calculated from the incidence angle, excitation wavelengths, and indices of refraction for a given set of bead images. A master image stack consisting of the TIRF 647 nm, TIRF 488 nm, widefield 647 nm and widefield 488 nm channels for each individual field of view is then opened and stored in the memory. Following this, the non-homogeneity in the TIRF excitation intensity in each individual T647 nm and T488 nm image was corrected by dividing each image using a standard image of a fluorescent supported lipid bilayer. These normalized images were stored. The user is then prompted to select beads manually from a widefield image, allowing pre-screening for beads that do not have obvious defects. The bead diameter is then automatically measured from the epifluorescence image, and a 2D Gaussian is then fit to each bead in the TIRF channels to determine the centroid of the bead. Next, the pixels that make up an individual bead are binned based on their distance from the bead center,

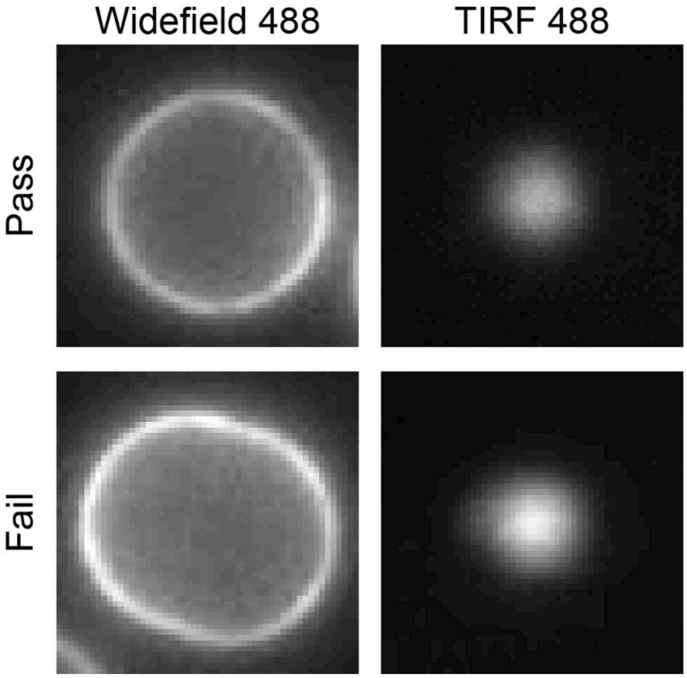

Figure 4.8: Representative images of beads that were either analyzed or discarded.

and the mean and coefficient of variation are then taken for each bin. This leaves a graded measurement of the fluorescence intensity as a function of distance from the bead center. Importantly, beads for which the coefficient of variation is larger than 0.4 in any given bin are discarded from the analysis, as manufacturing irregularities in bead shape will cause divergence from the trigonometry used to calculate theoretical values (Fig. 4.8). After the distance-correlated fluorescence information is obtained for each TIRF channel, the software calculates the ratio and Δz as previously described. Theoretical values for Δz are generated using basic trigonometry to describe the profile of the bead along with the previously calculated evanescent field decay functions. Finally, beads are binned together and averaged according to their diameter (as different diameter beads will have different z profiles), and the average Δz profile for beads of a given diameter is compared to that of the theoretical values.

The ratio of the TIRF images in the 488 and 647 nm channels was used to determine the height profile of the surface of the bead. The measured and theoretical axial profiles were in agreement. To determine the accuracy of the measurement, we generated a height profile for ten beads with similar diameters, and compared this measurement with the predicted height profile (Fig. 4.1 E). Note that the deviation from the predicted height profile increases at greater z-positions which is expected given the reduction in S/N. Nonetheless, the maximum deviation from the predicted height value was 21 nm over a range of 400 nm, thus STAR is expected to accurately measure z positions within 21 nm over a range of 0-400 nm above the coverslip (Fig. 4.1 F). Again it is important to note that objects closer to the coverslip can be localized with a greater degree of accuracy, thus the average deviation over this range is 8.4 nm.

4.6 Mapping Microtubule z Positions with STAR

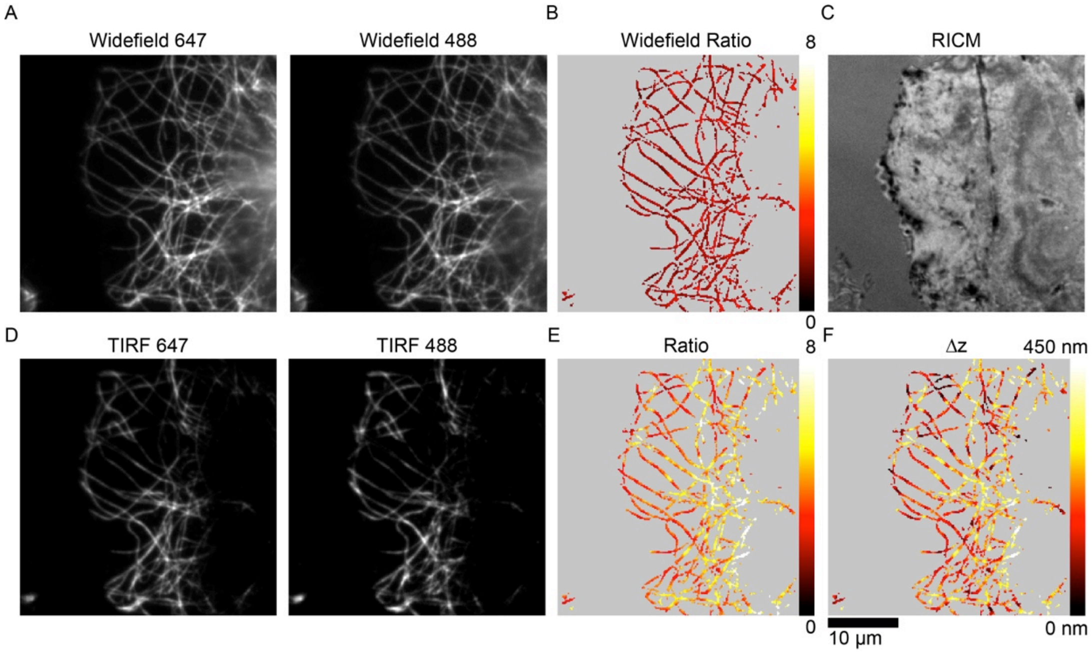

Figure 4.9: Measuring the height of microtubules along the optical axis using STAR with standard immunofluorescence.
(A) Widefield images of COS-7 cells stained with anti ß-tubulin primary antibody and dual-tagged streptavidin. (B) Ratio of the widefield images. (C) RICM images of the cells showing the adhesion profile of the cell. (D) Representative TIRF images of the cell. (E) Ratio of the TIRF images. (F) Δz map which was calculated from the TIRF and widefield ratios.

Having established the accuracy of the technique, we next used STAR to create a height map of microtubules in fixed cells. COS7 cells were fixed and microtubules labeled with a biotinylated primary antibody and Alexa488-Alexa647 tagged streptavidin. Cells were imaged with widefield (Fig. 2A-B) and TIRF (Fig. E-F) in both the 488 nm and 647 nm channels. Compared to the widefield channels, only microtubules near the coverslip are visible in TIRF. The ratio of the two widefield channels was uniform (1.9 ± 0.3) for all microtubules in the cell (Fig. 2C). This was expected because the widefield ratio simply reflects the product of the detected brightness of the Alexa488 and Alexa647 dyes and their respective labeling ratios. In contrast, the TIRF ratio varied from 1 to 7 along individual microtubules, displaying a general decrease in the ratio near the cell edge (Fig. 2G) corresponding to the cell-substrate contact regions captured with RICM (Fig. 2D).

To determine the nanometer *z*-position, the TIRF images for each channel were background subtracted and divided to obtain a ratio (Fig. 4.10). The baseline ratio corresponding to a *z* position of zero was determined from the background corrected ratio of the widefield images, which corrects for FRET contributions. The height map was then calculated using equation 2 (Fig. 2H). RICM shows that the association of the plasma membrane and the substrate is close at the edge of the cell and increases towards the center. Likewise, the microtubules towards the edge of the cell are generally located between 0 and 100 nm and increase in height toward the center of the cell. These values agree with published *z* positions obtained using scanning-angle interference.[12] One important caveat is that STAR is diffraction limited in the *x-y* plane. Accordingly, when two target proteins are located within a single diffraction limit, the STAR height measurement is biased and rather than reporting the average height of both microtubules, it will report a weighted average that is biased toward objects that are near the glass coverslip.

4.7 Real-time Imaging of EGFR Internalization

To demonstrate the ability of STAR to capture dynamics, we next measured the nanometer *z*-position of the epidermal growth factor receptor (EGFR) during ligand binding, clustering, and internalization at the plasma membrane. Endocytosis is a well-suited process to study with STAR, as it involves a host of rapidly assembling proteins, with translocations in the axial direction. EGFR internalization via clathrin mediated endocytosis is well-characterized and can be triggered by addition of its ligand, EGF.[14]

We designed a plasmid where the C-terminus of EGFR was tandem tagged with enhanced green fluorescent protein (EGFP) and infrared fluorescent protein (iRFP) (Fig. 4.11 A). These two fluorophores were selected to minimize FRET, as there is minimal overlap between the fluorescence emission peak of EGFP and the fluorescence excitation peak of iRFP (Fig. 4.12). Transiently transfected COS-7 cells expressing EGFR-EGFP-iRFP were imaged using STAR. For real-time acquisition, dual channel TIRF images were simultaneously acquired using a commercially available emission splitter. The dual tagged receptor was observed in both the TIRF 647 and 488 channels (Fig. 4.11 B), and was laterally mobile within the cell membrane. An exponential frame-by-frame

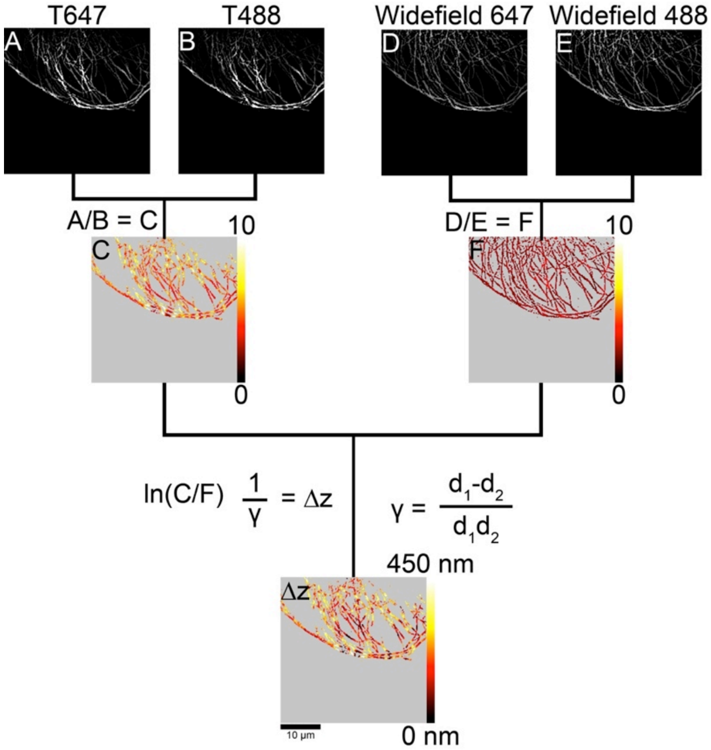

Figure 4.10: Derivation of z position from initial TIRF images.
Representative scheme showing how z position is calculated from fluorescence images. Ratios (C and F) are determined between both the TIRF images (A and B) and widefield images (D and E). The TIRF ratio map is then divided by the widefield map as a baseline, whereupon the equations shown are applied across the resulting image to generate a z map.

photobleaching correction was applied to all time-lapse experiments (Fig. 4.13). It is important to note that all STAR experiments rely on the presence of both dye molecules

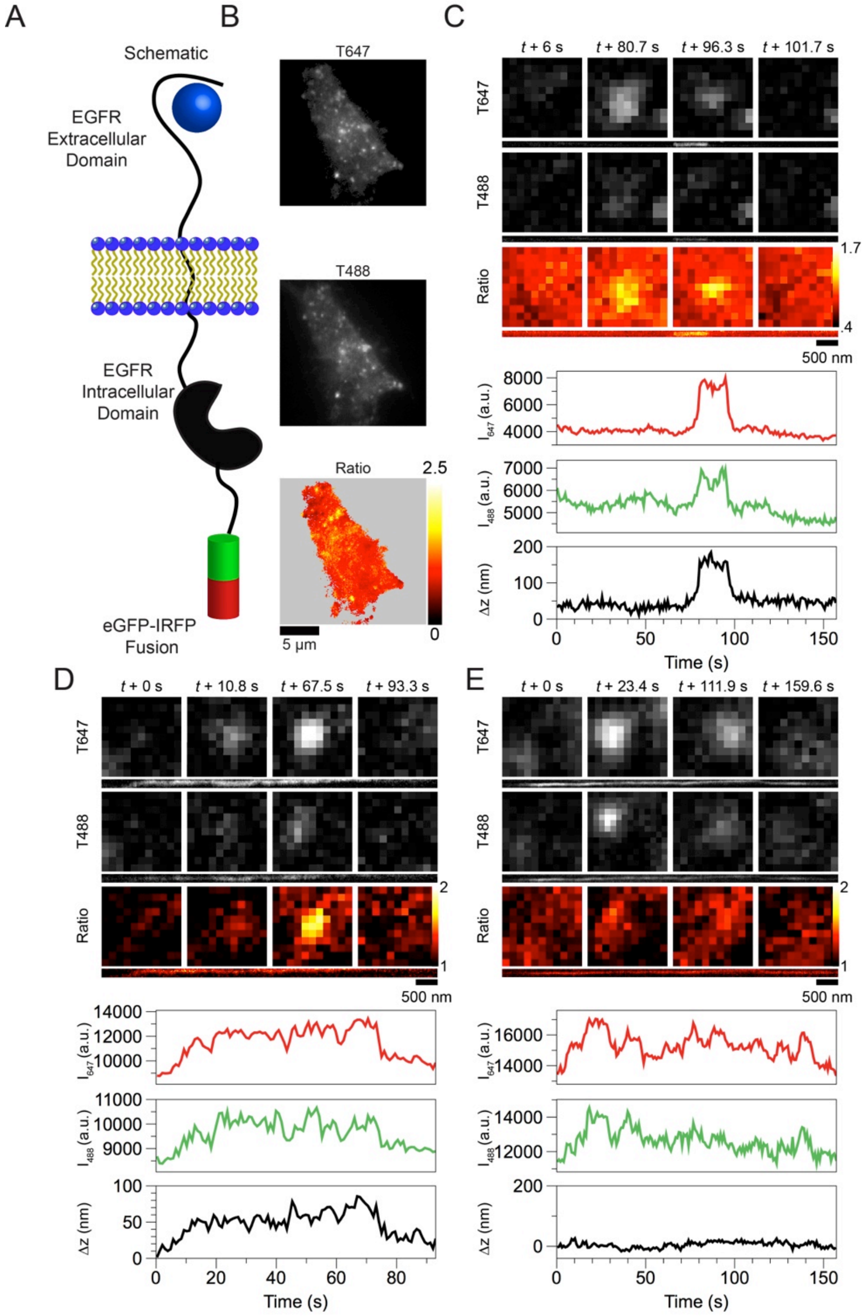

Figure 4.11: Imaging EGFR endocytosis in real time with STAR.
(A) Schematic of the eGFP-iRFP tagged EGFR. (B) A COS-7 cell expressing EGFR-EGFP-iRFP after EGF stimulation imaged in TIRF647 and TIRF488 and the ratio. (C-E) Traces and representative images of individual EGFR puncta. Below each set of fluorescent images is a kymograph of the puncta over the entire time series. Graphs show the mean intensity of the puncta in each channel and the calculated Δz over time.

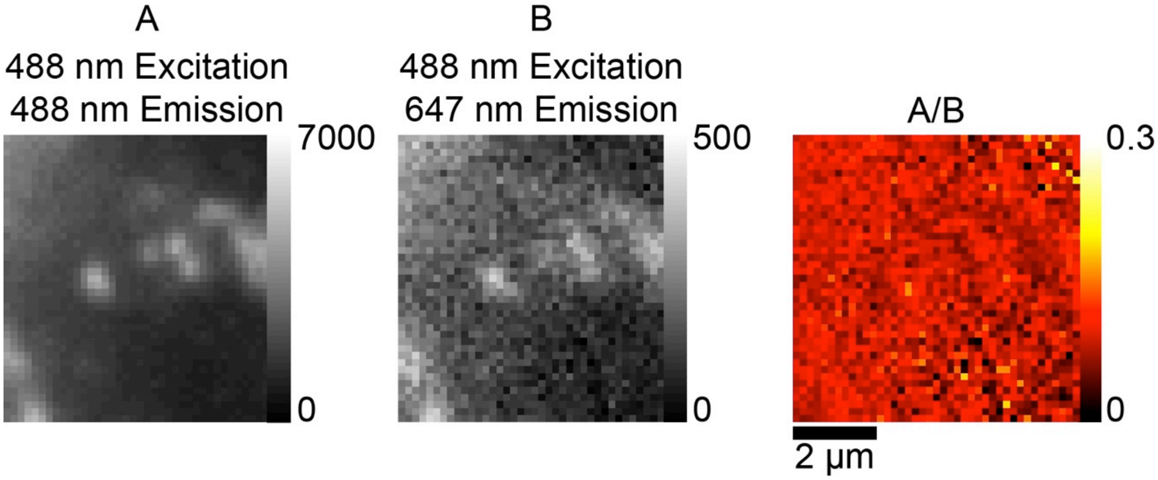

Figure 4.12: FRET signal levels for dual-tagged EGFR experiments.
Representative images show the fluorescence intensity of the donor (T488) channel and the corresponding FRET signal. The ratio of the FRET signal divided by the donor signal serves to demonstrate that the FRET signal does not vary greatly between diffuse EGFR and EGFR in puncta.

on the target protein. In order to illustrate this point, we transfected COS-7 cells with EGFP-EGFR and iRFP-EGFR as separate constructs. Images of these cells reveal false Δz measurements due to differential expression and localization of the separately tagged target proteins (Fig. 4.14).

Analysis of individual puncta revealed several behaviors. A subset of puncta had dynamic changes in *z*. The dynamics followed a pattern of a rapid increase in z as the fluorescence intensity increased followed by a rapid return to the baseline that coincided with loss of fluorescence and disappearance of the puncta from the evanescent field (Fig. 4.11 C-D). This pattern of *z* positions is indicative of our predictions for EGFR internalization via clathrin mediate endocytosis. The representative puncta shown in Fig. 4.11 C displayed a peak height of 180 nm, which is in agreement with the dimensions of clathrin coated pits reported determined by cryo-electron microscopy.[15] In contrast, Fig. 4.11 D shows the initial formation of a pit with a peak height of only 86 nm. Again, the average lifetime of this puncta was in line with that of clathrin coated pits, but the lower

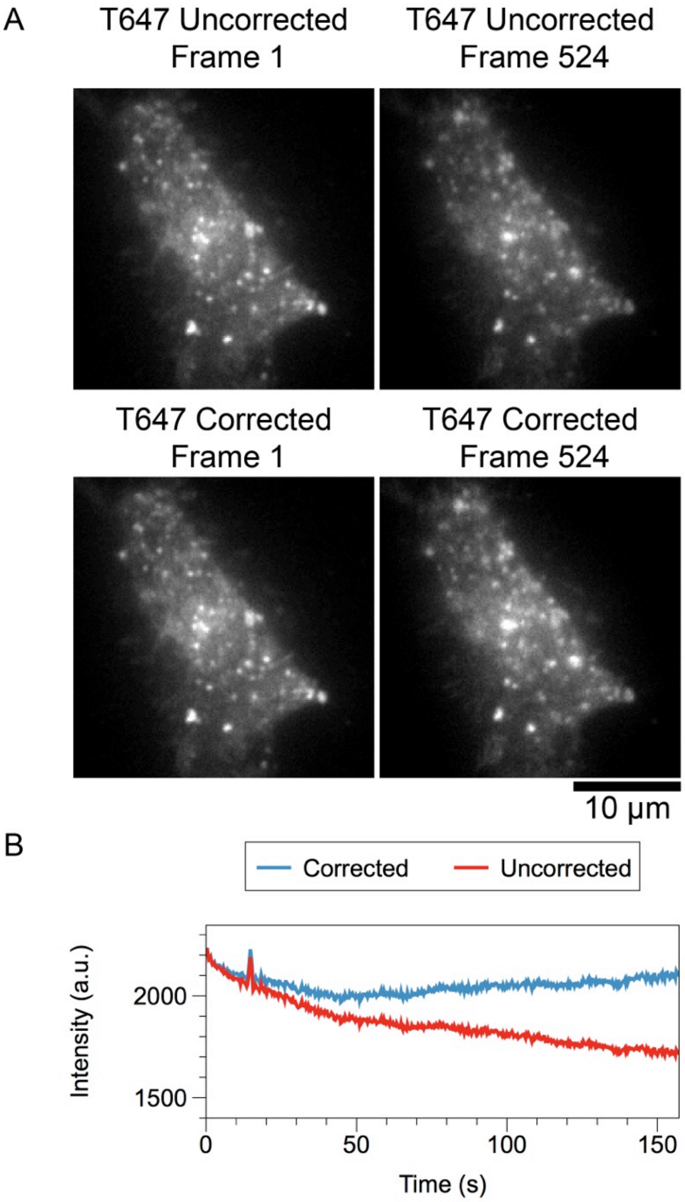

Figure 4.13: Representative photobleaching correction for dual channel live cell TIRF imaging. (A) Representative images show the first and last frames of a time lapse in the T647 channel for both corrected and uncorrected movies. The contrast of all representative images shown is identical. (B) Traces for corrected and uncorrected movies of the mean intensity of single frames through time.

z-position may indicate an aborted process, although this cannot be discerned from the current data. Importantly, the formation of a subset of EGFR puncta and the corresponding increase in fluorescence intensity was not always coupled with displacement in *z* (Fig. 4.11 E). These puncta accumulated intensity over a similar timescale to others, however were not dynamic in z. These puncta, which may represent abortive pits, illustrate that the measured *z* is independent of receptor density or clustering. In typical puncta traces an accumulation of receptor intensity in both channels was closely coupled with increases in *z*. This supports a model wherein EGFR is recruited into clusters at the site of pre-formed pits or that the pits are forming as the receptor is recruited rather than a sequential clustering of the receptor followed by pit formation. Therefore, the data agrees with the current hypothesis wherein cargo is sorted into pre-formed pits and provides additional detail as to the *z* state of endocytosis at the time of cargo selection.[16,17]

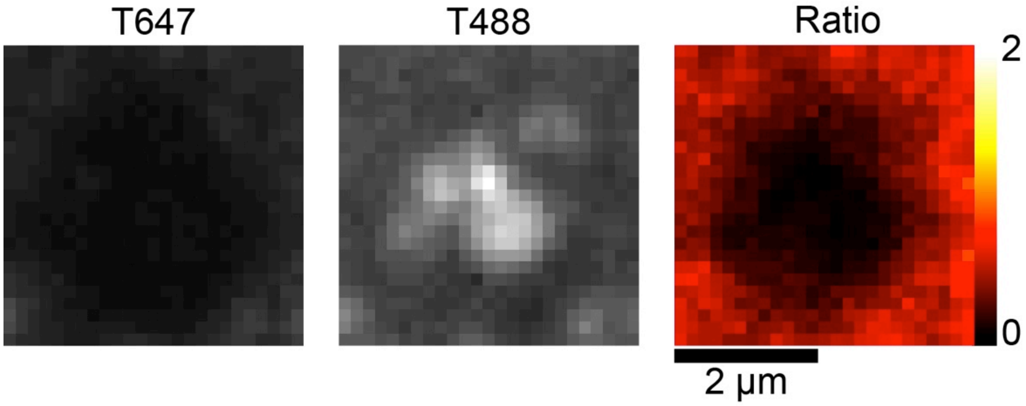

Figure 4.14: Both fluorescent labels must be present on the target for STAR to function. Representative images of a cell expressing both eGFP-EGFR and IRFP-EGFR on separate constructs. Areas of disparate protein expression are apparent between the channels, which artificially effects the ratio, giving rise to false height predictions.

4.8 Conclusion

In summary, we have a developed a simple strategy for using a standard TIRF microscope for determining the z-position of protein within a cell with nanometer resolution and in real-time. The technique is based on a ratiometric measurement of TIRF emission in two channels that is robust to changing concentrations of proteins. Through the use of silica microspheres, we have shown that STAR can accurately measure *z* positions within 21 nm over a range of 0-400 nm from the coverslip. Furthermore, height mapping of microtubules and tracking of EGFR endocytosis in real-time demonstrates key advantages of the method including compatibility with existing dyes and genetic labeling strategies, as well as simultaneous image acquisition that allows imaging of dynamic protein self-assembly events. One important caveat with STAR is that it is still diffraction limited in the xy plane. Thus, in cases where one microtubule (or any other object) passes over another, the measured Δz within the diffraction limit will represent a biased average of the height of both elements. Due to the fact that intensities in TIRF are greatest near the surface, this average will be weighted towards the lower object.

Additionally, STAR stands in contrast to the majority of established super-resolution techniques in that it does not require advanced sample preparation or specialized home-built equipment, and can therefore be implemented on standard TIRF microscopes that are commonly available in most labs. STAR is a widely adoptable method that could lower the barrier of entry to super-resolution imaging along the optical axis. Accordingly, the technique may also lead to many new discoveries surrounding the dynamics of fundamental processes that occur at the cell membrane.

4.9 Methods

Extended Theory

The intensity I of the evanescent field produced by TIRF exponentially decays with distance z from the coverslip/sample interface:

$$I = I_0 e^{-\frac{z}{d}}$$

Where I_0 is the intensity at $z = 0$ and

$$d = \frac{\lambda}{4\pi\sqrt{n_1^2 \sin\theta^2 - n_2^2}}$$

n_1 is the index of refraction of the glass coverslip and n_2 is the index of refraction of the sample, λ is the wavelength of the excitation light and θ is the angle of incidence. The evanescent field produced by two excitation wavelengths, λ_1 and λ_2 are:

$$I_{\lambda_1} = I_0 e^{-\frac{z}{d_{\lambda_1}}}$$
$$I_{\lambda_2} = I_0 e^{-\frac{z}{d_{\lambda_2}}}$$

The ratio of intensities, assuming constant n_1, n_2, and θ can be written as:

$$ln\left(\frac{I^{\lambda_2}}{I^{\lambda 1}}\right) = ln\left(\frac{I_0^{\lambda_2}}{I_0^{\lambda_1}}\right) + z\frac{1}{\gamma}$$

where:

$$\gamma = \frac{d^{\lambda_2} - d^{\lambda_1}}{d^{\lambda_2} \times d^{\lambda_1}}$$

Solving for z gives:

$$z = ln\left(\frac{I^{\lambda_2}}{I^{\lambda_1}}\right) - ln\left(\frac{I_0^{\lambda_2}}{I_0^{\lambda_1}}\right) \times \gamma$$

To bypass the requirement of measuring I_0, a relative z position, Δz, can be calculated, as a ratio of intensity ratios. The baseline ratio can be measured at $t = 0$, in a specific region of the sample, from a widefield image, or on a calibration sample known to be restricted to the coverslip.

$$\Delta z = ln\left(\frac{I^{\lambda_2}}{I^{\lambda_1}} \Big/ \frac{I_{base}^{\lambda_2}}{I_{base}^{\lambda_1}}\right) \times \frac{1}{\gamma}$$

Cell Culture

COS-7 cells were cultured in DMEM medium (Mediatech) supplemented with 10% FBS (Mediatech), sodium pyruvate (1 mM, Sigma), L-glutamine (2.1 mM, Mediatech), penicillin G (100 IU ml^{-1}, Mediatech) and streptomycin (100 μg ml^{-1}, Mediatech) and were incubated at 37 °C with 5% CO2. Cells were passaged at 80-90% confluency and plated at a density of 25% using standard cell culture procedures.

Microscope Setup

Images were acquired on a Nikon Eclipse Ti TIRF microscope with Elements software (Nikon). The microscope is equipped with an Evolve electron multiplying charge-coupled device (EMCCD; Photometrics) used for cell imaging and a CoolSnap (Nikon) CCD camera used for bead imaging, an Intensilight epifluorescence source (Nikon), a CFI Apo 100× 1.49 NA objective, and 488 nm (10 mW) and 640 nm (20 mW) laser lines. The microscope was equipped with the following Chroma filter cubes: Quad Band TIRF, individual TIRF at 488nm and 647nm, Cy5, Brightfield, and reflection interference contrast microscopy (RICM). EGFR internalization was imaged with an optical splitter, the Opto-Split III (Cairn Research), utilizing emission filters to pass the 488 and 647 nm lines onto equal but separate portions of the camera sensor area.

Plasmids

Rat EGFR tagged with EGFP (pEGFP-N1-EGFR) was a gift from Alexander Sorkin (University of Colorado Health Sciences Center). EGRF tagged with EGFP and IRFP (EGFR-IRFP-EGFP) was constructed by Oskar Laur in the Emory University Cloning Core as follows: first, IRFP was cloned out of Addgene plasmid 31856 (pShuttle CMV IRFP) using PCR. The PCR product was then ligated into the AgeI site in the above-mentioned EGFP-EGFR plasmid in order to form the full EGFR-IRFP-EGFP construct.

Silica Microsphere Labeling and Imaging

5 µm aminated silica microspheres (Bang's Labs) were functionalized with NHS-biotin (Pierce) following manufacturer protocols. Biotinylated beads were purified via centrifugation and resuspended in 1x PBS (3 cycles, 10 minutes per cycle). The beads were then incubated with dual-tagged streptavidin (prepared by standard reaction with succinimidyl esters of Alexa 488 and Alexa 647) for 20 min and re-purified. For imaging, beads were added to wells of a glass-bottomed 96 well plate (Nunco) in 63.5% glycerol (in 1x PBS) formulated to match the index of refraction of the beads (1.43). Beads were imaged with sequential TIRF 647, TIRF 488, Widefield 647, and Widefield 488 excitation.

Microtubule Imaging

COS-7 cells were seeded into wells of a glass bottomed 96-well plate (Nunco) and grown overnight. The next day, cells were rinsed with 5 mL 1x PBS and incubated with 4% Paraformaldehyde (in 1x PBS) for 12 min. Cells were then rinsed with 5 mL 1x PBS and permeabilized for 5 min with .1% Triton-X in 1x PBS. Cells were then rinsed with 5 mL PBS followed by incubation with 1% BSA in 1x PBS for 1 h at RT. After blocking, cells were labeled with a biotinylated β-tubulin primary antibody at 1:400 dilution in 1% BSA (in 1x PBS) for 1 h, followed by rinsing and incubation with 1 µg dual-tagged streptavidin in 200 µL 1% BSA in 1x PBS. Following fixation and staining, cells were imaged with the quad-band TIRF cube and alternating TIRF 488 and TIRF 647 excitaiton.

EGFR Imaging

COS-7 cells were grown overnight on glass and subsequently transfected with EGFR-EGFP-IRFP using Lipofectaime 2000 following manufacturer protocols. The cells were incubated in serum free media for 1 h before imaging. During this time, the cells were also incubated with 5 µM billiverdin to activate IRFP fluorescence. Time-lapse imaging was performed on individual cells following addition of 2 nM EGF (R&D Biosystems). 5 min movies were acquired with 200 ms exposure times and a 300 ms delay between frames. All live cell data were acquired using the Cairn OptosplitIII setup described above.

4.10 References

1. Klar, T. A., Jakobs, S., Dyba, M., Egner, A., and Hell, S. W., *Proceedings of the National Academy of Sciences* **97** (15), 8206 (2000).
2. Rust, M. J., Bates, M., and Zhuang, X., *Nat Meth* **3** (10), 793 (2006).
3. Gustafsson, M. G. L., *Journal of Microscopy* **198** (2), 82 (2000).
4. Betzig, E., Patterson, G. H., Sougrat, R., Lindwasser, O. W., Olenych, S. et al., *Science* **313** (5793), 1642 (2006).
5. Hess, S. T., Girirajan, T. P. K., and Mason, M. D., *Biophysical Journal* **91** (11), 4258 (2006).
6. Kanchanawong, P., Shtengel, G., Pasapera, A. M., Ramko, E. B., Davidson, M. W. et al., *Nature* **468** (7323), 580 (2010).
7. Xu, K., Zhong, G., and Zhuang, X., *Science* **339** (6118), 452 (2013).
8. Axelrod, D., *The Journal of Cell Biology* **89** (1), 141 (1981).
9. Mattheyses, A. L., Simon, S. M., and Rappoport, J. Z., *Journal of Cell Science* **123** (21), 3621 (2010).
10. Allersma, M. W., Wang, L., Axelrod, D., and Holz, R. W., *Molecular Biology of the Cell* **15** (10), 4658 (2004).
11. Saffarian, S. and Kirchhausen, T., *Biophysical Journal* **94** (6), 2333 (2008).
12. Paszek, M. J., DuFort, C. C., Rubashkin, M. G., Davidson, M. W., Thorn, K. S. et al., *Nat Meth* **9** (8), 825 (2012).
13. Mattheyses, A. L. and Axelrod, D., *Journal of Biomedical Optics* **11** (1) (2006).
14. Goh, L. K., Huang, F., Kim, W., Gygi, S., and Sorkin, A., *The Journal of Cell Biology* **189** (5), 871 (2010).
15. Saffarian, S., Cocucci, E., and Kirchhausen, T., *PLoS Biology* **7** (9), e1000191 (2009).
16. Rappoport, J. Z. and Simon, S. M., *Journal of Cell Science* **122** (9), 1301 (2009).
17. Scott, M. G. H., Benmerah, A., Muntaner, O., and Marullo, S., *Journal of Biological Chemistry* **277** (5), 3552 (2002).

Chapter 5: Conclusion

5.1 Perspectives

The EGFR is an extremely well characterized receptor tyrosine kinase with a precisely defined signaling network.[1] In spite of this, the role of mechanical force and spatial organization remain obscure due to a lack of suitable methods to study these aspects of receptor function. This dissertation has thus served to describe novel methods that are of use to answer such questions and will enable further study of the mechanisms of other receptor signaling and internalization in the coming years. Moreover, the approaches developed to study the EGFR pathway (Chapters 2-4), are not unique to the EGFR pathway, and can be adapted to investigate a wide range of membrane receptor biophysics and biochemistry.

5.2 The role of force in EGFR endocytosis.

In chapter 2, the development of a novel force sensor that allows the imaging of cell-exerted forces in real time was described. We used this sensor to address the question of whether a force is exerted by cells during the process of endocytosis, and in doing so we measured a peak force of 4 pN that was correlated with the presence of clathrin. This represents the first reported value of the force involved in EGFR endocytosis.[2] Our sensor has several advantages over similar techniques that make it particularly well suited for bridging the gap between biochemical and mechanotransductive events. Firstly, the sensor can report forces in the pN range with molecular specificity. For example, we were able to correlate distinct locations where cells were exerting forces on EGF functionalized sensor with eGFP-tagged clathrin puncta in a single imaging experiment. Another advantage is the fact that the sensor can image the force exerted by cells on the millisecond time domain across the entire basolateral membrane. Furthermore, the sensor does not require modification to cells or target proteins, allowing for minimal invasiveness that could perturb results.

In the intervening years since the force sensor was first published, the technique in general has come to be known as molecular tension fluorescence microscopy, or MTFM. Some of the first follow-up work sought to use MTFM to characterize the forces involved in cell adhesion. In order to do this, Yang Liu made use of a gold nanoparticle based sensor design to measure forces transduced through the integrin receptors present at focal adhesions.[3] This work showed that the basic tenets of MTFM are applicable to other systems, but made use of an extensively redesigned sensor, highlighting the difficulty of using a single sensor design in multiple systems without optimization.

In light of this, revising the sensor to make it more modular is highly desirable. While the PEG-based design is effective, there are some important drawbacks that keep it from being truly a plug-and-play system. Firstly, the current implementation is limited to small ligands (such as EGF), as random dye labeling of large ligands will result in non-uniform distances between the fluorophore and quencher across the population. This effect makes quantitative force measurements with large ligands all but impossible. Another issue is that new ligands must be optimized for use with the sensor by careful optimization of labeling chemistry and purification strategies. Lastly, Carol Jurchenko recently made the surprising discovery that the forces exerted by certain receptors (such as integrins) are large enough to dissociate individual sensors from the surface by breaking the biotin-streptavidin bond. As a consequence, the original sensor is best applied to systems that do not apply higher force levels (>15 pN), as loss of sensor from the surface makes force quantification impossible. It is important to note, however, that loss of the sensor from the surface was not observed during the course of the original study on EGFR endocytosis (this is likely due to the much lower magnitude of forces involved in receptor endocytosis as compared to cell adhesion and migration). All of these issues stand in the way of the widespread adoption and potential commercialization of MTFM, and it is therefore critical to overcome them.

In order to address these limitations, a universal force sensor design is currently being developed by Yuan Yang to be compatible with a much wider variety of ligands. The new design is fabricated using solid phase peptide synthesis as a single unit that includes the fluorophore, PEG linker, and quencher. This modular design ensures uniform distance between fluorophore and quencher for each sensor, and can be functionalized with ligand through native chemical ligation without the need for direct fluorophore labeling. The portion of the sensor that attaches to the surface is also modular, and it can be functionalized with either biotin (for low-force applications) or functional groups for covalent attachment to a surface (such as azides or alkynes) for higher force applications where biotin-streptavidin dissociation is a potential issue. Another advantage of this design is that the stoichiometry between the fluorophore and quencher remains 1 to 1. This is highly desirable, as differing amounts of fluorophore and quencher prevent the quantification of force from raw sensor data. If successful, this design could greatly expand the impact of the MTFM technique by allowing out-of-the-box use with a wide variety of ligands.

In addition to its applications in basic scientific research, the discovery that certain cancer cells exhibit different stiffness than healthy cells opens up potential for

MTFM to be used as a diagnostic method. Cancer and healthy cells can be distinguished via AFM, but these instruments do not exist in pathology labs and are not familiar to physicians.[4] As MTFM relies on standard fluorescence microscopy, it is in a much better position to be ported to the clinical setting. For this to happen, however, MTFM would have to be packaged into an easy-to-use clinical kit that is stable and gives a robust and easy to read signal. One potential way to overcome these barriers to entry in the clinical environment is through the use of a sensor design recently implemented by Yun Zhang. This sensor replaces the familiar PEG entropic spring with a DNA construct featuring a hairpin flanked by a fluorophore-labeled ligand and a quencher. When sufficient force is exerted on the ligand, the hairpin will open and the fluorophore will be removed from proximity with the quencher. This platform carries some of the same advantages as the universal force sensor design discussed previously, including defined stoichiometry and modularity with respect to ligand choice. Importantly, the unique design of the hairpin sensor could potentially be adapted into a high-throughput diagnostic method. In order to do this, the hairpin would be used as a switch to turn on rolling circle amplification (RCA). In such a design, the hairpin would be opened by force, after which circular RCA templates in solution would hybridize to the newly exposed single-stranded region of the hairpin sensor. Once this happens, RCA will occur indefinitely as long as the buffer solution contains the proper enzymes and a sufficient concentration of dNTPs. This extended DNA polymerization can be coupled with traditional pyrosequencing assays to give rise to an amplified fluorescent signal from a single sensor activation, increasing sensitivity. This system mirrors traditional biochemical assays such as qPCR and could be adapted to a pre-fabricated 96-well format that could be shipped already functionalized with a specific ligand (for the clinic) or left open to functionalization with a ligand of interest (for research settings). Once proof of concept for this amplified MTFM assay is demonstrated, baselines for healthy and transformed (cancerous) cells could be established, and detection thresholds could be set. Clinicians would then simply add tumor samples, incubate, and add the kit to a plate reader in order to determine if cancer is present. If successful, this version of MTFM could give rise to significant commercial interest for clinical applications, and would also be of interest to traditional biology groups accustomed to plate reader assays. In addition to diagnostics, this scheme could also be adapted into a high-throughput screen for drugs that affect mechanotransduction events.

The continued development of new sensor designs goes hand in hand with further investigation of biological questions that can be uniquely answered through the use of MTFM. Perhaps one of the most interesting of these questions is the origin of polarity in cell motility. Cells respond to cues, both mechanical and chemical, that dictate the directionality of migration through the polarization of cytoskeletal elements. For example, cells subjected to fluid shear flow undergo reorganization of actin along the direction of flow.[5] This process is a poignant example of mechanotransduction where the input and output signals are physical force and intermediate steps are transduced biochemically. While traditional methods are well suited to measure the biochemical aspects of this process, they cannot assess the physical inputs and outputs involved. MTFM could serve to augment current methods to allow the study of the physical inputs and outputs during this process while simultaneously measuring the biochemical changes taking place in the cell, such as the activation of c-Src in response to fluid shear.[6] In addition to providing a direct (as opposed to indirect) assessment of this process, MTFM allows the effects of shear flow to be imaged at earlier time points and could potentially reveal patterns of cell polarization in the exerted forces that occur before cell-wide reorganization of the cytoskeleton takes place. This line of investigation is currently being pursued in the lab by Kornelia Galior and shows promise in fully utilizing MTFM to correlate the physical inputs and outputs involved in shear flow alignment to the intermediate biochemical signals that have previously been characterized.

All in all, the future of MTFM may follows two paths. Firstly, further innovations in sensor design that overcome limitations on ligand selection and easy adaptation to other systems are essential. Secondly, it is important to continue to push the current generation of sensor designs towards answering questions in biology that are difficult to investigate with other techniques. Even in its most basic implementation, MTFM has several advantages that illustrate the promise of the technique, including compatibility with standard fluorescence microscopes, ligand specificity, simultaneous imaging of force and protein labels, and the ability to image in real time. With further refinement, we hope to see MTFM come into being as a standard method for the investigation of mechanotransduction events.

5.3 The effect of clustering on EGFR signaling.

Chapter 3 aimed to elucidate the role of EGFR clusters in receptor signaling. Dimerization of EGFR molecules has long been studied, but higher-order oligomers have also been observed.[7-9] While the dimerization model is well understood, the function of EGFR clusters remained mysterious. We used supported lipid bilayers on surfaces outfitted with diffusion barriers to control EGFR cluster size and observe the effect on signaling. This approach revealed that the size of the clusters has an effect on signal output: clusters smaller than 1 μm in size showed a 46% increase in signal over the control.[10] Further experiments were performed to attempt to elucidate the mechanism of cluster formation, which was found to depend on receptor phosphorylation while also being correlated with clathrin terminal domain associations and the actin cytoskeleton. Although these experiments reveal much about how clusters form, a precise mechanism has yet to be determined. For example, it is unclear whether cluster formation is due to receptor self-assembly or recruitment of receptors to clathrin coated structures. This particular question may be answered in the future through the use of targeted siRNA to critical elements of the CME pathway.[11] The role of receptor self-assembly may be addressed through mutation of a critical portion of the EGFR extracellular domain that has been performed previously in the literature but has not been investigated with regard to oligomers.[12] Another remaining question concerns the reason for the signal increase in larger clusters. While we speculate that this is due to a nucleation effect wherein ligand-bound receptors cross-phosphorylate unbound receptors (a process that could happen more efficiently with smaller clusters due to a larger perimeter to surface area ratio), the precise origin of the observed phenomenon is unknown. The cross-activation hypothesis could be tested by transfecting cells with fluorescently tagged kinase inactive EGFR mutants. Colocalization between mutant EGFR and phosphotyrosine signal at the sites of clusters would support the cross-activation model, and the contribution of cross-phosphorylation signal to the total signal across varying cluster sizes could further elucidate the mechanism. Future studies regarding EGFR clusters could provide critical knowledge about new types of interplay between EGFR signaling and CME, and could also provide insight into the function of the juxtacrine signaling pathways of EGFR.

5.4 Pushing the boundaries of optical microscopy in the z axis.

During the course of studying the EGFR endocytosis pathway, it became clear that the field was lacking tools that could observe nanometer changes along the optical axis with temporal resolution comparable to standard epifluorescence microscopy. We set out to develop a new imaging method to overcome this barrier in the hopes of uncovering dynamics that are difficult to capture with the traditional imaging techniques used to study CME. This method, known as simultaneous two-wavelength axial ratiometry (STAR), makes use of dual-channel TIRF imaging to locate target molecules with nm precision along the z axis. Due to the fact that both channels can be imaged at the same time, the technique is only limited by photon count and can therefore image just as fast as standard fluorescence microscopy methods. We used this technique to measure the internalization dynamics of EGFR in living cells, and were able to visualize the process as it occurred in real time.

STAR has several important limitations, and it is important to be aware of them when using the technique. As discussed in chapter 4, the presence of FRET between the dyes or fluorescent proteins on the protein of interest will result in inaccurate reporting of z position. For the most part, FRET contributions can be eliminated by using proper baseline measurements or through experimental design, but it is essential to know if FRET is present to obtain accurate z data. Like all fluorescence techniques, STAR requires modification of protein targets with either organic dyes or fluorescent proteins, which can lead to perturbation of wild-type function in some cases. Additionally, STAR measurements require the use of two fluorescence channels, which places further limits on multi color experiments as compared to traditional fluorescence techniques. A final caveat is the fact that objects at different z positions that are within a single diffraction limit along the xy plane will be measured as a single object having a composite height. As the evanescent field is strongest near the coverslip surface, this height will not be a true average but will be weighted towards the lower object. It should be noted that this drawback is shared by all similar TIRF techniques that are diffraction limited in the xy plane.

An important next step for STAR is to combine its high resolution z measurements with standard fluorescent protein imaging in the xy plane. For example, a much more robust study of EGFR internalization could be made using STAR to measure EGFR z position with simultaneous measurement of key proteins such as clathrin, epsin, and dynamin. This approach would be unique in its ability to correlate the real-time z position of EGFR to the arrival of proteins and measure the precise effect each of these events has on membrane curvature. While such studies have been done previously in EM preparations, real-time data would open up further lines of inquiry and potentially reveal transition states that cannot be easily seen in static samples.

Another interesting line of investigation would involve the combination of STAR with MTFM to correlate force with high-resolution protein imaging along the z axis. A good first step in this line of investigation could be to combine the original PEG-EGF sensor with STAR measurements of membrane labeling dyes. This would allow the direct correlation of membrane curvature to force loading in real-time, and would provide further information about the forces involved in endocytosis that could not be obtained in the original MTFM study. The ability to combine STAR with MTFM highlights one of the main advantages of the technique: compatibility with commercially available fluorescence microscopes, standard fluorescent immunohistochemistry, and fluorescent proteins. We believe that these traits put STAR in position to be adopted by a wider variety of labs.

5.5 Final Comments

In the future, we hope that the techniques and approaches enumerated herein will come into use in mainstream biological studies. Modern biochemical techniques have done much to elucidate the vast signaling networks that are at the core of cell behavior, but fall short in describing biophysical processes such as protein spatial organization and the generation of mechanical forces, or events that occur in real-time along the z axis. It is in this vein that we strive to extend the toolkit available to life scientists with non-specialized and convenient methods to allow further investigation of transmembrane receptors, protein spatial organization, and mechanotransduction events that have traditionally been difficult to study.

5.6 References

1. Yarden, Y. and Sliwkowski, M. X., *Nat Rev Mol Cell Biol* **2** (2), 127 (2001).
2. Stabley, D. R., Jurchenko, C., Marshall, S. S., and Salaita, K. S., *Nat Meth* **9** (1), 64 (2012).
3. Liu, Y., Yehl, K., Narui, Y., and Salaita, K., *Journal of the American Chemical Society* **135** (14), 5320 (2013).
4. Cross, S. E., Jin, Y.-S., Rao, J., and Gimzewski, J. K., *Nat Nano* **2** (12), 780 (2007).
5. Wechezak, A. R., Viggers, R. F., and Sauvage, L. R., *Laboratory investigation; a journal of technical methods and pathology* **53** (6), 639 (1985).
6. Okuda, M., Takahashi, M., Suero, J., Murry, C. E., Traub, O. et al., *Journal of Biological Chemistry* **274** (38), 26803 (1999).
7. Chung, I., Akita, R., Vandlen, R., Toomre, D., Schlessinger, J. et al., *Nature* **464** (7289), 783 (2010).
8. Abulrob, A., Lu, Z., Baumann, E., Vobornik, D., Taylor, R. et al., *Journal of Biological Chemistry* **285** (5), 3145 (2010).
9. Yang, S., Raymond-Stintz, M. A., Ying, W., Zhang, J., Lidke, D. S. et al., *Journal of Cell Science* **120** (16), 2763 (2007).
10. Stabley, D., Retterer, S., Marshall, S., and Salaita, K., *Integrative Biology* **5** (4), 659 (2013).
11. Huang, F., Khvorova, A., Marshall, W., and Sorkin, A., *Journal of Biological Chemistry* **279** (16), 16657 (2004).
12. Mattoon, D., Klein, P., Lemmon, M. A., Lax, I., and Schlessinger, J., *Proceedings of the National Academy of Sciences of the United States of America* **101** (4), 923 (2004).